

A STUDY OF NATURAL CONVECTION IN MOLTEN METAL UNDER A  
MAGNETIC FIELD

A THESIS SUBMITTED TO  
THE GRADUATE SCHOOL OF NATURAL AND APPLIED SCIENCES  
OF  
MIDDLE EAST TECHNICAL UNIVERSITY

BY

ERSAN GÜRAY

IN PARTIAL FULFILLMENT OF THE REQUIREMENTS  
FOR  
THE DEGREE OF DOCTOR OF PHILOSOPHY  
IN  
ENGINEERING SCIENCES

SEPTEMBER 2006

Approval of the Graduate School of Natural and Applied Sciences

---

Prof. Dr. Canan Özgen  
Director

I certify that thesis satisfies all the requirements as a thesis for the degree of Doctor of Philosophy.

---

Prof. Dr. Turgut Tokdemir  
Head of Department

This is to certify that we have read this thesis and that in our opinion it is fully adequate, in scope and quality, as a thesis for the degree of Doctor of Philosophy.

---

Assoc. Prof. Dr. Hakan Işık Tarman  
Supervisor

**Examining Committee Members**

Prof. Dr. Tekin Gültop	(Gazi Ün., CE)	_____
Assoc. Prof. Hakan I. Tarman	(METU, ES)	_____
Prof. Dr. Polat Saka	(METU, ES)	_____
Prof. Dr. Münevver Tezer	(METU, MATH)	_____
Prof. Dr. Turgut Tokdemir	(METU, ES)	_____

**I hereby declare that all information in this document has been obtained and presented in accordance with academic rules and ethical conduct. I also declare that, as required by these rules and conduct, I have fully cited and referenced all material and results that are not original to this work.**

Name, Last name :

Signature :

## **ABSTRACT**

### A STUDY OF NATURAL CONVECTION IN MOLTEN METAL UNDER A MAGNETIC FIELD

Güray, Ersan

Ph.D., Department of Engineering Sciences

Supervisor: Assoc. Prof. Hakan Işık Tarman

September 2006, 141 pages

The interaction between thermal convection and magnetic field is of interest in geophysical and astrophysical problems as well as in metallurgical processes such as casting or crystallization. A magnetic field may act in such a way to damp the convective velocity field in the melt or to reorganize the flow aligned with the magnetic field. This ability to manipulate the flow field is of technological importance in industrial processes. In this work, a direct numerical simulation of three-dimensional Boussinesq convection in a horizontal layer of electrically conducting fluid confined between two perfectly conducting horizontal plates heated from below in a gravitational and magnetic field is performed using a spectral element method. Periodic boundary conditions are assumed in the horizontal directions. The numerical model is then used to study the effects of imposing magnetic field. Finally, a low dimensional representation scheme is presented based on the Karhunen-Loeve approach.

Keywords: RB convection, magnetoconvection, spectral element methods, low dimensional model, Karhunen Loeve Galerkin.

## ÖZ

### MANYETİK BİR ALANIN ETKİSİ ALTINDAKİ ERİYİK METAL AKIŞKANDA DOĞAL KONVEKSİYON AKIMLARI

Güray, Ersan

Doktora, Mühendislik Bilimleri Bölümü

Tez Yöneticisi: Assoc. Prof. Hakan Işık Tarman

Eylül 2006, 141 sayfa

Isıl konveksiyon ve manyetik alan arasındaki etkileşim döküm ve kristalizasyon gibi metalürji konularının yanısıra jeofizik ve astrofizik konularıyla da ilişkilidir. Manyetik alan konvektif hız alanını sönümlendirebildiği gibi akışı manyetik alana bağlı yeniden şekillendirebilir. Bu, akışı ustalıkla yönlendirebilme özelliği endüstriyel işlemlerde teknolojik bir önem teşkil eder. Bu çalışmada, yerçekimi ve manyetik alan altındaki iki tam elektrik iletken tabakayla sınırlandırılmış, alttan ısıtılan, bir elektrik iletken akışkan tabakasında cereyan eden üç boyutlu Boussinesq konveksiyonunun spektral eleman yöntemi kullanılarak tam olarak nümerik benzetimi gerçekleştirilir. Yatay yönlerde periyodik sınır koşulları ele alınır. Sonrasında, nümerik model uygulanan manyetik alanın etkilerini çalışmak üzere kullanılır. Son olarak, Karhunen-Loeve yaklaşımıyla elde edilen düşük boyutlu sistemin çözümü ele alınmıştır.

Anahtar Kelimeler: RB konveksiyonu, manyetikonveksiyon, spektral eleman yöntemleri, düşük boyutlu model, Karhunen Loeve Galerkin.

To Turkish Nation

## **ACKNOWLEDGEMENTS**

The author would like to express my gratitude to all those who gave me the possibility to complete this thesis.

The author is deeply indebted to my supervisor Assoc. Prof. Dr. Hakan I. Tarman from Middle East Technical University whose help, stimulating suggestions, criticism and encouragement helped me in all the time of research for and writing of this thesis.

During the PhD period, author is supported and encouraged by his parent to go ahead with his thesis. He furthermore wishes to express his deepest gratitude to each member of his family for having provided him a comfortable, tranquil and excellent environment.

The author would also like to thank Prof. Dr. M. Ruşen Geçit, Prof. Dr. Turgut Tokdemir and Prof. Dr. Münevver Tezer for all their help, support, interest and valuable hints and insight.

The author is sincerely thankful to dear friends Durmuş and great Ayşegül and Özge who provided a peaceful, social and amusing environment in breaks.

This study was supported by The Scientific and Technological Research Council of Turkey (TUBITAK) Grant No: 105M044

## TABLE OF CONTENTS

PLAGIARISM .....	iii
ABSTRACT .....	iv
ÖZ .....	v
DEDICATION .....	vi
ACKNOWLEDGEMENTS .....	vii
TABLE OF CONTENTS .....	viii
CHAPTER	
1. INTRODUCTION .....	1
1.1 Earlier Research .....	3
1.2 Scope of the Work .....	5
2. MAGNETOCONVECTIVE MOTION .....	8
2.1 Model Equations .....	9
2.2 Discretizations .....	15
2.2.1 Computational Grids on Horizontal Domain .....	16
2.2.2 Quadrature in Vertical Direction .....	17
2.2.3 Temporal Discretization .....	20
3. WEAK FORMULATION OF EQUATIONS .....	26
3.1 Inverse of Helmholtz Operators .....	32
3.2 Solution for the Pressure .....	33
3.3 Special Cautions for the Constant Term Mode .....	36
3.4 Test Studies .....	37
4. STRONG FORMULATION OF HYDROMAGNETIC EQUATION .....	45
4.1 Construction of Hermite Cardinal Functions .....	47
4.2 Inverse of Differentiation Operators .....	52

4.3 Test Studies .....	56
5. NUMERICAL CODE VALIDATION IN REAL CASES .....	64
5.1 Two Dimensional Stationary Flows .....	67
5.2 Time Dependent Flows .....	80
6. A LOW DIMENSIONAL APPROXIMATION SCHEME TO MAGNETO-CONVECTION .....	109
6.1 Karhunen-Loeve Decomposition .....	110
6.2 Adaptation on Magneto-Convection Model ....	113
6.3 KL Description of Motion .....	117
7. CONCLUSIONS .....	131
REFERENCES .....	134
APPENDICES	
A. TEST FUNCTIONS .....	138
VITA .....	141

## LIST OF TABLES

### TABLES

Table 4.1	Maximum values of error for the test cases .....	59
Table 5.1	Grid refinement, $Ra = 50000$ , $Pr = 0.05$ and $Q = 900$ .....	67
Table 5.2	$Q_c$ ( $Nu = 1$ ) for $Ra = 10000$ , $Ra = 30000$ and $Ra = 50000$ ....	70
Table 5.3	$Nu$ and $\zeta$ . $Pr = 0.05$ . Present work with $\Gamma = 3:1.5$ and $\Gamma = 6:3$ at [6] .....	71
Table 5.4	Extrapolated values of $Ra_c$ ( $Nu = 1$ ) from Figure 5.9 for $Q = 0$ and $Q = 100$ at $\chi = 30^\circ$ , $\chi = 45^\circ$ , $\chi = 60^\circ$ and $\chi = 90^\circ$ .....	84
Table 6.1	Symetry group elements .....	113
Table 6.2	Mechanical KL modes for the first five .....	119
Table 6.3	Thermal KL modes for the first five .....	119
Table 6.4	The indexing of the KL modes as it appears in the KL spectrum plots in Figures 6.7 to 6.8 .....	121

## LIST OF FIGURES

### FIGURES

Figure 2.1	Computational domain and external vector fields ....	8
Figure 2.2	Ascendance of hot fluid, descendance of cold fluid in a roll action .....	9
Figure 3.1	$\mathbf{u}_x$ vs. $z$ at $x = \pi/4, y = \pi/4, t = 5$ .....	40
Figure 3.2	$\mathbf{u}_y$ vs. $z$ at $x = \pi/4, y = \pi/4, t = 5$ .....	40
Figure 3.3	$\mathbf{u}_z$ vs. $z$ at $x = \pi/4, y = \pi/4, t = 5$ .....	40
Figure 3.4	$\Theta$ vs. $z$ at $x = \pi/4, y = \pi/4, t = 5$ .....	41
Figure 3.5	$\mathbf{b}_x$ vs. $z$ at $x = \pi/4, y = \pi/4, t = 5$ .....	41
Figure 3.6	$\mathbf{b}_y$ vs. $z$ at $x = \pi/4, y = \pi/4, t = 5$ .....	41
Figure 3.7	$\mathbf{b}_z$ vs. $z$ at $x = \pi/4, y = \pi/4, t = 5$ .....	42
Figure 3.8	Infinite norm of error in $\mathbf{u}_x$ vs. $t$ .....	42
Figure 3.9	Infinite norm of error in $\mathbf{u}_y$ vs. $t$ .....	42
Figure 3.10	Infinite norm of error in $\mathbf{u}_z$ vs. $t$ .....	43
Figure 3.11	Infinite norm of error in $\Theta$ vs. $t$ .....	43
Figure 3.12	Infinite norm of error in $\mathbf{b}_x$ vs. $t$ .....	43
Figure 3.13	Infinite norm of error in $\mathbf{b}_y$ vs. $t$ .....	44
Figure 3.14	Infinite norm of error in $\mathbf{b}_z$ vs. $t$ .....	44
Figure 4.1	Code Flowchart .....	55
Figure 4.2	$ \bar{\mathbf{u}}_x $ at $z_3 = -0.677, t = 5$ .....	59
Figure 4.3	$ \bar{\mathbf{u}}_y $ at $z_3 = -0.677, t = 5$ .....	59
Figure 4.4	$ \bar{\mathbf{u}}_z $ at $z_3 = -0.677, t = 5$ .....	59
Figure 4.5	$ \bar{\Theta} $ at $z_3 = -0.677, t = 5$ .....	60

Figure 4.6	$ \bar{\mathbf{b}}_x $ at $z_3 = -0.677, t = 5$	60
Figure 4.7	$ \bar{\mathbf{b}}_y $ at $z_3 = -0.677, t = 5$	60
Figure 4.8	$ \bar{\mathbf{b}}_z $ at $z_3 = -0.677, t = 5$	61
Figure 4.9	Maximum value of $\ \mathbf{u}_x - \mathbf{u}_x^e\ _\infty$ vs. $\Delta t$	61
Figure 4.10	Maximum value of $\ \mathbf{u}_y - \mathbf{u}_y^e\ _\infty$ vs. $\Delta t$	61
Figure 4.11	Maximum value of $\ \mathbf{u}_z - \mathbf{u}_z^e\ _\infty$ vs. $\Delta t$	62
Figure 4.12	Maximum value of $\ \Theta_x - \Theta_x^e\ _\infty$ vs. $\Delta t$	62
Figure 4.13	Maximum value of $\ \mathbf{b}_x - \mathbf{b}_x^e\ _\infty$ vs. $\Delta t$	62
Figure 4.14	Maximum value of $\ \mathbf{b}_y - \mathbf{b}_y^e\ _\infty$ vs. $\Delta t$	63
Figure 4.15	Maximum value of $\ \mathbf{b}_z - \mathbf{b}_z^e\ _\infty$ vs. $\Delta t$	63
Figure 5.1	Velocity field, $Ra = 30000, Pr = 0.05$ and $Q = 1700$	72
Figure 5.2	Magnetic induction field $Ra = 30000,$ $Pr = 0.05$ and $Q = 1700$	73
Figure 5.3	$Nu$ vs. $Q$ with $Ra = 10000, Ra = 30000$ and $Ra = 50000$ for $Pr = 0.05$	74
Figure 5.4	Temperature contours on $xz$ plane at $y = 0.375.$ $Ra = 30000, Pr = 0.05$ and $Q = 1700.$ Restructuring of rolls from steady case at $Q = 1100.$ $t = 0$ and $t = 2$	75
Figure 5.5	Temperature contours on $xz$ plane at $y = 0.375.$ $Ra = 30000, Pr = 0.05$ and $Q = 1700.$ Restructuring of rolls from steady case at $Q = 1100.$ $t = 34$ and $t = 36$	76
Figure 5.6	Temperature contours on $xz$ plane at $y = 0.375.$ $Ra = 30000, Pr = 0.05$ and $Q = 1700.$ Restructuring of	

	rolls from steady case at $Q=1100$ . $t=38$ and $t=42$ .....	77
Figure 5.7	Temperature contours on $xz$ plane at $y=0.375$ . $Ra=30000$ , $Pr=0.05$ and $Q=1700$ . Restructuring of rolls from steady case at $Q=1100$ . $t=43$ and $t=45$ .....	78
Figure 5.8	$Nu$ vs. $Ra/Q$ in log scale .....	79
Figure 5.9	$Nu$ vs. $Ra$ for $Pr=0.1$ with when $Q=100$ .....	86
Figure 5.10	Velocity field and $\Theta$ contours on $xy$ plane at $z=-0.9109$ , $Ra=10000$ , $Pr=0.1$ , $Q=100$ and $\chi=90^\circ$ . ( $\Gamma=1.95:1.90$ ) .....	87
Figure 5.11	Velocity field and $\Theta$ contours on $xy$ plane at $z=0.9109$ , $Ra=10000$ , $Pr=0.1$ , $Q=100$ and $\chi=90^\circ$ . ( $\Gamma=1.95:1.90$ ) .....	87
Figure 5.12	$x$ and $y$ components of the velocity field vs. $t$ at $x=0.4875$ , $y=0.475$ and $z=-0.9109$ for $Ra=14000$ , $Pr=0.1$ , $Q=100$ and inc. angle is 60 degree .....	88
Figure 5.13	$z$ component of the velocity and temperature fields vs. $t$ at $x=0.4875$ , $y=0.475$ and $z=-0.9109$ for $Ra=14000$ , $Pr=0.1$ , $Q=100$ and inc. angle is 60 degree .....	89
Figure 5.14	Velocity field and $\Theta$ contours on $xy$ plane at $z=0$ and $t=10$ , $Ra=14000$ , $Pr=0.1$ , $Q=100$ and $\chi=60^\circ$ . ( $\Gamma=1.95:1.90$ ) .....	90
Figure 5.15	Velocity field and $\Theta$ contours on $xy$ plane at $z=0$ and $t=10.15$ , $Ra=14000$ , $Pr=0.1$ , $Q=100$ and $\chi=60^\circ$ . ( $\Gamma=1.95:1.90$ ) .....	90
Figure 5.16	Velocity field and $\Theta$ contours on $xy$ plane at $z=0$	

	and $t = 10.30$ , $Ra = 14000$ , $Pr = 0.1$ , $Q = 100$ and $\chi = 60^\circ$ . ( $\Gamma = 1.95 : 1.90$ ) .....	91
Figure 5.17	Velocity field and $\Theta$ contours on $xy$ plane at $z = 0$ and $t = 10.45$ , $Ra = 14000$ , $Pr = 0.1$ , $Q = 100$ and $\chi = 60^\circ$ . ( $\Gamma = 1.95 : 1.90$ ) .....	91
Figure 5.18	Frequency spectrum of $\mathbf{u}_x$ at $x = 0.4875$ , $y = 0.475$ and $z = -0.9109$ for $Ra = 14000$ , $Pr = 0.1$ , $Q = 100$ and $\chi = 60^\circ$ . ( $\Gamma = 1.95 : 1.90$ ) .....	92
Figure 5.19	$Nu$ vs. $t$ at $z = 0$ for $Ra = 20000$ , $Pr = 0.1$ , $Q = 100$ and inc. angle is 60 degree .....	93
Figure 5.20	$x$ and $y$ components of the velocity field vs. $t$ at $x = 0.4875$ , $y = 0.475$ and $z = -0.9109$ for $Ra = 20000$ , $Pr = 0.1$ , $Q = 100$ and inc. angle is 60 degree .....	94
Figure 5.21	$z$ component of the velocity and temperature fields vs. $t$ at $x = 0.4875$ , $y = 0.475$ and $z = -0.9109$ for $Ra = 20000$ , $Pr = 0.1$ , $Q = 100$ and inc. angle is 60 degree .....	95
Figure 5.22	Velocity field and $\Theta$ contours on $xy$ plane at $z = 0$ and $t = 10$ , $Ra = 20000$ , $Pr = 0.1$ , $Q = 100$ and $\chi = 60^\circ$ . ( $\Gamma = 1.95 : 1.90$ ) .....	96
Figure 5.23	Velocity field and $\Theta$ contours on $xy$ plane at $z = 0$ and $t = 10.15$ , $Ra = 20000$ , $Pr = 0.1$ , $Q = 100$ and $\chi = 60^\circ$ . ( $\Gamma = 1.95 : 1.90$ ) .....	96
Figure 5.24	Velocity field and $\Theta$ contours on $xy$ plane at $z = 0$ and $t = 10.30$ , $Ra = 20000$ , $Pr = 0.1$ , $Q = 100$ and $\chi = 60^\circ$ . ( $\Gamma = 1.95 : 1.90$ ) .....	97
Figure 5.25	Velocity field and $\Theta$ contours on $xy$ plane at $z = 0$	

	and $t = 10.45$ , $Ra = 20000$ , $Pr = 0.1$ , $Q = 100$ and $\chi = 60^\circ$ . ( $\Gamma = 1.95 : 1.90$ ) .....	97
Figure 5.26	Frequency spectrum of $\mathbf{u}_x$ at $x = 0.4875$ , $y = 0.475$ and $z = -0.9109$ for $Ra = 20000$ , $Pr = 0.1$ , $Q = 100$ and $\chi = 60^\circ$ . ( $\Gamma = 1.95 : 1.90$ ) .....	98
Figure 5.27	$Nu$ vs. $t$ at $z = 0$ for $Ra = 18000$ , $Pr = 0.1$ , $Q = 100$ and inc. angle is 30 degree .....	99
Figure 5.28	Velocity field and $\Theta$ contours on $xy$ plane at $z = 0$ and $t = 5$ , $Ra = 18000$ , $Pr = 0.1$ , $Q = 100$ and $\chi = 30^\circ$ . ( $\Gamma = 1.95 : 1.90$ ) .....	100
Figure 5.29	Velocity field and $\Theta$ contours on $xy$ plane at $z = 0$ and $t = 6$ , $Ra = 18000$ , $Pr = 0.1$ , $Q = 100$ and $\chi = 30^\circ$ . ( $\Gamma = 1.95 : 1.90$ ) .....	100
Figure 5.30	Velocity field and $\Theta$ contours on $xy$ plane at $z = 0$ and $t = 7$ , $Ra = 18000$ , $Pr = 0.1$ , $Q = 100$ and $\chi = 30^\circ$ . ( $\Gamma = 1.95 : 1.90$ ) .....	101
Figure 5.31	Frequency spectrum of $\Theta$ at $x = 0.4875$ , $y = 0.475$ and $z = -0.9109$ for $Ra = 18000$ , $Pr = 0.1$ , $Q = 100$ and $\chi = 30^\circ$ . ( $\Gamma = 1.95 : 1.90$ ) .....	101
Figure 5.32	$Nu$ vs. $t$ at $z = 0$ for $Ra = 18000$ , $Pr = 0.1$ , $Q = 100$ and inc. angle is 30 degree with halved asp. ratio .....	102
Figure 5.33	Velocity field and $\Theta$ contours on $xy$ plane at $z = 0$ and $t = 5.1$ , $Ra = 18000$ , $Pr = 0.1$ , $Q = 100$ and $\chi = 30^\circ$ . ( $\Gamma = 0.975 : 0.95$ ) .....	103
Figure 5.34	Velocity field and $\Theta$ contours on $xy$ plane at $z = 0$ and $t = 5.1725$ , $Ra = 18000$ , $Pr = 0.1$ , $Q = 100$ and $\chi = 30^\circ$ . ( $\Gamma = 0.975 : 0.95$ ) .....	103

Figure 5.35	Velocity field and $\Theta$ contours on $xy$ plane at $z = 0$ and $t = 5.245$ , $Ra = 18000$ , $Pr = 0.1$ , $Q = 100$ and $\chi = 30^\circ$ . ( $\Gamma = 0.975 : 0.95$ ) .....	104
Figure 5.36	Velocity field and $\Theta$ contours on $xy$ plane at $z = 0$ and $t = 5.3175$ , $Ra = 18000$ , $Pr = 0.1$ , $Q = 100$ and $\chi = 30^\circ$ . ( $\Gamma = 0.975 : 0.95$ ) .....	104
Figure 5.37	Velocity field and $\Theta$ contours on $xy$ plane at $z = 0$ and $t = 5.39$ , $Ra = 18000$ , $Pr = 0.1$ , $Q = 100$ and $\chi = 30^\circ$ . ( $\Gamma = 0.975 : 0.95$ ) .....	105
Figure 5.38	Velocity field and $\Theta$ contours on $xy$ plane at $z = 0$ and $t = 5.4625$ , $Ra = 18000$ , $Pr = 0.1$ , $Q = 100$ and $\chi = 30^\circ$ . ( $\Gamma = 0.975 : 0.95$ ) .....	105
Figure 5.39	Velocity field and $\Theta$ contours on $xy$ plane at $z = 0$ and $t = 5.535$ , $Ra = 18000$ , $Pr = 0.1$ , $Q = 100$ and $\chi = 30^\circ$ . ( $\Gamma = 0.975 : 0.95$ ) .....	106
Figure 5.40	Velocity field and $\Theta$ contours on $xy$ plane at $z = 0$ and $t = 5.6075$ , $Ra = 18000$ , $Pr = 0.1$ , $Q = 100$ and $\chi = 30^\circ$ . ( $\Gamma = 0.975 : 0.95$ ) .....	106
Figure 5.41	Velocity field and $\Theta$ contours on $xy$ plane at $z = 0$ and $t = 5.68$ , $Ra = 18000$ , $Pr = 0.1$ , $Q = 100$ and $\chi = 30^\circ$ . ( $\Gamma = 0.975 : 0.95$ ) .....	107
Figure 5.42	Frequency spectrum of $\Theta$ at $x = 0.24375$ , $y = 0.2375$ and $z = -0.9109$ for $Ra = 18000$ , $Pr = 0.1$ , $Q = 100$ and $\chi = 30^\circ$ . ( $\Gamma = 0.975 : 0.95$ ) .....	107
Figure 5.43	Total kinetic energy and magnetic energy vs. inc. angle for $Ra = 10000$ .....	108
Figure 6.1	The vertical profiles of KL modes ( $m = 1$ , $n = 0$ , $k$ ) with real (solid) and imaginary (dash) parts .....	121

Figure 6.2	The vertical profiles of KL modes ( $m = 1, n = 1, k$ ) with real (solid) and imaginary (dash) parts .....	122
Figure 6.3	The vertical profiles of KL modes ( $m = 0, n = 0, k$ ) with real (solid) and imaginary (dash) parts .....	123
Figure 6.4	The vertical profiles of the induced magnetic field components corresponding to KL modes ( $m = 1, n = 0, k$ ) with real (solid) and imaginary (dash) parts .....	124
Figure 6.5	The vertical profiles of the induced magnetic field components corresponding to KL modes ( $m = 1, n = 1, k$ ) with real (solid) and imaginary (dash) parts .....	125
Figure 6.6	The vertical profiles of the induced magnetic field components corresponding to KL modes ( $m = 0, n = 0, k$ ) with real (solid) and imaginary (dash) parts .....	126
Figure 6.7	The rolling motion at $Ra=10000, Pr=0.1$ obtained by integrating the dynamical system in time. The KL spectrum shows those modes (Table 6.3) excited in this steady regime .....	127
Figure 6.8	The periodic motion at $Ra=14000, Pr=0.1$ obtained by integrating the dynamical system in time. The KL spectrum shows that relatively more modes (Table 6.3) are excited in this periodic regime .....	128
Figure 6.9	The steady roll motion in Figure 6.7 cascades to zero as the strength of the vertical magnetic field applied is increased .....	129
Figure 6.10	The periodic motion in Figure 6.8 is inhibited by the application of the vertical magnetic field as	

shown in the time evolution of a particular  
expansion coefficient .....130

## LIST OF SYMBOLS

$A$	Vertical Laplacian matrix
$B$	Mass matrix
$\mathbf{b}$	Induced magnetic field vector
$\mathbf{B}$	Total magnetic field vector
$\mathbf{B}^q$	Induced magnetic field KL basis vector for $q$
$B_0$	Magnitude of external magnetic field
$C, D$	Vertical derivative matrices
$d$	Fluid layer height
$\mathbf{E}$	Kinematic viscosity
$E, \mathbf{E}$	Eigenvector matrix
$\mathbf{e}$	Unit vector
$f$	Heat equation forcing term
$\mathbf{f}_U, \mathbf{f}_\theta, \mathbf{f}_b$	Test case; forcing vectors
$G, G$	Eigenvalue matrix
$G$	Pressure equation forcing term
$g$	Gravity
$\mathbf{g}$	Momentum equation forcing term
$H$	Legendre Lagrange interpolant matrix
$H_B$	Coefficient matrix of hydromagnetic
$h_j$	Legendre Lagrange interpolant of order $j$
$H_U$	Coefficient matrix of momentum equation
$H_\theta$	Coefficient matrix of energy equation
$I$	Identity matrix
$i, j, l, p$	Index numbers
$\mathbf{J}$	Current density vector

$k$	Wavenumber
$k$	Quantum number
$L_j$	Legendre polynomial of order $j$
$L_x, L_y$	Horizontal box lengths
$m, n$	Wave index numbers
$m, n$	Time level
$N_x, N_y$	Number of grids horizontal directions
$N_z$	Grid parameter in vertical direction
$Nu$	Magnitude of external magnetic field
$P$	Pressure
$Pm$	Magnetic Prandtl number
$Pr$	Thermal Prandtl number
$\mathfrak{q}$	Hydro-magnetic equation forcing term
$Q$	Chandrasekhar number
$r$	Residual
$R$	Residual function
$Ra$	Rayleigh number
$S$	Pressure equation coefficient matrix
$s_x, s_y, \mathcal{V}$	Dimensionless box lengths
$T$	Temperature
$t$	Time
$\mathbf{u}$	Velocity vector
$u, v, w$	Velocity components
$\mathbf{U}^q$	Velocity field KL basis vector for $q$
$w_j$	Quadrature weight
$\mathbf{x}$	Space vector
$x, y, z$	Components of coordinate system
$\Delta t$	Time step

## Greek Symbols

$\chi$	Inclination angle
$\mu$	Magnetic permeability
$\nu$	Kinematic viscosity
$\rho$	Density
$\beta$	Coefficient of thermal expansion
$\nabla$	Gradient operator
$\nabla^2$	Laplacian operator
$\alpha$	Thermal diffusivity
$\lambda$	Magnetic diffusivity; eigenvalue
$\sigma$	Electrical conductivity
$\Theta$	Temperature fluctuation
$\omega$	Vorticity
$\Gamma$	Aspect ratio
$\zeta, \eta$	Wave numbers
$\Lambda$	Precondition matrix
$\delta_{ij}$	Kronecker delta tensor
$\delta_{\Theta}$	Thermal layer
$\zeta$	Wavelength
$\Psi, \Phi$	Eigenvectors
$\Theta^q$	Temperature field KL basis vector for $q$

## **CHAPTER 1**

### **INTRODUCTION**

The interaction between convection and magnetic field, magneto-convection, has been researched for a long time motivated by astrophysical and geophysical observations. Dynamics of sunspots and molten motion in the mantles of planets involve not only thermal effects but also strong magnetic forces. Magneto-convection is also of prevalent research interest in some industrial processes such as molten metal casting and crystallization. In crystal growth or steel production processes, magneto-convective motion governs the molecular bonding. During the process of crystal production, polycrystal silicon is heated from below and crystal develops during melting process. However, non-uniform distribution of dopant inhibits the development of well quality crystal. The impurities in a molten metal membrane can be limited by an external magnetic field during production. To organize the convective flow, an external magnetic field is applied to electrically conducting fluid; as a result, it determines the quality of the product. The magnetic field in any direction within the plane of the convective roll axis acts towards inhibition of forms of convective motions as stated by Chandrasekhar [1].

An electrically conducting infinite convective layer is the simplest geometry to numerically study the interaction between thermal convection and externally imposed magnetic

field. In this work, the influence of magnetic field on thermal convection in the layer bounded from top and bottom by perfectly conducting rigid plates is numerically simulated and analyzed. Flow driven by a heat source is resisted against by the gravity and Lorentz forces. While gravitation acts in direction of heat gradient, Lorentz force due to magnetic induction acts in any direction causing strong electromagnetic damping by Joule dissipation. The model equations governing the dynamics of magnetic field interaction with convective motion include divergence free conditions for induced magnetic field and velocity field, momentum conservation, energy transport and hydromagnetic equations. Dimensionless forms of these equations involve well known parameters, Rayleigh (Ra), Chandrasekhar (Q) numbers characterizing dynamics and thermal (Pr) and magnetic (Pm) Prandtl numbers characterizing material properties.

Rayleigh number is the ratio of buoyancy force to viscous dissipative effect of fluid and Chandrasekhar number is the ratio of the time scale of viscous dissipation to the time scale of Joule dissipation that implicitly states the strength of the magnetic field. Thermal  $Pr = \nu/\alpha$  and magnetic  $Pm = \nu/\lambda$  Prandtl numbers designate thermal  $\alpha$  and magnetic  $\lambda$  diffusivities relative to viscosity  $\nu$  of convective fluid. Dynamics of the magneto-convection depends on the ratio  $Pr/Pm$  fundamentally. This ratio indicates the relative magnitudes of magnetic diffusivity and thermal diffusivity. The variety of solutions depending upon to this ratio was pointed out by Veronis in 1959 [2]. In the case studied here, magnetic diffusivity is high ( $\lambda \gg \alpha$ ) which corresponds to the experimental situations involving liquid metals. Infact,

magnetic Prandtl number comes out to be very small in most of the natural events. Even in the deepest layer of the sun mantle, chromo-sphere, it is about  $10^{-4}$  and in the outer part of it, corona, it drops to until  $10^{-6}$ , where it corresponds to plasma. It is about  $10^{-8}$  in the earth's core which is made up with liquid iron and  $10^{-6}$  in the black holes and neutron stars.

### **1.1 Earlier Research**

The influence of magnetic field in a layer in which convection is driven by buoyancy is a special problem with the existence of double diffusion. Even though magnetic diffusion is accepted as dominant process in this study, this approach is in agreement with many applications or events. In 1955, Lehnert [3] stated that a uniform applied magnetic field has a pronounced effect on the decay of turbulence in a conducting fluid. He modelled the problem with linear equations and Deissler [4] had analyzed the problem numerically using these linear set of equations in 1963. In sixties, a Taylor series expansion of variables in time had been used by Nestlerode and Lumley [5] to solve the case with a strong field. Linear theory of magneto-convective mechanism is extensively discussed by Chandrasekhar [1] for various boundary conditions and the results were in a good agreement with the experiments by Nakagawa [6]. In these experiments, the linear relation between critical Ra number and the strength of magnetic field was reported which is also shown in the linear analysis of Chandrasekhar [1]. In the first systematic study of the development of nonlinear magneto-convection, preliminary results were given by Spiegel [7] and Weiss [8]. A general review can be found in literature for the nonlinear analysis of

the motion by Weiss [9]. In this review, double diffusive motion is considered with time dependent magnetic equation by means of the case where energy transfer mostly occurs by radiation. There exist a long series of research [10-13] headed by F.H. Busse *et al.* restricting attention to the case  $\lambda \gg \alpha$ . This corresponds to the physical situation that while the induced magnetic field is hardly modified by convection, the ambient homogeneous magnetic field affects the convective motions.

The emerging picture [10-12], [14-16] of the underlying dynamics under the influence of a vertical magnetic field reveals that the interaction of convection with the magnetic field causes Lorentz forces. They in turn are opposing the horizontal motions in recirculating natural convective flows. As the horizontal motion is ever present at the onset of convection in the form of two-dimensional rolls in the neighborhood of the critical Rayleigh number, the Lorentz force stabilizes the fluid and the onset of convection is shifted towards higher critical Ra. The increase of the critical Ra with an increasing Q is calculated by Chandrasekhar [1] using a linear stability analysis. Another important effect of the vertical magnetic field is the reduction in the horizontal length scales of convection. This is in a way minimization of Joule dissipation by reducing horizontal motions. The convection rolls become unstable to three dimensional disturbances in the form of waves which travel along the rolls and manifest themselves as transverse oscillations of the rolls. The inhibiting influence of the vertical magnetic field on the onset of oscillations is even stronger than the stabilizing influence on the onset of convection. A horizontal magnetic field, on the

other hand, has the most inhibiting effect on the onset of oscillation [13], [16]. The resulting Lorentz forces inhibit three dimensional oscillatory motion and give rise to transition into two dimensional convective roll pattern aligned with the magnetic field. This is a configuration with considerably less Joule dissipation. The additional delay of the oscillatory instability due to the horizontal magnetic field causes a much enlarged region of stable rolls.

## **1.2 Scope of the Work**

In this thesis, numerical simulations are performed on problem with the same physical parameters chosen in literature by imposing an external magnetic field inclined relative to the horizontal direction. In particular, the effect of the horizontal and vertical components of the external strong magnetic field is examined. The condition  $Pm \ll Pr$  (or equivalently  $\lambda \gg \alpha$ ) is taken into consideration. In this limit, the interaction terms between the velocity and the fluctuating components of the magnetic field in the hydromagnetic equation become negligible and the advection of the magnetic field by the velocity field is omitted as stated in the studies of Clever and Busse [11-13]. This is referred to as quasi-static approximation and as a result only additional linear terms appear in the equation of motion thus resulting in considerable simplification in the model equations and in the numerical simulations. In order to simulate the real cases and to compare with existing results in literature,  $Pr$  is selected to be 0.05 and 0.1.

Main objective of this study is to simulate magneto-convective flow numerically by using a spectral element method and to interpret the effects of the magnetic field over natural convection. The spectral element method is developed in the early eighties by Patera [17]. It is based on the weak (variational) form of the governing equations. In spectral element methods, the basis functions are hierarchical and follow easier rules of construction, for instance, they can be derived from Chebyshev or Legendre polynomials. As the order is increased, the former set of basis functions is simply augmented by a new set of polynomials constructed from the previous set. Therefore, in spectral element methods, the order of approximation is user-dependent and can even vary from element to element. There are numerical advantages in using the Chebyshev or Legendre polynomials instead of regularly spaced Lagrange interpolants.

The numerical scheme used in this work builds on the work of Schumack et al. [18] and Guessous [19]. The main features of the scheme are its treatment of the pressure term and the use of rescaled Legendre-Lagrangian interpolants to represent the velocity, temperature and the induced magnetic field. The treatment of the pressure term avoids the complicated staggered grids approach and instead pressure is approximated with lower order polynomials than velocity. For other numerical approaches, we refer to Chandrasekhar [1], publications of Clever and Busse [12], [13] and a numerical computation by a finite difference scheme, Mößner and Müller [20]. The validity of results is also shown in comparison with the experiment by [21].

In Chapter 2, the geometry of the problem, the system of model partial differential equations and dimensionless numbers are presented, and in addition the numerical scheme is constructed. In Chapter 3, a weak solution is obtained by applying Galerkin projection to the set of partial differential equations. Test functions are used to test the accuracy and consistency of the numerical scheme. In the next chapter 4, the weak formulation is performed for only the computation of the velocity field. On the other hand explicit values of induced magnetic field are evaluated in strong form at nodes by means of the differential operators. Analysis for stationary and time dependent flows are presented separately in Chapter 5. A preliminary work on a low dimensional representation scheme is presented in Chapter 6 based on the Karhunen-Loeve approach. In Chapter 7, results are summarized and main points of conclusions are drawn.

## CHAPTER 2

### MAGNETO-CONVECTIVE MOTION

The fluid layer, between perfectly conducting rigid plates with a depth  $d$  extending to infinity in the horizontal directions  $x$  and  $y$ , is heated from below and an inclined external magnetic field  $B_0$  is applied in the  $yz$  plane with angle  $\chi$  from  $y$  axis (Figure 2.1).

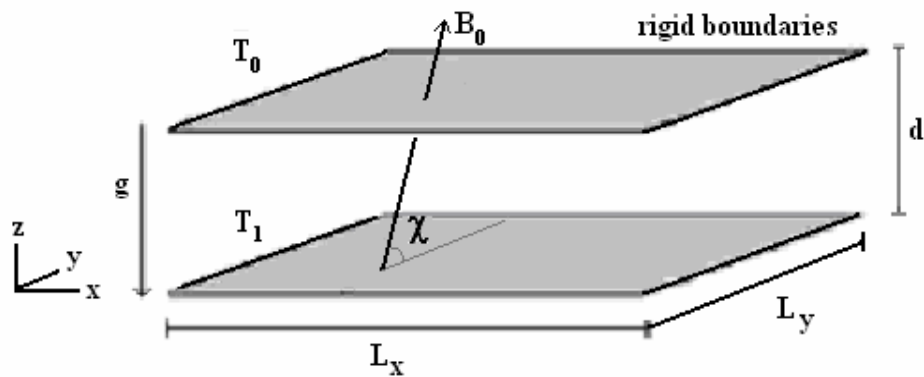


Figure 2.1 Computational domain and external vector fields.

Motionless state is maintained until a minimum temperature difference between bottom and top surfaces of the layer is reached and in this state the temperature varies in a linear manner. The heat is transmitted by means of pure conduction. The density of the heated fluid slowly drops due to thermal expansion and the balance between buoyancy, viscous and magnetic (Lorentz) forces maintains conductive

no-motion state. When the temperature difference is high enough or the magnitude of the magnetic field  $B_0$  is not adequate to inhibit motion, the layer rapidly resolves itself into a number of cells with roll motion which is ascension in the middle of a cell and a descension at the common boundary between a cell and its neighbours (Figure 2.2).

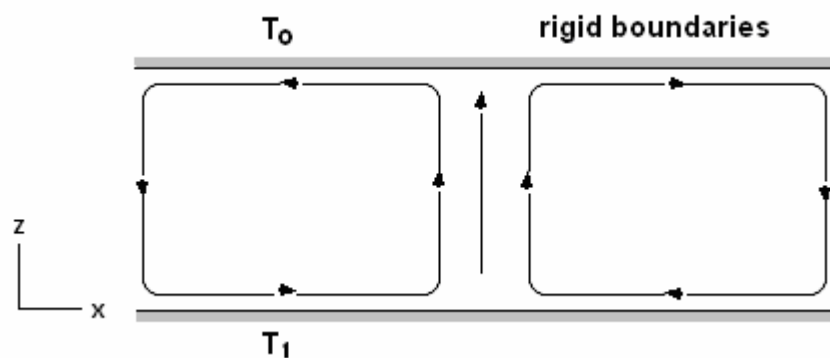


Figure 2.2 Ascendance of hot fluid, descendance of cold fluid in a roll action.

## 2.1 Model Equations

Mathematical model of magneto-convection in such a layer is constructed using Navier-Stokes equations which entails mass and momentum conservation including forcing terms of gravitation and magnetic fields. Various coefficients such as density  $\rho$ , kinematic viscosity  $\nu$  or thermal diffusivity  $\alpha$  are temperature dependent. The variation of these coefficients with temperature fundamentally depends upon the volumetric expansion coefficient,  $\beta$  which is a small number for fluids and gases as indicated in Chandrasekhar [1]. In addition to this, temperature differences are assumed to be

very small, therefore those equations can be arranged according to Boussinesq approximation that the variations in the coefficients are ignored except the variability of the density  $\rho$  appearing in the external gravitation term in the momentum equation is not. Conservation of mass and momentum for incompressible fluids under Boussinesq approximation can then be written respectively as:  $\Theta'$

$$\nabla \cdot \tilde{\mathbf{u}} = 0, \quad (2.1)$$

$$\frac{\partial \tilde{\mathbf{u}}}{\partial t} + (\tilde{\mathbf{u}} \cdot \nabla) \tilde{\mathbf{u}} = -\frac{1}{\rho_0} \nabla \tilde{P} - \frac{\rho}{\rho_0} g \mathbf{e}_z + \nu \nabla^2 \tilde{\mathbf{u}} + \frac{1}{\rho_0} (\tilde{\mathbf{J}} \times \tilde{\mathbf{B}}). \quad (2.2)$$

where  $\tilde{\mathbf{u}}$  is the velocity field,  $\tilde{P}$  is the pressure,  $\tilde{\mathbf{J}}$  is the current density and  $\tilde{\mathbf{B}}$  is the magnetic field. Here, “ $\sim$ ” refers to a total value of the variable.  $g$  is the acceleration of gravity in the opposite direction to  $\mathbf{e}_z$  and  $\rho_0$  is the density at a reference temperature  $T_0$ . According to the Ampere’s law, the relation between the current density and the magnetic field is:

$$\nabla \times \tilde{\mathbf{B}} = 4\pi\mu \tilde{\mathbf{J}} \quad (2.3)$$

where  $\mu$  is the magnetic permeability of the fluid. By substitution of (2.3) into (2.2), Lorentz forcing term ( $\tilde{\mathbf{J}} \times \tilde{\mathbf{B}}$ ) is redefined in a simple manner:

$$\frac{\partial \tilde{\mathbf{u}}}{\partial t} + (\tilde{\mathbf{u}} \cdot \nabla) \tilde{\mathbf{u}} = -\frac{1}{\rho_0} \nabla \tilde{P} - \frac{\rho}{\rho_0} g \mathbf{e}_z + \nu \nabla^2 \tilde{\mathbf{u}} + \frac{1}{4\pi\mu\rho_0} (\nabla \times \tilde{\mathbf{B}} \times \tilde{\mathbf{B}}) \quad (2.4)$$

or identically;

$$\frac{\partial \tilde{\mathbf{u}}}{\partial t} + (\tilde{\mathbf{u}} \cdot \nabla) \tilde{\mathbf{u}} = -\frac{1}{\rho_0} \nabla \left( \tilde{P} + \frac{|\tilde{\mathbf{B}}|^2}{8\pi\mu} \right) - \frac{\rho g \mathbf{e}_z}{\rho_0} + \nu \nabla^2 \tilde{\mathbf{u}} + \frac{1}{4\pi\mu\rho_0} (\tilde{\mathbf{B}} \cdot \nabla) \tilde{\mathbf{B}}. \quad (2.5)$$

Conservation of energy leads to the heat transport equation for the temperature field,  $\tilde{T}$ :

$$\frac{\partial \tilde{T}}{\partial t} + (\tilde{\mathbf{u}} \cdot \nabla) \tilde{T} = \alpha \nabla^2 \tilde{T} \quad (2.6)$$

in which heating due to viscous dissipation is neglected. Additionally, the interaction between the velocity field,  $\tilde{\mathbf{u}}$  and the magnetic field,  $\tilde{\mathbf{B}}$  is governed by Maxwell's equations. Since we are not interested in the effects of propagation of electromagnetic waves, the relation with respect to displacement currents is omitted. Charge density and its time variation are also dropped because they are relatively small [1]. Therefore Maxwell's equations give:

$$\nabla \cdot \tilde{\mathbf{B}} = 0, \quad (2.7)$$

$$\nabla \times \tilde{\mathbf{E}} = -\frac{\partial \tilde{\mathbf{B}}}{\partial t}, \quad (2.8)$$

together with (2.3). Here,  $\tilde{\mathbf{E}}$  is the electric field. Ohm's law for moving materials relative to a magnetic field  $\tilde{\mathbf{B}}$  dictates:

$$\tilde{\mathbf{J}} = \sigma(\tilde{\mathbf{E}} + \tilde{\mathbf{u}} \times \tilde{\mathbf{B}}) \quad (2.9)$$

where  $\sigma$  is the coefficient of electrical conductivity. By substitution of the curl of (2.3) and (2.9) into (2.8), it turns out to be an equation involving only the magnetic and velocity fields:

$$\frac{\partial \tilde{\mathbf{B}}}{\partial t} - \nabla \times (\tilde{\mathbf{u}} \times \tilde{\mathbf{B}}) = -\nabla \times [\lambda (\nabla \times \tilde{\mathbf{B}})] \quad (2.10)$$

or by using some vector identities;

$$\frac{\partial \tilde{\mathbf{B}}}{\partial t} = -(\tilde{\mathbf{u}} \cdot \nabla) \tilde{\mathbf{B}} + (\tilde{\mathbf{B}} \cdot \nabla) \tilde{\mathbf{u}} + \lambda \nabla^2 \tilde{\mathbf{B}}. \quad (2.11)$$

In (2.11), magnetic diffusivity is presented in a combined form:

$$\lambda = \frac{1}{4\pi \mu \sigma}. \quad (2.12)$$

The total values  $\tilde{\mathbf{u}}$ ,  $\tilde{\mathbf{P}}$  and  $\tilde{\mathbf{T}}$  can be decomposed as in the usual approach to their components representing variables in no-motion (conduction) state and in convection state:

$$\tilde{\mathbf{u}}(x, y, z, t) = 0 + \mathbf{u}'(x, y, z, t), \quad (2.13)$$

$$\tilde{\mathbf{P}}(x, y, z, t) = \check{\mathbf{P}}(z) + \mathbf{P}'(x, y, z, t), \quad (2.14)$$

$$\tilde{\mathbf{T}}(x, y, z, t) = \check{\mathbf{T}}(z) + \Theta'(x, y, z, t), \quad (2.15)$$

and the total magnetic field consists of two parts; externally imposed uniform magnetic field applied in the direction  $\mathbf{e}_B$  in the  $yz$  plane with a magnitude  $B_0$  and the induced magnetic field  $\mathbf{b}'$  which exists with convective motion:

$$\tilde{\mathbf{B}}(x, y, z, t) = B_0 \mathbf{e}_B + \frac{\alpha}{\lambda} B_0 \mathbf{b}'(x, y, z, t). \quad (2.16)$$

In the no-motion state of conduction, the pressure and temperature fields,  $\check{\mathbf{P}}$  and  $\check{\mathbf{T}}$  vary only in the vertical  $z$  direction. Here, primed variables represent fluctuations over the conduction state in the state of convection. Density is assumed to obey:

$$\rho = \rho_0 [1 - \beta(\check{\mathbf{T}} - T_0)]. \quad (2.17)$$

When pure conduction is considered and (2.17) is substituted, the momentum (2.5) and the heat transport (2.6) equations respectively give:

$$\frac{1}{\rho_0} \frac{\partial \check{\mathbf{P}}}{\partial z} = -[1 - \beta(\check{\mathbf{T}} - T_0)] g \mathbf{e}_z, \quad (2.18)$$

$$\frac{\partial^2 \check{\mathbf{T}}}{\partial z^2} = 0. \quad (2.19)$$

A linear temperature distribution in  $z$  is obtained by (2.19) as:

$$\check{\mathbf{T}}(z) = T_0 + \frac{(T_1 - T_0)}{2} \left(1 - \frac{z}{d/2}\right). \quad (2.20)$$

Advection term in (2.4) is rearranged for the improvement of numerical accuracy. (2.13) is substituted for velocity field and  $(\tilde{\mathbf{u}} \cdot \nabla)\tilde{\mathbf{u}}$  is rewritten in the form of:

$$(\mathbf{u}' \cdot \nabla)\mathbf{u}' = \nabla \left( \frac{\mathbf{u}' \cdot \mathbf{u}'}{2} \right) - \mathbf{u}' \times (\nabla \times \mathbf{u}') = \nabla \left( \frac{\mathbf{u}' \cdot \mathbf{u}'}{2} \right) - \mathbf{u}' \times \boldsymbol{\omega}'. \quad (2.21)$$

Substitution of equations from (2.13) to (2.16), (2.20) and (2.21) into (2.1), (2.5-2.7) and (2.11) gives with the final form of the equations of motion:

$$\nabla \cdot \mathbf{u}' = 0, \quad (2.22)$$

$$\begin{aligned} \frac{\partial \mathbf{u}'}{\partial t} = & \mathbf{u}' \times \boldsymbol{\omega}' - \frac{1}{\rho_0} \nabla \Pi' + \beta g \Theta' \mathbf{e}_z + \nu \nabla^2 \mathbf{u}' \\ & + \frac{1}{4\pi\mu\rho_0} \left[ B_0 \left( \text{Cos}\chi \frac{\partial}{\partial y} + \text{Sin}\chi \frac{\partial}{\partial z} \right) + B_0(\alpha/\lambda) \mathbf{b}' \cdot \nabla \right] \frac{\alpha}{\lambda} \mathbf{b}', \end{aligned} \quad (2.23)$$

$$\frac{\partial \Theta'}{\partial t} + (\mathbf{u}' \cdot \nabla)\Theta' = \mathbf{u}' \cdot \mathbf{e}_z \frac{T_1 - T_0}{2} + \alpha \nabla^2 \Theta', \quad (2.24)$$

$$\nabla \cdot \mathbf{b}' = 0, \quad (2.25)$$

$$\frac{\partial \mathbf{b}'}{\partial t} = -(\mathbf{u}' \cdot \nabla)\mathbf{b}' + \left[ \frac{B_0 \lambda}{\alpha} \left( \text{Cos}\chi \frac{\partial}{\partial y} + \text{Sin}\chi \frac{\partial}{\partial z} \right) + \mathbf{b}' \cdot \nabla \right] \mathbf{u}' + \lambda \nabla^2 \mathbf{b}' \quad (2.26)$$

where  $\Pi'$  is the stagnation pressure in dimensional form:

$$\Pi' = P' + \rho_0 \frac{|\mathbf{u}'|^2}{2} + \frac{\left| B_0 \mathbf{e}_{yz} + \frac{\alpha}{\lambda} B_0 \mathbf{b}' \right|^2}{8\pi\mu}. \quad (2.27)$$

All variables are normalized by dividing with the characteristic values:

$$x = \frac{x}{d/2}, t = \frac{t}{d^2/4\alpha}, \mathbf{u} = \frac{\mathbf{u}'}{2\alpha/d}, \Theta = \frac{\Theta'}{T_1 - T_0}, \Pi = \frac{\Pi'}{4\rho_0\alpha^2/d^2}, \mathbf{b} = \frac{\mathbf{b}'}{B_0}.$$

The dimensionless form of the governing equations is then:

$$\nabla \cdot \mathbf{u} = 0, \quad (2.28)$$

$$\begin{aligned} \frac{\partial \mathbf{u}}{\partial t} = & \mathbf{u} \times \boldsymbol{\omega} - \nabla \Pi + \text{Pr Ra}^* \Theta \mathbf{e}_z + \text{Pr} \nabla^2 \mathbf{u} \\ & + Q^* \text{Pr} \left[ \text{Cos}\chi \frac{\partial}{\partial y} + \text{Sin}\chi \frac{\partial}{\partial z} \right] \mathbf{b}, \end{aligned} \quad (2.29)$$

$$\frac{\partial \Theta}{\partial t} + (\mathbf{u} \cdot \nabla) \Theta = \mathbf{e}_z \frac{\mathbf{u}}{2} + \nabla^2 \Theta, \quad (2.30)$$

$$\nabla \cdot \mathbf{b} = 0, \quad (2.31)$$

$$\nabla^2 \mathbf{b} = - \left[ \text{Cos} \chi \frac{\partial}{\partial y} + \text{Sin} \chi \frac{\partial}{\partial z} \right] \mathbf{u}, \quad (2.32)$$

where the primes are dropped for the dimensionless variables. In reducing (2.26) into the form (2.32), the scope of this study involving convective fluid with high magnetic diffusivity  $\lambda$  (liquid metals) is taken into consideration. Following [13], this is referred to as quasi-static approximation. Dimensionless form of the total magnetic field is introduced as:

$$\mathbf{B} = \text{Cos} \chi \mathbf{e}_y + \text{Sin} \chi \mathbf{e}_z + \frac{\alpha}{\lambda} \mathbf{b}. \quad (2.33)$$

Here,  $\mathbf{u} = (u_x, u_y, u_z)$  and  $\mathbf{b} = (b_x, b_y, b_z)$  are the dimensionless forms of the velocity and the induced magnetic fields.  $\mathbf{e}_y$  and  $\mathbf{e}_z$  are the unit vectors in the  $y$  and  $z$  directions, respectively.  $\Theta$  is the temperature fluctuation in dimensionless form in the convective state.  $\omega$  is the vorticity which is the curl of velocity and  $\Pi$  is the dimensionless form of combined scalar terms. The dimensionless parameters Rayleigh ( $\text{Ra}^*$ ) and Chandrasekhar ( $\text{Q}^*$ ) numbers are modified in accordance with the scaling based on the half-depth as defined by:

$$\text{Ra}^* = \frac{\text{Ra}}{8} = \frac{\beta g (T_1 - T_0) d^3}{8 \nu \alpha}, \quad (2.34)$$

$$\text{Q}^* = \frac{\text{Q}}{4} = \frac{B_0^2 d^2}{4 \rho \mu \nu \lambda}. \quad (2.35)$$

Thermal Prandtl ( $\text{Pr}$ ) does not change:

$$\text{Pr} = \frac{\nu}{\alpha}. \quad (2.36)$$

All physical variables are subjected to periodic boundary conditions in the horizontal  $x$  and  $y$  directions. Due to the rigid plates on  $z$  boundaries, no slip boundary conditions for  $\mathbf{u}$ , perfectly conducting boundary conditions for  $\Theta$  and electrically high conductive boundary conditions for the induced magnetic field,  $\mathbf{b}$ , are imposed such that:

$$\mathbf{u} = \Theta = 0 \quad \text{and} \quad \frac{\partial \mathbf{b}_x}{\partial z} = \frac{\partial \mathbf{b}_y}{\partial z} = \mathbf{b}_z = 0 \quad \text{at } z = \mp 1. \quad (2.37)$$

## 2.2 Discretizations

A spectral element numerical scheme for pure Rayleigh Benard convection (RBC) is constructed by Guessous [19], which is based on the earlier works by Patera [17], Schumack et al. [18] and Orszag [22].

While Fourier expansions are used for the discretization of the variables in the horizontal  $x$  and  $y$  directions due to the assumption of periodicity, a polynomial type basis is used for the approximation in the vertical direction. As developed in the work of Schumack et.al. [18], and applied in the study of Guessous [19], velocity and temperature approximation in the  $z$  direction are based on the rescaled Lagrange-Legendre interpolants expansion. The absence of boundary conditions for the pressure variable at  $z = \pm 1$  is accommodated by an expansion based on two order less Legendre polynomial expansion than those for the other variables. This replaces the need to use staggered grid approach and thus simplifying the implementation.

### 2.2.1 Computational Grids on Horizontal Domain

Consideration of periodicity in the horizontal  $x$  and  $y$  directions naturally restricts the computational domain to a rectangular box with an aspect ratio  $\Gamma = s_x/2 : s_y/2$ , where  $s_x$  and  $s_y$  are the dimensionless lengths of the box in the horizontal directions:

$$0 \leq x \leq s_x = \frac{L_x}{d/2}, \quad (2.38)$$

$$0 \leq y \leq s_y = \frac{L_y}{d/2} \quad (2.39)$$

with  $-1 \leq z \leq +1$  and  $t \geq 0$ .

All physical variables are represented by their Fourier expansions in the  $x$  and  $y$  directions:

$$\begin{bmatrix} \mathbf{u} \\ \Theta \\ \mathbf{b} \\ \Pi \end{bmatrix} (x, y, z_i, t) = \sum_m \sum_n \begin{bmatrix} \hat{\mathbf{u}} \\ \hat{\Theta} \\ \hat{\mathbf{b}} \\ \hat{\Pi} \end{bmatrix} (m, n, z_i, t) \cdot \exp[i(m\zeta \cdot x + n\eta \cdot y)], \quad (2.40)$$

where  $m\zeta$  and  $n\eta$  are the wave numbers with

$$\zeta = 2\pi/s_x, \quad (2.41)$$

$$\eta = 2\pi/s_y \quad (2.42)$$

and  $m$  and  $n$  are integers in the range

$$1 - \frac{N_x}{2} \leq m \leq \frac{N_x}{2}, \quad (2.43)$$

$$1 - \frac{N_y}{2} \leq n \leq \frac{N_y}{2}. \quad (2.44)$$

Here,  $N_x$  and  $N_y$  represent the horizontal resolution. The collocation points in the horizontal directions are:

$$x_i = \frac{2\pi \cdot i}{\zeta \cdot N_x}, \quad (2.45)$$

$$y_j = \frac{2\pi \cdot j}{\eta \cdot N_y}. \quad (2.46)$$

For each wave index pair  $(m,n)$ , the periodic boundary conditions (2.37) for the physical variables,  $\mathbf{u}$ ,  $\Theta$  and  $\mathbf{b}$  are:

$$\mathbf{u}\left(x + \frac{2\pi \cdot m}{\zeta}, y + \frac{2\pi \cdot n}{\eta}, z, t\right) = \mathbf{u}(x, y, z, t), \quad (2.47)$$

$$\Theta\left(x + \frac{2\pi \cdot m}{\zeta}, y + \frac{2\pi \cdot n}{\eta}, z, t\right) = \Theta(x, y, z, t), \quad (2.48)$$

$$\mathbf{b}\left(x + \frac{2\pi \cdot m}{\zeta}, y + \frac{2\pi \cdot n}{\eta}, z, t\right) = \mathbf{b}(x, y, z, t). \quad (2.49)$$

### 2.2.2 Quadrature in the Vertical Direction

The collocation points in the vertical  $z$  direction are the Legendre-Gauss-Lobatto quadrature points. The Legendre-Gauss-Lobatto quadrature points are computed as the roots of:

$$q(z) = (1 - z^2) L'_{N_z}(z) \quad (2.50)$$

where prime denotes the differentiation with respect to  $z$  and  $L_{N_z}$  is the Legendre polynomial of order  $N_z$  which can be obtained from the Rodrigues' formula:

$$L_{N_z}(z) = \frac{1}{2^{N_z} N_z!} \frac{d^{N_z}}{dz^{N_z}} (z^2 - 1)^{N_z}. \quad (2.51)$$

The quadrature points consist of two collocation points, which are specified a priori as the boundary nodes  $z_0 = -1$  and  $z_{N_z} = 1$ , and  $N_z - 1$  roots of Legendre polynomial  $L'_{N_z}(z)$ . The interior collocation points satisfy some three term

relations as a general property of Jacobi polynomials. These relations are derived in [23] for Legendre polynomials and here they can be manipulated by using the properties of Legendre polynomials:

$$z L_{N_z}(z) = \frac{N_z}{2N_z+1} L_{N_z-1}(z) + \frac{N_z+1}{2N_z+1} L_{N_z+1}(z) \quad (2.52)$$

$$L_{N_z}(z) = -\frac{1}{2N_z+1} L'_{N_z-1}(z) + \frac{1}{2N_z+1} L'_{N_z+1}(z) \quad (2.53)$$

$$(1-z^2)L'_{N_z}(z) = \frac{N_z(N_z+1)}{2N_z+1} L_{N_z-1}(z) - \frac{N_z(N_z+1)}{2N_z+1} L_{N_z+1}(z) \quad (2.54)$$

Substitution of (2.54) into (2.50) gives a direct relation in terms of the Legendre polynomials:

$$q(z) = \frac{N_z(N_z+1)}{2N_z+1} L_{N_z-1}(z) - \frac{N_z(N_z+1)}{2N_z+1} L_{N_z+1}(z) \quad (2.55)$$

To obtain the convenient recursive relation for the computation of the roots using Newton method, differentiation of  $q(z)$  in (2.55) is necessary:

$$q'(z) = \frac{N_z(N_z+1)}{2N_z+1} L'_{N_z-1}(z) - \frac{N_z(N_z+1)}{2N_z+1} L'_{N_z+1}(z). \quad (2.56)$$

Substitution of (2.53) in to the equation (2.56) provides a simple form:

$$q'(z) = -N_z(N_z+1)L_{N_z}(z). \quad (2.57)$$

The roots of  $q(z) = 0$  are computed by Newton iteration:

$$z_j^{k+1} = z_j^k - \frac{q(z_j^k)}{q'(z_j^k)} = z_j^k + \frac{L_{N_z-1}(z) - L_{N_z+1}(z)}{(2N_z+1)L_{N_z}(z)} \quad (2.58)$$

Initial values of  $z$  are chosen as the Chebyshev points:

$$z_j^o = \cos\left(\frac{j\pi}{N_z}\right) \quad (2.59)$$

for  $1 \leq j \leq N_z - 1$ . Iteration is performed for each node until satisfactory accuracy is obtained. Corresponding weights are given by [24] as:

$$w_j = \begin{cases} \frac{2}{N_z(N_z + 1)} & j = 0 \text{ and } j = N_z, \\ \frac{2(L_{N_z}(x_j))^{-2}}{N_z(N_z + 1)} & 1 \leq j \leq N_z - 1. \end{cases} \quad \text{for} \quad (2.60)$$

In the works of Schumack [18] and Guessous [19], the velocity and temperature variables are expanded in  $z$  by rescaled Lagrange Legendre interpolants,  $\bar{h}_p(z)$  for each pair  $(m,n)$  in Fourier space. Rescaled Legendre-Lagrangian interpolants are obtained by dividing the Lagrangian interpolants by the square root of the corresponding quadrature weights [24]:

$$\bar{h}_i(z) = \frac{h_i(z)}{\sqrt{w_i}} = -\frac{(1-z^2)L'_{N_z}(z)}{N_z(N_z + 1)L_{N_z}(z_i)(z - z_i)\sqrt{w_i}}, \quad (2.61)$$

Here, at the grid (collocation) points,  $z_i$ , the rescaled Lagrangian interpolants (2.61) satisfy the Lagrangian property:

$$\bar{h}_i(z_j) = \frac{h_i(z_j)}{\sqrt{w_i}} = \frac{\delta_{ij}}{\sqrt{w_i}} \quad (2.62)$$

where  $\delta$  is the usual Kronecker Delta tensor. In the case of magneto-convection, the additional flow variable, namely, the induced magnetic field is expanded in terms of the same interpolants, and thus all variables are now represented in the form:

$$\begin{bmatrix} \hat{\mathbf{u}} \\ \hat{\Theta} \\ \hat{\mathbf{b}} \end{bmatrix} (m, n, z_i, t) = \sum_{j=0}^{N_z} \begin{bmatrix} \bar{\mathbf{u}} \\ \bar{\Theta} \\ \bar{\mathbf{b}} \end{bmatrix} (m, n, z_j, t) \cdot \bar{h}_j(z_i) = \begin{bmatrix} \bar{\mathbf{u}} \\ \bar{\Theta} \\ \bar{\mathbf{b}} \end{bmatrix} (m, n, z_i, t) \cdot \bar{h}_i(z_i) \quad (2.63)$$

Here, over-bar denotes the rescaled values of the variables.

$\hat{\Pi}$  is expanded in terms of two order less Legendre polynomials:

$$\hat{\Pi}(m, n, z, t) = \sum_{j=1}^{N_z-1} \bar{\Pi}(m, n, j, t) \cdot L_{j-1}(z). \quad (2.64)$$

### 2.2.3 Temporal Discretization

In this study, as indicated earlier, fluid in the layer is assumed to be incompressible therefore the discrete operators of the linear terms will be constant or time independent coefficient tensors. In this case, linear terms, i.e. the viscous term and the pressure are considered implicitly [25]. Nonlinear advection and forcing terms are implemented explicitly. In summary time discretization is performed using a semi-implicit scheme. Advection and forcing terms are discretized in time using second order Adams-Bashforth method and the others using Crank-Nicolson. Both methods have second order accuracy. After the temporal discretization, governing equations (2.28) to (2.32) are written in the form:

$$\nabla \cdot \mathbf{u}^{n+1} = 0, \quad (2.65)$$

$$\begin{aligned} \frac{\mathbf{u}^{n+1} - \mathbf{u}^n}{\Delta t} = & \frac{3}{2} \left\{ \mathbf{u} \times \boldsymbol{\omega} + \text{PrRa}^* \Theta \mathbf{e}_z + Q^* \text{Pr} \left[ \text{Cos}\chi \frac{\partial}{\partial y} + \text{Sin}\chi \frac{\partial}{\partial z} \right] \mathbf{b} \right\}^n \\ & - \frac{1}{2} \left\{ \mathbf{u} \times \boldsymbol{\omega} + \text{PrRa}^* \Theta \mathbf{e}_z + Q^* \text{Pr} \left[ \text{Cos}\chi \frac{\partial}{\partial y} + \text{Sin}\chi \frac{\partial}{\partial z} \right] \mathbf{b} \right\}^{n-1} \\ & + \frac{1}{2} \left\{ \text{Pr} \nabla^2 \mathbf{u} - \nabla \Pi \right\}^{n+1} + \frac{1}{2} \left\{ \text{Pr} \nabla^2 \mathbf{u} - \nabla \Pi \right\}^n, \end{aligned} \quad (2.66)$$

$$\frac{\Theta^{n+1} - \Theta^n}{\Delta t} = \frac{3}{2} \left\{ \mathbf{e}_z \frac{\mathbf{u}}{2} - (\mathbf{u} \cdot \nabla) \Theta \right\}^n - \frac{1}{2} \left\{ \mathbf{e}_z \frac{\mathbf{u}}{2} - (\mathbf{u} \cdot \nabla) \Theta \right\}^{n-1} + \frac{1}{2} \nabla^2 (\Theta^{n+1} + \Theta^n), \quad (2.67)$$

$$\nabla \cdot \mathbf{b}^n = 0, \quad (2.68)$$

$$\nabla^2 \mathbf{b}^n = - \left[ \text{Cos} \chi \frac{\partial}{\partial y} + \text{Sin} \chi \frac{\partial}{\partial z} \right] \mathbf{u}^n. \quad (2.69)$$

Here,  $\Delta t$  and  $n$  denote the size of the constant time-step and the time level, respectively. Divergence free condition on the velocity field (2.65) is enforced at time level  $n+1$ . Since induced magnetic field is directly connected to the velocity field by the quasi-steady relationship (2.69), a solenoid velocity field will generate a solenoid induced magnetic field. Therefore, there is no need to satisfy the divergence free condition on the magnetic field and thus (2.68) is implicitly satisfied. These set of partial differential equations are compacted by rearranging in the following form:

$$\nabla \cdot \mathbf{u}^{n+1} = 0, \quad (2.70)$$

$$\left( \text{Pr} \nabla^2 - \frac{2}{\Delta t} \right) \mathbf{u}^{n+1} = \nabla \Pi^{n+1} + \mathbf{g}^n, \quad (2.71)$$

$$\left( \text{Pr} \nabla^2 - \frac{2}{\Delta t} \right) \Theta^{n+1} = f^n, \quad (2.72)$$

$$\nabla^2 \mathbf{b}^n = \mathbf{q}^n. \quad (2.73)$$

where  $\mathbf{g}^n$ ,  $f^n$  and  $\mathbf{q}^n$  are the forcing terms at the  $n^{\text{th}}$  level in (2.66), (2.67) and (2.69):

$$\begin{aligned}
\mathbf{g}^n = & -3 \left( \mathbf{u} \times \boldsymbol{\omega} + \text{Pr Ra}^* \Theta \mathbf{e}_z + \text{Q}^* \text{Pr} \left[ \text{Cos}\chi \frac{\partial}{\partial y} + \text{Sin}\chi \frac{\partial}{\partial z} \right] \mathbf{b} \right)^n \\
& + \left( \mathbf{u} \times \boldsymbol{\omega} + \text{Pr Ra}^* \Theta \mathbf{e}_z + \text{Q}^* \text{Pr} \left[ \text{Cos}\chi \frac{\partial}{\partial y} + \text{Sin}\chi \frac{\partial}{\partial z} \right] \mathbf{b} \right)^{n-1} \quad (2.74) \\
& + \nabla \Pi^n - \left( \text{Pr} \nabla^2 + \frac{2}{\Delta t} \right) \mathbf{u}^n,
\end{aligned}$$

$$\mathbf{f}^n = -3 \left( \mathbf{e}_z \frac{\mathbf{u}}{2} - (\mathbf{u} \cdot \nabla) \Theta \right)^n + \left( \mathbf{e}_z \frac{\mathbf{u}}{2} - (\mathbf{u} \cdot \nabla) \Theta \right)^{n-1} - \left( \nabla^2 + \frac{2}{\Delta t} \right) \Theta^n, \quad (2.75)$$

$$\mathbf{q}^n = - \left[ \text{Cos}\chi \frac{\partial}{\partial y} + \text{Sin}\chi \frac{\partial}{\partial z} \right] \mathbf{u}^n. \quad (2.76)$$

The boundary conditions are imposed as:

$$\mathbf{u}^{n+1} = \Theta^{n+1} = 0 \quad \text{and} \quad \frac{\partial \mathbf{b}_x^n}{\partial z} = \frac{\partial \mathbf{b}_y^n}{\partial z} = \mathbf{b}_z^n = 0 \quad \text{at} \quad z = \mp 1. \quad (2.77)$$

Before the application of Galerkin projection, the equations (2.70) to (2.73) should be rewritten in terms of Fourier coefficients. For each wave index pair  $(m,n)$ , the differentiation in the horizontal directions can be expressed in the form of product with the wave numbers:

$$\mathfrak{S} \left\{ \frac{\partial}{\partial x} \begin{bmatrix} \mathbf{u} \\ \Theta \\ \mathbf{b} \\ \Pi \end{bmatrix} (x, y, z, t) \right\} = i m \zeta \begin{bmatrix} \hat{\mathbf{u}} \\ \hat{\Theta} \\ \hat{\mathbf{b}} \\ \hat{\Pi} \end{bmatrix} (m, n, z, t) = i k_x \begin{bmatrix} \hat{\mathbf{u}} \\ \hat{\Theta} \\ \hat{\mathbf{b}} \\ \hat{\Pi} \end{bmatrix}, \quad (2.78)$$

in  $x$  and

$$\mathfrak{S} \left\{ \frac{\partial}{\partial y} \begin{bmatrix} \mathbf{u} \\ \Theta \\ \mathbf{b} \\ \Pi \end{bmatrix} (x, y, z, t) \right\} = i n \eta \begin{bmatrix} \hat{\mathbf{u}} \\ \hat{\Theta} \\ \hat{\mathbf{b}} \\ \hat{\Pi} \end{bmatrix} (m, n, z, t) = i k_y \begin{bmatrix} \hat{\mathbf{u}} \\ \hat{\Theta} \\ \hat{\mathbf{b}} \\ \hat{\Pi} \end{bmatrix} \quad (2.79)$$

in  $y$  directions. Here,  $\mathfrak{S}$  is the fourier operator and  $k_x = m\zeta$  and  $k_y = n\eta$  are the wave numbers in  $x$  and  $y$  directions, respectively.

After substitution of (2.78) and (2.79), the system of partial differential equations from (2.70) to (2.73) are represented in Fourier space as:

$$ik_x \hat{\mathbf{u}}_x^{n+1} + ik_y \hat{\mathbf{u}}_y^{n+1} + \frac{\partial}{\partial z} \hat{\mathbf{u}}_z^{n+1} = 0, \quad (2.80)$$

$$\left( \text{Pr} \left( \frac{\partial^2}{\partial z^2} - k^2 \right) - \frac{2}{\Delta t} \right) \hat{\mathbf{u}}_x^{n+1} = ik_x \hat{\Pi}^{n+1} + \hat{\mathbf{g}}_x^n, \quad (2.81)$$

$$\left( \text{Pr} \left( \frac{\partial^2}{\partial z^2} - k^2 \right) - \frac{2}{\Delta t} \right) \hat{\mathbf{u}}_y^{n+1} = ik_y \hat{\Pi}^{n+1} + \hat{\mathbf{g}}_y^n, \quad (2.82)$$

$$\left( \text{Pr} \left( \frac{\partial^2}{\partial z^2} - k^2 \right) - \frac{2}{\Delta t} \right) \hat{\mathbf{u}}_z^{n+1} = \frac{\partial}{\partial z} \hat{\Pi}^{n+1} + \hat{\mathbf{g}}_z^n, \quad (2.83)$$

$$\left( \text{Pr} \left( \frac{\partial^2}{\partial z^2} - k^2 \right) - \frac{2}{\Delta t} \right) \hat{\Theta}^{n+1} = \hat{f}^n, \quad (2.84)$$

$$\left( \frac{\partial^2}{\partial z^2} - k^2 \right) \hat{\mathbf{b}}_x^n = \hat{\mathbf{q}}_x^n, \quad (2.85)$$

$$\left( \frac{\partial^2}{\partial z^2} - k^2 \right) \hat{\mathbf{b}}_y^n = \hat{\mathbf{q}}_y^n, \quad (2.86)$$

$$\left( \frac{\partial^2}{\partial z^2} - k^2 \right) \hat{\mathbf{b}}_z^n = \hat{\mathbf{q}}_z^n, \quad (2.87)$$

where  $\hat{\mathbf{g}}^n, \hat{f}^n$  and  $\hat{\mathbf{q}}^n$  are the forcing terms from (2.74) to (2.76) in Fourier space:

$$\begin{aligned} \hat{\mathbf{g}}^n = & -3 \left( \Im \{ \mathbf{u} \times \boldsymbol{\omega} \} + \text{PrRa}^* \hat{\Theta} \mathbf{e}_z + \text{Q}^* \text{Pr} \left[ \text{Cos} \chi (ik_y) + \text{Sin} \chi \frac{\partial}{\partial z} \right] \hat{\mathbf{b}} \right)^n \\ & + \left( \Im \{ \mathbf{u} \times \boldsymbol{\omega} \} + \text{PrRa}^* \hat{\Theta} \mathbf{e}_z + \text{Q}^* \text{Pr} \left[ \text{Cos} \chi (ik_y) + \text{Sin} \chi \frac{\partial}{\partial z} \right] \hat{\mathbf{b}} \right)^{n-1} \\ & + \Im \{ \nabla \} \hat{\Pi}^n - \left( \text{Pr} \left[ \frac{\partial^2}{\partial z^2} - k^2 \right] + \frac{2}{\Delta t} \right) \hat{\mathbf{u}}^n, \end{aligned} \quad (2.88)$$

$$\hat{\mathbf{f}}^n = -3\left(\mathbf{e}_z \frac{\hat{\mathbf{u}}}{2} - \mathfrak{S}\{(\mathbf{u} \cdot \nabla)\Theta\}\right)^n + \left(\mathbf{e}_z \frac{\hat{\mathbf{u}}}{2} - \mathfrak{S}\{(\mathbf{u} \cdot \nabla)\Theta\}\right)^{n-1} - \left(\frac{\partial^2}{\partial z^2} - k^2 + \frac{2}{\Delta t}\right)\hat{\Theta}^n \quad (2.89)$$

and

$$\hat{\mathbf{q}}^n = -\left[\text{Cos}\chi(ik_y) + \text{Sin}\chi \frac{\partial}{\partial z}\right]\hat{\mathbf{u}}^n. \quad (2.90)$$

Here,  $\mathfrak{S}\{\nabla\} = (im\zeta, in\eta, \partial/\partial z)$  and  $\mathfrak{S}\{\nabla^2\} = \partial^2/\partial z^2 - k^2$  are representations of the gradient and laplacian operators in Fourier space and  $k^2 = k_x^2 + k_y^2$ . Boundary conditions become:

$$\hat{\mathbf{u}}^{n+1} = \hat{\Theta}^{n+1} = 0 \quad \text{and} \quad \frac{\partial}{\partial z} \hat{\mathbf{b}}_x^n = \frac{\partial}{\partial z} \hat{\mathbf{b}}_y^n = \hat{\mathbf{b}}_z^n = 0 \quad \text{at } z = \mp 1. \quad (2.91)$$

In this multi-step scheme, there exists a difficulty at the beginning stage ( $t = 0$ ) because the only known values of the variables are those:

$$\hat{\mathbf{u}}^0 = \hat{\mathbf{u}}(m, n, z, 0), \quad (2.92)$$

$$\hat{\Theta}^0 = \hat{\Theta}(m, n, z, 0), \quad (2.93)$$

$$\hat{\mathbf{b}}^0 = \hat{\mathbf{b}}(m, n, z, 0), \quad (2.94)$$

However, the scheme needs two levels of starting values in order to determine,  $\hat{\mathbf{u}}^n$ ,  $\hat{\Theta}^n$  and  $\hat{\mathbf{b}}^n$  at the later stages. To overcome this problem, it is necessary to apply a starting scheme for the first step. In this study, first order forward Euler is implemented. Manipulation of equations from (2.28) to (2.32) towards implementing Forward Euler results in a change in  $\hat{\mathbf{g}}^0$  and  $\hat{\mathbf{f}}^0$  as:

$$\hat{\mathbf{g}}^0 = -2\left(\mathfrak{S}\{\mathbf{u} \times \boldsymbol{\omega}\} + \text{Pr Ra}^* \hat{\Theta}^0 \mathbf{e}_z + \text{Q}^* \text{Pr} \left[\text{Cos}\chi(ik_y) + \text{Sin}\chi \frac{\partial}{\partial z}\right] \hat{\mathbf{b}}^0\right)^0 + \hat{\nabla} \hat{\Pi}^0 - \left(\text{Pr} \hat{\nabla}^2 + \frac{2}{\Delta t}\right) \hat{\mathbf{u}}^0, \quad (2.95)$$

$$\hat{f}^0 = -2 \left( \mathbf{e}_z \frac{\hat{\mathbf{u}}}{2} - \mathfrak{S}\{(\mathbf{u} \cdot \nabla)\Theta\} \right)^0 - \left( \hat{\nabla}^2 + \frac{2}{\Delta t} \right) \hat{\Theta}^0 \quad (2.96)$$

Due to the way that the nonlinear terms are treated in (2.88) and (2.89), de-aliasing is required at each time step. Multiplication of flow variables generates coefficients at high wave numbers; this creates a wholly unphysical transfer of energy from high wave numbers to low called aliasing. Parts of arrays are set to zero for wave numbers;  $|m| > N_x/3$  and  $|n| > N_y/3$  towards eliminating aliasing in [19]. In this study, loop over mode pairs  $(m,n)$  is performed only on surviving modes to save time instead of working on non-zero modes and subsequently filtering them out.

## CHAPTER 3

### WEAK FORMULATION OF EQUATIONS

Equations from (2.80) to (2.87) are discretized by following a variational method, Galerkin procedure. While Legendre polynomials (2.51) are chosen as test functions for the continuity equation (2.80), variational forms of the momentum conservation, heat transport and hydromagnetic equations are obtained by the inner product of rescaled Lagrange-Legendre interpolants (2.62) with the equations (2.81) to (2.87). Due to the homogeneous Dirichlet boundary conditions at  $z = \mp 1$  for velocity, temperature variables and the  $z$  component of the induced magnetic field, the test functions are selected to satisfy Dirichlet boundary conditions automatically which amounts to excluding those interpolants with indices corresponding to the boundary nodes. On the other hand, the unknown values of  $x$  and  $y$  components of the induced magnetic field at the  $z$  boundaries for which Neumann conditions are specified, are included in the computations by selecting the whole range of the Lagrange interpolants as test functions:

$$\int_{-1}^1 L_{i-1}(z) \left[ ik_x \hat{\mathbf{u}}_x^{n+1} + ik_y \hat{\mathbf{u}}_y^{n+1} + \frac{\partial}{\partial z} \hat{\mathbf{u}}_z^{n+1} \right] dz = 0, \quad (3.1)$$

$$\int_{-1}^1 \bar{h}_i(z) \left[ \text{Pr} \left( \frac{\partial^2}{\partial z^2} - k^2 \right) - \frac{2}{\Delta t} \right] \hat{\mathbf{u}}_x^{n+1} dz = \int_{-1}^1 \bar{h}_i(z) ( ik_x \hat{\Pi}^{n+1} + \hat{\mathbf{g}}_x^n ) dz, \quad (3.2)$$

$$\int_{-1}^1 \bar{h}_i(z) \left[ \text{Pr} \left( \frac{\partial^2}{\partial z^2} - k^2 \right) - \frac{2}{\Delta t} \right] \hat{\mathbf{u}}_y^{n+1} dz = \int_{-1}^1 \bar{h}_i(z) ( ik_y \hat{\Pi}^{n+1} + \hat{\mathbf{g}}_y^n ) dz, \quad (3.3)$$

$$\int_{-1}^1 \bar{h}_i(z) \left[ \Pr \left( \frac{\partial^2}{\partial z^2} - k^2 \right) - \frac{2}{\Delta t} \right] \hat{\mathbf{u}}_z^{n+1} dz = \int_{-1}^1 \bar{h}_i(z) \left( \frac{\partial}{\partial z} \hat{\Pi}^{n+1} + \hat{\mathbf{g}}_z^n \right) dz, \quad (3.4)$$

$$\int_{-1}^1 \bar{h}_i(z) \left[ \left( \frac{\partial^2}{\partial z^2} - k^2 \right) - \frac{2}{\Delta t} \right] \hat{\Theta}^{n+1} dz = \int_{-1}^1 \bar{h}_i(z) \hat{f}^n dz, \quad (3.5)$$

$$\int_{-1}^1 \bar{h}_i(z) \left[ \left( \frac{\partial^2}{\partial z^2} - k^2 \right) - \frac{2}{\Delta t} \right] \hat{\mathbf{b}}_x^n dz = \int_{-1}^1 \bar{h}_i(z) \hat{\mathbf{q}}_x^n dz, \quad (3.6)$$

$$\int_{-1}^1 \bar{h}_i(z) \left[ \left( \frac{\partial^2}{\partial z^2} - k^2 \right) - \frac{2}{\Delta t} \right] \hat{\mathbf{b}}_y^n dz = \int_{-1}^1 \bar{h}_i(z) \hat{\mathbf{q}}_y^n dz, \quad (3.7)$$

$$\int_{-1}^1 \bar{h}_i(z) \left[ \left( \frac{\partial^2}{\partial z^2} - k^2 \right) - \frac{2}{\Delta t} \right] \hat{\mathbf{b}}_z^n dz = \int_{-1}^1 \bar{h}_i(z) \hat{\mathbf{q}}_z^n dz, \quad (3.8)$$

where  $0 < i < N_z$  and  $0 \leq l \leq N_z$ .

Integration by parts reduces second order  $z$  derivatives and subsequently, the system of partial differential equations for the momentum conservation (3.2)-(3.4), the heat transport (3.5) and the hydromagnetic (3.6)-(3.8) equations are rewritten in to the form of:

$$\begin{aligned} \int_{-1}^1 \left[ -\Pr \left( \bar{h}_i'(z) \frac{\partial}{\partial z} + k^2 \bar{h}_i(z) \right) - \frac{2}{\Delta t} \bar{h}_i(z) \right] \hat{\mathbf{u}}_x^{n+1} dz + \Pr \bar{h}_i(z) \frac{\partial}{\partial z} \hat{\mathbf{u}}_x^{n+1} \Big|_{-1}^{+1} \\ = \int_{-1}^1 \bar{h}_i(z) \left( ik_x \hat{\Pi}^{n+1} + \hat{\mathbf{g}}_x^n \right) dz, \end{aligned} \quad (3.9)$$

$$\begin{aligned} \int_{-1}^1 \left[ -\Pr \left( \bar{h}_i'(z) \frac{\partial}{\partial z} + k^2 \bar{h}_i(z) \right) - \frac{2}{\Delta t} \bar{h}_i(z) \right] \hat{\mathbf{u}}_y^{n+1} dz + \Pr \bar{h}_i(z) \frac{\partial}{\partial z} \hat{\mathbf{u}}_y^{n+1} \Big|_{-1}^{+1} \\ = \int_{-1}^1 \bar{h}_i(z) \left( ik_y \hat{\Pi}^{n+1} + \hat{\mathbf{g}}_y^n \right) dz, \end{aligned} \quad (3.10)$$

$$\begin{aligned} \int_{-1}^1 \left[ -\Pr \left( \bar{h}_i'(z) \frac{\partial}{\partial z} + k^2 \bar{h}_i(z) \right) - \frac{2}{\Delta t} \bar{h}_i(z) \right] \hat{\mathbf{u}}_z^{n+1} dz + \Pr \bar{h}_i(z) \frac{\partial}{\partial z} \hat{\mathbf{u}}_z^{n+1} \Big|_{-1}^{+1} \\ = \int_{-1}^1 \left( -\bar{h}_i'(z) \hat{\Pi}^{n+1} + \bar{h}_i(z) \hat{\mathbf{g}}_z^n \right) dz + \bar{h}_i(z) \hat{\Pi}^{n+1} \Big|_{-1}^{+1}, \end{aligned} \quad (3.11)$$

$$\int_{-1}^1 - \left[ \bar{h}_i'(z) + \left( k^2 - \frac{2}{\Delta t} \right) \bar{h}_i(z) \right] \hat{\Theta}^{n+1} dz + \bar{h}_i(z) \frac{\partial}{\partial z} \hat{\Theta}^{n+1} \Big|_{-1}^{+1} = \int_{-1}^1 \bar{h}_i(z) \hat{f}^n dz, \quad (3.12)$$

$$\int_{-1}^1 - \left[ \bar{h}_l'(z) + \left( \frac{2}{\Delta t} - k^2 \right) \bar{h}_l(z) \right] \hat{\mathbf{b}}_x^n dz + \bar{h}_l(z) \frac{\partial}{\partial z} \hat{\mathbf{b}}_x^n \Big|_{-1}^{+1} = \int_{-1}^1 \bar{h}_l(z) \hat{\mathbf{q}}_x^n dz, \quad (3.13)$$

$$\int_{-1}^1 - \left[ \bar{h}_l'(z) + \left( \frac{2}{\Delta t} - k^2 \right) \bar{h}_l(z) \right] \hat{\mathbf{b}}_y^n dz + \bar{h}_l(z) \frac{\partial}{\partial z} \hat{\mathbf{b}}_y^n \Big|_{-1}^{+1} = \int_{-1}^1 \bar{h}_l(z) \hat{\mathbf{q}}_y^n dz, \quad (3.14)$$

$$\int_{-1}^1 - \left[ \bar{h}_i'(z) + \left( \frac{2}{\Delta t} - k^2 \right) \bar{h}_i(z) \right] \hat{\mathbf{b}}_z^n dz + \bar{h}_i(z) \frac{\partial}{\partial z} \hat{\mathbf{b}}_z^n \Big|_{-1}^{+1} = \int_{-1}^1 \bar{h}_i(z) \hat{\mathbf{q}}_z^n dz. \quad (3.15)$$

Here, prime denotes derivative with respect to  $z$ . Boundary terms in the equations (3.9)-(3.15) vanish due to the homogeneous boundary conditions (2.91) and:

$$\bar{h}_i(\pm 1) = 0 \quad \text{for} \quad 0 < i < N_z. \quad (3.16)$$

The derivative of rescaled Legendre–Lagrange interpolants is found in literature to be:

$$\bar{h}_i'(z) = \begin{cases} \frac{1}{\sqrt{w_i}} \frac{L_{N_z}(z)}{L_{N_z}(z_i)(z-z_i)} & z \neq z_i, \\ 0 & z = z_i \neq 0, N_z, \\ -\frac{N_z(N_z+1)}{4\sqrt{w_i}} & \text{if } z = z_i = 0, \\ \frac{N_z(N_z+1)}{4\sqrt{w_i}} & z = z_j = N_z. \end{cases} \quad (3.17)$$

After the substitution of the expansion in terms of rescaled Legendre Lagrange interpolants (2.63) and Legendre polynomials (2.64), the equations (3.9) to (3.15) are rewritten in the form:

$$\int_{-1}^1 L_{i-1}(z) \left[ ik_x \bar{h}_j(z) \bar{\mathbf{u}}_{xj}^{n+1} + ik_y \bar{h}_j(z) \bar{\mathbf{u}}_{yj}^{n+1} + \bar{h}_j'(z) \bar{\mathbf{u}}_{zj}^{n+1} \right] dz = 0, \quad (3.18)$$

$$\begin{aligned} \int_{-1}^1 \left[ -\Pr \left( \bar{h}_i'(z) \bar{h}_j'(z) + k^2 \bar{h}_i(z) \bar{h}_j(z) \right) - \frac{2}{\Delta t} \bar{h}_i(z) \bar{h}_j(z) \right] \bar{\mathbf{u}}_{xj}^{n+1} dz \\ = \int_{-1}^1 \bar{h}_i(z) \left( ik_x L_{j-1}(z) \bar{\Pi}_j^{n+1} + \bar{h}_j(z) \bar{\mathbf{g}}_{xj}^n \right) dz, \end{aligned} \quad (3.19)$$

$$\begin{aligned} \int_{-1}^1 \left[ -\Pr \left( \bar{h}_i'(z) \bar{h}_j'(z) + k^2 \bar{h}_i(z) \bar{h}_j(z) \right) - \frac{2}{\Delta t} \bar{h}_i(z) \bar{h}_j(z) \right] \bar{\mathbf{u}}_{yj}^{n+1} dz \\ = \int_{-1}^1 \bar{h}_i(z) \left( ik_y L_{j-1}(z) \bar{\Pi}_j^{n+1} + \bar{h}_j(z) \bar{\mathbf{g}}_{yj}^n \right) dz, \end{aligned} \quad (3.20)$$

$$\begin{aligned} \int_{-1}^1 \left[ -\Pr \left( \bar{h}_i'(z) \bar{h}_j'(z) + k^2 \bar{h}_i(z) \bar{h}_j(z) \right) - \frac{2}{\Delta t} \bar{h}_i(z) \bar{h}_j(z) \right] \bar{\mathbf{u}}_{zj}^{n+1} dz \\ = \int_{-1}^1 \left( -\bar{h}_i'(z) L_{j-1}(z) \bar{\Pi}_j^{n+1} + \bar{h}_i(z) \bar{h}_j(z) \bar{\mathbf{g}}_{zj}^n \right) dz, \end{aligned} \quad (3.21)$$

$$\int_{-1}^1 - \left[ \bar{h}_i'(z) \bar{h}_j(z) + \left( k^2 - \frac{2}{\Delta t} \right) \bar{h}_i(z) \bar{h}_j(z) \right] \bar{\Theta}_j^{n+1} dz = \int_{-1}^1 \bar{h}_i(z) \bar{h}_j(z) \bar{\mathbf{f}}_j^n dz, \quad (3.22)$$

$$\int_{-1}^1 - \left[ \bar{h}_i'(z) \bar{h}_p(z) + \left( \frac{2}{\Delta t} - k^2 \right) \bar{h}_i(z) \bar{h}_p(z) \right] \bar{\mathbf{b}}_{xp}^n dz = \int_{-1}^1 \bar{h}_i(z) \bar{h}_p(z) \bar{\mathbf{q}}_{xp}^n dz, \quad (3.23)$$

$$\int_{-1}^1 - \left[ \bar{h}_i'(z) \bar{h}_p(z) + \left( \frac{2}{\Delta t} - k^2 \right) \bar{h}_i(z) \bar{h}_p(z) \right] \bar{\mathbf{b}}_{yp}^n dz = \int_{-1}^1 \bar{h}_i(z) \bar{h}_p(z) \bar{\mathbf{q}}_{yp}^n dz, \quad (3.24)$$

$$\int_{-1}^1 - \left[ \bar{h}_i'(z) \bar{h}_j(z) + \left( \frac{2}{\Delta t} - k^2 \right) \bar{h}_i(z) \bar{h}_j(z) \right] \bar{\mathbf{b}}_{zj}^n dz = \int_{-1}^1 \bar{h}_i(z) \bar{h}_j(z) \bar{\mathbf{q}}_{zj}^n dz \quad (3.25)$$

for  $0 < i < N_z$ ,  $0 < j < N_z$  and  $0 \leq l \leq N_z$ ,  $0 \leq p \leq N_z$ .

It should be noticed that  $\hat{\mathbf{b}}_x$  and  $\hat{\mathbf{b}}_y$ ;  $\hat{\mathbf{b}}_{x0}$ ,  $\hat{\mathbf{b}}_{xN_z}$  and  $\hat{\mathbf{b}}_{y0}$ ,  $\hat{\mathbf{b}}_{yN_z}$  are non-zero values therefore Lorentz forcing terms in  $\hat{\mathbf{g}}_x$  and  $\hat{\mathbf{g}}_y$  are evaluated on  $N_z + 1$  nodes. Using Gauss-Lobatto quadrature, the integrals in  $z$  are computed:

$$A_{ij} = \int_{-1}^1 \bar{h}_i'(z) \bar{h}_j'(z) dz = \sum_{k=0}^{N_z} w_k \bar{h}_i'(z_k) \bar{h}_j'(z_k), \quad (3.26)$$

$$B_{ij} = \int_{-1}^1 \bar{h}_i(z) \bar{h}_j(z) dz = \sum_{k=0}^{N_z} w_p \bar{h}_i(z_k) \bar{h}_j(z_k) = \delta_{ij}, \quad (3.27)$$

$$C_{ij} = \int_{-1}^1 \bar{h}_i(z) L_{j-1}(z) dz = \sum_{k=0}^{N_z} w_p \bar{h}_i(z_k) L_{j-1}(z_k) = \sqrt{w_i} L_{j-1}(z_i), \quad (3.28)$$

$$D_{ij} = \int_{-1}^1 \bar{h}_i'(z) L_{j-1}(z) dz = \sum_{k=0}^{N_z} w_k \bar{h}_i'(z_k) L_{j-1}(z_k). \quad (3.29)$$

Here, the range of the indices  $i$  and  $j$  include the boundary points in (3.23) and (3.24). Coefficient matrices  $A$ ,  $B$ ,  $C$  and  $D$  in (3.26) to (3.29) represent the discrete form of the differential operators. As an advantage of using the rescaled Lagrange Legendre interpolants,  $B$  turns out to be an identity matrix,  $I$  which creates a simplification in the computations (3.27).

Substitution of (3.26)-(3.29) into (3.18)-(3.25) result in:

$$ik_x C^T \bar{\mathbf{u}}_x^{n+1} + ik_y C^T \bar{\mathbf{u}}_y^{n+1} + D^T \bar{\mathbf{u}}_z^{n+1} = 0, \quad (3.30)$$

$$-\left[ \text{Pr}A + \left( \text{Pr}k^2 + \frac{2}{\Delta t} \right) I \right] \bar{\mathbf{u}}_x^{n+1} = ik_x C \bar{\Pi}^{n+1} + \bar{\mathbf{g}}_x^n, \quad (3.31)$$

$$-\left[ \text{Pr}A + \left( \text{Pr}k^2 + \frac{2}{\Delta t} \right) I \right] \bar{\mathbf{u}}_y^{n+1} = ik_y C \bar{\Pi}^{n+1} + \bar{\mathbf{g}}_y^n, \quad (3.32)$$

$$-\left[ \text{Pr}A + \left( \text{Pr}k^2 + \frac{2}{\Delta t} \right) I \right] \bar{\mathbf{u}}_z^{n+1} = -D \bar{\Pi}^{n+1} + \bar{\mathbf{g}}_z^n, \quad (3.33)$$

$$-\left[ A + \left( k^2 + \frac{2}{\Delta t} \right) I \right] \bar{\Theta}^{n+1} = \bar{f}^n, \quad (3.34)$$

$$-\left[ A + k^2 I \right] \bar{\mathbf{b}}_x^n = \bar{\mathbf{q}}_x^n, \quad (3.35)$$

$$-\left[ A + k^2 I \right] \bar{\mathbf{b}}_y^n = \bar{\mathbf{q}}_y^n, \quad (3.36)$$

$$-\left[ A + k^2 I \right] \bar{\mathbf{b}}_z^n = \bar{\mathbf{q}}_z^n. \quad (3.37)$$

The solution strategy follows from earlier studies on the numerical solution of Navier Stokes equations as in the Uzawa technique [25] and in Guessous' work [19]. In this

strategy, the momentum equations (3.31)-(3.33) are solved for the velocity in each direction and for each  $(k_x, k_y)$  pair:

$$\bar{\mathbf{u}}_x^{n+1} = H_U^{-1} \left( ik_x C \bar{\Pi}^{n+1} + \bar{\mathbf{g}}_x^n \right), \quad (3.38)$$

$$\bar{\mathbf{u}}_y^{n+1} = H_U^{-1} \left( ik_y C \bar{\Pi}^{n+1} + \bar{\mathbf{g}}_y^n \right), \quad (3.39)$$

$$\bar{\mathbf{u}}_z^{n+1} = H_U^{-1} \left( -D \bar{\Pi}^{n+1} + \bar{\mathbf{g}}_z^n \right) \quad (3.40)$$

and similarly (3.34) for the temperature field:

$$\bar{\Theta}^{n+1} = H_\Theta^{-1} \bar{\mathbf{f}}^n \quad (3.41)$$

and (3.35)-(3.37) for the induced magnetic field:

$$\bar{\mathbf{b}}_x^n = -H_B^{-1} \bar{\mathbf{q}}_x^n, \quad (3.42)$$

$$\bar{\mathbf{b}}_y^n = -H_B^{-1} \bar{\mathbf{q}}_y^n, \quad (3.43)$$

$$\bar{\mathbf{b}}_z^n = -H_B^{-1} \bar{\mathbf{q}}_z^n. \quad (3.44)$$

Here,  $H_U$ ,  $H_\Theta$  and  $H_B$  in (3.44) are  $(N_z - 1) \times (N_z - 1)$  discrete Helmholtz operators. (3.42) and (3.43) are solved for the boundary values of  $\bar{\mathbf{b}}_x$  and  $\bar{\mathbf{b}}_y$  therefore  $H_B$  is a  $(N_z + 1) \times (N_z + 1)$  matrix for these equations:

$$H_U = - \left[ \text{Pr} A + \left( \text{Pr} k^2 + \frac{2}{\Delta t} \right) I \right], \quad (3.45)$$

$$H_\Theta = - \left[ A + \left( k^2 + \frac{2}{\Delta t} \right) I \right], \quad (3.46)$$

$$H_B = - \left[ A + k^2 I \right]. \quad (3.47)$$

Substitution of the matrix equations (3.38)-(3.40) into the continuity equation (3.30) provides the discrete equation to solve for the pressure at time level  $n+1$ :

$$S \bar{\Pi}^{n+1} = \bar{\mathbf{G}}^n, \quad (3.48)$$

where  $S$  is the pressure operator,  $\bar{\mathbf{G}}^n$  is the right hand side vector at time level  $n$ :

$$S = - \left( k^2 C^T H_U^{-1} C + D^T H_U^{-1} D \right), \quad (3.49)$$

$$\bar{G}^n = -ik_x C^T H_U^{-1} \bar{g}_x^n - ik_y C^T H_U^{-1} \bar{g}_y^n - D^T H_U^{-1} \bar{g}_z^n. \quad (3.50)$$

After solving (3.48) for the pressure, updated values for the velocity field are obtained by inserting the pressure in to equations from (3.38) to (3.40). Temperature field involves the third component of the velocity field, therefore, new values for temperature field are obtained by substituting into (3.41).

### 3.1 Inverse of Helmholtz Operators

Here, for inverting the Helmholtz operators (3.45), (3.46) and (3.47), an efficient technique, namely, collocation diagonalization method [26] is performed. The key in the performance of this technique is the use of the rescaled Lagrangian interpolant expansion functions and subsequently having the mass matrix  $B$  as identity. This way the cost of the inversion is reduced from  $O(N_z^3)$  to  $O(N_z^2)$  arithmetic operations in the overall numerical scheme. First, the symmetric second order derivative matrix  $A$  is factorized by using similarity transformations, such that:

$$A = E G E^{-1}. \quad (3.51)$$

Here,  $G$  is the diagonal matrix in which the diagonal elements are the eigenvalues of  $A$  and  $E$  contains the corresponding eigenvectors as its columns.

Substitution of (3.51) into (3.45) gives:

$$H_U = - \left[ \text{Pr } E G E^{-1} + \left( \text{Pr } k^2 + \frac{2}{\Delta t} \right) I \right], \quad (3.52)$$

And finally, manipulating the equation gives the inverse in a simpler form, such that:

$$E^{-1}H_U = -\left[Pr G E^{-1} + E^{-1}\left(Pr k^2 + \frac{2}{\Delta t}\right)I\right] \quad (3.53)$$

or

$$E^{-1}H_U = -\left[Pr G + \left(Pr k^2 + \frac{2}{\Delta t}\right)I\right]E^{-1}. \quad (3.54)$$

Then

$$-E\left[Pr G + \left(Pr k^2 + \frac{2}{\Delta t}\right)I\right]^{-1}E^{-1}H_U = I, \quad (3.55)$$

$$H_U^{-1} = -E\left[Pr G + \left(Pr k^2 + \frac{2}{\Delta t}\right)I\right]^{-1}E^{-1}. \quad (3.56)$$

For each  $k^2$ , only a diagonal matrix is to be inverted. Similarly, the other operators can also be inverted in this way:

$$H_\Theta^{-1} = -E\left[G + \left(Pr k^2 + \frac{2}{\Delta t}\right)I\right]^{-1}E^{-1}, \quad (3.57)$$

$$H_B^{-1} = -E\left[G + k^2 I\right]^{-1}E^{-1}. \quad (3.58)$$

### 3.2 Solution for the Pressure

Unlike the sparse systems of equations produced by finite differences or finite elements, spectral element technique which uses a global approximation for each node leads full matrices. To solve the pressure equation (3.48), pressure operator,  $S$  (3.49) should be inverted for each wave number pair which is numerically costly. Here, solution of the pressure equation is obtained by Minimum Residual Richardson (MRR) algorithm which is also applied in the pure convection case in Guessous' work [19]. This algorithm presents a preconditioned iterative scheme which costs only

$O(N^2)$  flops as opposed to  $O(N^3)$  flops in using the inverse of a diagonal pre-conditioner matrix. More details of the algorithm can be found in [23].

Pressure equation (3.48) at step  $n+1$  is written symbolically for the sake of simplicity and multiplied by a preconditioning matrix:

$$\Lambda^{-1}S\bar{\Pi} = \Lambda^{-1}\bar{G}, \quad (3.59)$$

where

$$\bar{G} = \bar{G}^n, \quad (3.60)$$

$\bar{\Pi} = \bar{\Pi}^{n+1}$  is the pressure vector at time step  $n+1$  for a wave number  $k^2$  and;

$$\Lambda_{ij} = \delta_{ij}S_{ij}. \quad (3.61)$$

Here,  $\Lambda$  is the preconditioning matrix that has the diagonal elements of pseudo-spectral differential operator of the pressure equation (3.49),  $S$ .

Iteration starts at time step  $n$ , executes over a number of sub-time levels and terminates until a convergence criteria is satisfied. Therefore, this equation is subsequently discretized within the time interval  $[t^n, t^{n+1}]$  by Richardson iterative scheme:

$$\frac{\bar{\Pi}^{m+1} - \bar{\Pi}^m}{\tau^m} = -\Lambda^{-1}S\bar{\Pi}^m + \Lambda^{-1}\bar{G} \quad (3.62)$$

or

$$\bar{\Pi}^{m+1} = (I - \tau^m \Lambda^{-1}S)\bar{\Pi}^m + \tau^m \Lambda^{-1}\bar{G}. \quad (3.63)$$

where  $\tau^m$  is an optimized real parameter varying with the subsequent index  $m$ . Associated with (3.48), residual at an subsequent level  $m$ ,  $r^m$  is:

$$r^m = \bar{G} - S \bar{\Pi}^m \quad (3.64)$$

and similarly, an expression for  $r^{m+1}$  is derived by substituting (3.63) for the pressure at  $m+1$ :

$$r^{m+1} = \bar{G} - S \bar{\Pi}^{m+1} = \bar{G} - S(I - \tau^m \Lambda^{-1} S) \bar{\Pi}^m - \tau^m S \Lambda^{-1} \bar{G} \quad (3.65)$$

or, substitution of (3.64) gives a recursive relation on  $r^m$ :

$$r^{m+1} = r^m + \tau^m S \Lambda^{-1} r^m. \quad (3.66)$$

The real parameter  $\tau^m$  is obtained by mean square minimization using the inner product of residual with its complex conjugate:

$$\begin{aligned} (r^{m+1}, \bar{r}^{m+1}) = & (r^m, \bar{r}^m) + \tau^m (r^m, S \Lambda^{-1} \bar{r}^m) + \tau^m (\bar{r}^m, S \Lambda^{-1} r^m) \\ & + (\tau^m)^2 (S \Lambda^{-1} r^m, S \Lambda^{-1} \bar{r}^m), \end{aligned} \quad (3.67)$$

where overbar designates complex conjugate and  $S \Lambda^{-1}$  is a symmetric operator. Thus (3.67) is rewritten as:

$$(r^{m+1}, \bar{r}^{m+1}) = (r^m, \bar{r}^m) + 2\tau^m (r^m, S \Lambda^{-1} \bar{r}^m) + (\tau^m)^2 (S \Lambda^{-1} r^m, S \Lambda^{-1} \bar{r}^m). \quad (3.68)$$

In order to minimize (3.68) derivative with respect to  $\tau^m$  is set to 0 to yield:

$$\frac{\partial (r^{m+1}, \bar{r}^{m+1})}{\partial \tau^m} = 2(r^m, S \Lambda^{-1} \bar{r}^m) + 2(\tau^m) (S \Lambda^{-1} r^m, S \Lambda^{-1} \bar{r}^m) = 0 \quad (3.69)$$

or

$$\tau^m = \frac{(r^m, S \Lambda^{-1} \bar{r}^m)}{(S \Lambda^{-1} r^m, S \Lambda^{-1} \bar{r}^m)}. \quad (3.70)$$

Initial values of pressure are taken from the previous time step as in Guessous work [19] and (3.63) is repeated for each subsequent level  $m+1$  until residual norm (3.66) falls below a desired value (selected as  $10^{-13}$  in this work).

### 3.3 Special Cautions for Constant Term Mode

A special attention is necessary for the pressure equation (3.48) due to the singular behaviour of pressure which appears in its gradient form in the model equations and has no associated boundary conditions that is the motivation behind the expansion in terms of two order less Legendre polynomials over  $z$ . This singular behaviour due to the lack of sufficient number of constraints is reflected in pressure operator,  $S$  which is singular for  $k_x = k_y = 0$ . Therefore, following the work of Schumack [18] and Guessous [19], as an additional constraint the constant pressure mode is set to zero, without loss of generality, by modifying the matrix equation (3.48) for  $k_x = k_y = 0$ , such that:

$$S_{ij} = \begin{cases} 0 & i \neq j = 0 \\ 0 & j \neq i = 0 \\ 1 & i = j = 0 \\ S_{ij} & i \neq 0 \text{ and } j \neq 0 \end{cases} \quad \text{for } t > 0 \quad (3.71)$$

and

$$G_i = \begin{cases} 0 & i = 0 \\ G_i & i \neq 0 \end{cases} \quad \text{for } t > 0. \quad (3.72)$$

With this treatment, the first component of the unknown pressure array for the modes ( $k_x = k_y = 0$ ) is set to zero:

$$\bar{\Pi}(0,0,1,t) = 0 \quad \text{for } t > 0. \quad (3.73)$$

Similar singular behaviour is also observed in the  $x$  and  $y$  components of the induced magnetic field (3.42) and (3.43) for  $k_x = k_y = 0$ . The horizontal components of the induced magnetic field is subjected to Neumann boundary conditions.

$H_B$  for the horizontal components is a singular matrix for  $k^2 = 0$ :

$$H_B = -A. \quad (3.74)$$

Therefore, without loss of generality, hydromagnetic equation is modified preserving symmetry for  $k_x = k_y = 0$ , such that:

$$H_{Bij} = \begin{cases} 0 & \text{if } i \neq j = N_z/2 \\ 0 & \text{if } j \neq i = N_z/2 \\ 1 & \text{if } i = j = N_z/2 \\ -A_{ij} & \text{if } i \neq N_z/2 \text{ and } j \neq N_z/2 \end{cases} \quad \text{for } t > 0 \quad (3.75)$$

and

$$\bar{q}_i = \begin{cases} 0 & \text{if } i = N_z/2 \\ \bar{q}_i & \text{if } i \neq N_z/2 \end{cases} \quad \text{for } t > 0. \quad (3.76)$$

This corresponds to setting the value of the horizontal components of the induced magnetic field at the node  $z = 0$  to zero for  $(k_x = k_y = 0)$ :

$$\bar{b}_x(0,0,z_{N_z/2},t) = \bar{b}_{x_{N_z/2}} = 0 \quad \text{for } t > 0, \quad (3.77)$$

$$\bar{b}_y(0,0,z_{N_z/2},t) = \bar{b}_{y_{N_z/2}} = 0 \quad \text{for } t > 0. \quad (3.78)$$

### 3.4 Test Studies

In this section, numerical tests are performed for the consistency and the accuracy of numerical scheme. Apriori selected functions are imposed as velocity, temperature and induced magnetic solution fields by adding suitable forcing terms to the model equations. These functions satisfy the periodicity in the  $x$  and  $y$  directions, Dirichlet boundary conditions for the velocity field and the  $z$  component of the induced magnetic field and Neumann boundary conditions for

the horizontal components of the induced magnetic field (2.37). They also satisfy the divergence free condition of the velocity (2.28) and the induced magnetic fields (2.31):

$$\mathbf{u}_x^e(x, y, z, t) = -2 \sin t \cos x \cos y z (1 - z^2), \quad (3.79)$$

$$\mathbf{u}_y^e(x, y, z, t) = 2 \sin t \sin x \sin y z (1 - z^2), \quad (3.80)$$

$$\mathbf{u}_z^e(x, y, z, t) = \sin t \sin x \cos y (1 - z^2)^2, \quad (3.81)$$

$$\Theta^e(x, y, z, t) = \sin t \sin x \cos y (1 - z^2), \quad (3.82)$$

$$\mathbf{b}_x^e(x, y, z, t) = 2 \sin t \cos x \cos y \left( -\frac{3}{\sqrt{2}} \frac{e^{\sqrt{2}z} + e^{-\sqrt{2}z}}{e^{\sqrt{2}} - e^{-\sqrt{2}}} + \frac{3}{2} z^2 + 1 \right), \quad (3.83)$$

$$\mathbf{b}_y^e(x, y, z, t) = -2 \sin t \sin x \sin y \left( -\frac{3}{\sqrt{2}} \frac{e^{\sqrt{2}z} + e^{-\sqrt{2}z}}{e^{\sqrt{2}} - e^{-\sqrt{2}}} + \frac{3}{2} z^2 + 1 \right), \quad (3.84)$$

$$\mathbf{b}_z^e(x, y, z, t) = -\sin t \sin x \cos y \left( 6 \frac{e^{\sqrt{2}z} - e^{-\sqrt{2}z}}{e^{\sqrt{2}} - e^{-\sqrt{2}}} - 2z^3 - 4z \right). \quad (3.85)$$

Tests are performed at the parameter values given below:

$$\text{Ra}^* = \text{Pr} = 1, Q^* = \sqrt{3}, L_x = L_y = 2\pi, N_x = N_y = 16, N_z = 8, \Delta t = 0.005.$$

Magnetic field is applied diagonally within the convective box, therefore Lorentz forcing terms and right hand side of the hydro-magnetic equation is modified for this case.  $\hat{\mathbf{f}}_U, \hat{\mathbf{f}}_\Theta$  and  $\hat{\mathbf{f}}_b$  are the forcing terms due to test functions (3.79) to (3.85) and are produced in appendix A. Therefore (2.88), (2.89) and (2.90) are changed to:

$$\begin{aligned} \hat{\mathbf{g}}^n = & -3 \left( \mathfrak{S}\{\mathbf{u} \times \boldsymbol{\omega}\} + \text{PrRa}^* \hat{\Theta} \mathbf{e}_z + Q^* \text{Pr} \frac{1}{\sqrt{3}} \left[ ik_x + ik_y + \frac{\partial}{\partial z} \right] \hat{\mathbf{b}} + \hat{\mathbf{f}}_U \right)^n \\ & + \left( \mathfrak{S}\{\mathbf{u} \times \boldsymbol{\omega}\} + \text{PrRa}^* \hat{\Theta} \mathbf{e}_z + Q^* \text{Pr} \frac{1}{\sqrt{3}} \left[ ik_x + ik_y + \frac{\partial}{\partial z} \right] \hat{\mathbf{b}} + \hat{\mathbf{f}}_U \right)^{n-1} \quad (3.86) \\ & + \mathfrak{S}\{\nabla\} \hat{\Pi}^n - \left( \text{Pr} \left[ \frac{\partial^2}{\partial z^2} - k^2 \right] + \frac{2}{\Delta t} \right) \hat{\mathbf{u}}^n, \end{aligned}$$

$$\hat{\mathbf{f}}^n = -3 \left( \mathbf{e}_z \frac{\hat{\mathbf{u}}}{2} - \mathfrak{I}\{(\mathbf{u} \cdot \nabla)\Theta\} + \hat{\mathbf{f}}_\Theta \right)^n + \left( \mathbf{e}_z \frac{\hat{\mathbf{u}}}{2} - \mathfrak{I}\{(\mathbf{u} \cdot \nabla)\Theta\} + \hat{\mathbf{f}}_\Theta \right)^{n-1} - \left( \frac{\partial^2}{\partial z^2} - k^2 + \frac{2}{\Delta t} \right) \hat{\Theta}^n, \quad (3.87)$$

$$\hat{\mathbf{q}}^n = -\frac{1}{\sqrt{3}} \left[ ik_x + ik_y + \frac{\partial}{\partial z} \right] \hat{\mathbf{u}}^n + \hat{\mathbf{f}}_b^n. \quad (3.88)$$

Horizontal dimensions of the layer provide the periods for the trigonometric test functions ensuring periodicity for all the variables.

The computational results are plotted at a particularly chosen point  $x = \pi/4$  and  $y = \pi/4$  for all  $z$  at  $t = 5$ . Numerical results are shown by markers at the grid points superimposed over the exact profile shown by the solid line.

Absolute error in infinite norm for each variable is plotted with respect to time. Oscillatory behaviour is caused by the periodicity in time. To calculate the infinite norm each variable is reshaped into a vector form and norm is then calculated. Absolute error values show that solution for the weak formulation yields excellent results.

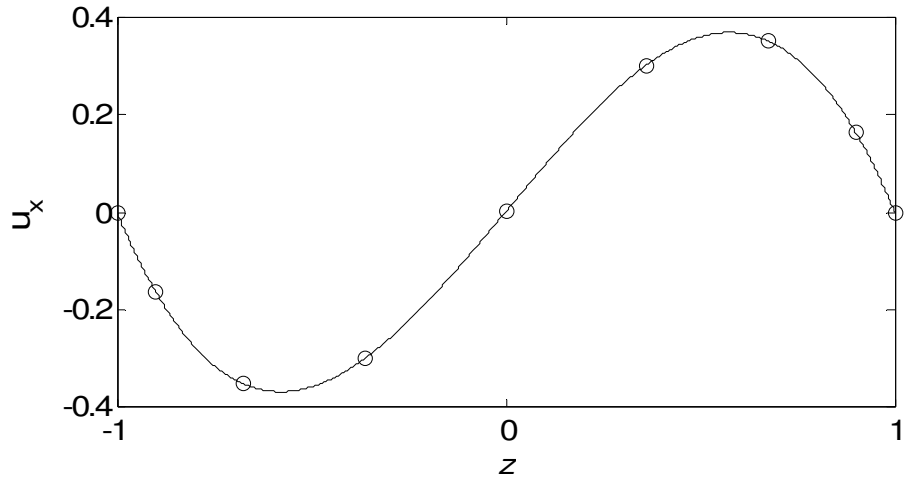


Figure 3.1  $u_x$  vs.  $z$  at  $x = \pi/4, y = \pi/4, t = 5$

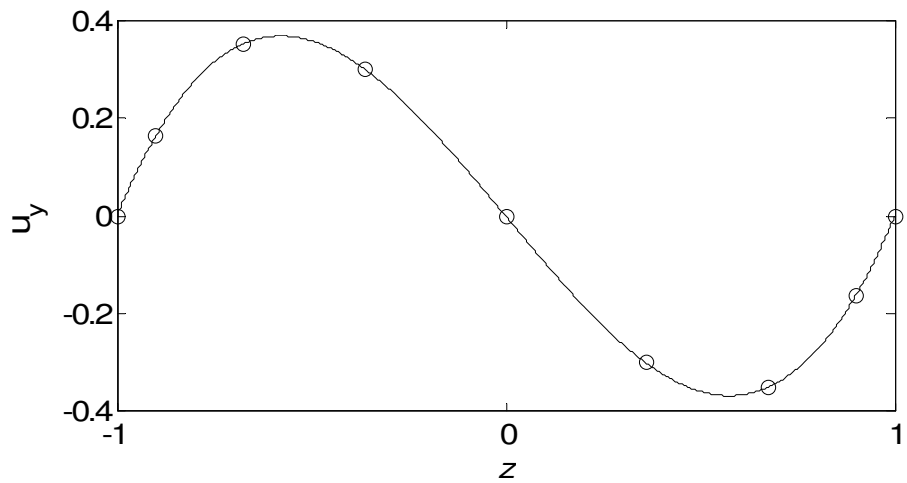


Figure 3.2  $u_y$  vs.  $z$  at  $x = \pi/4, y = \pi/4, t = 5$

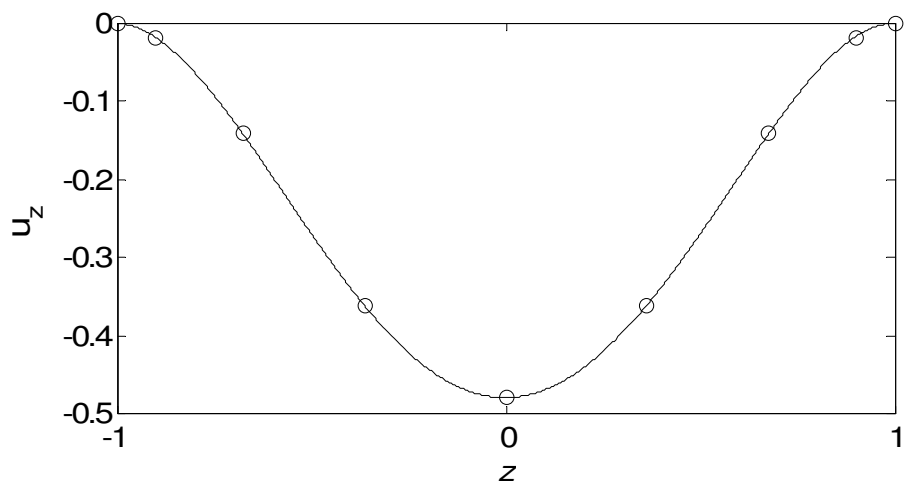


Figure 3.3  $u_z$  vs.  $z$  at  $x = \pi/4, y = \pi/4, t = 5$

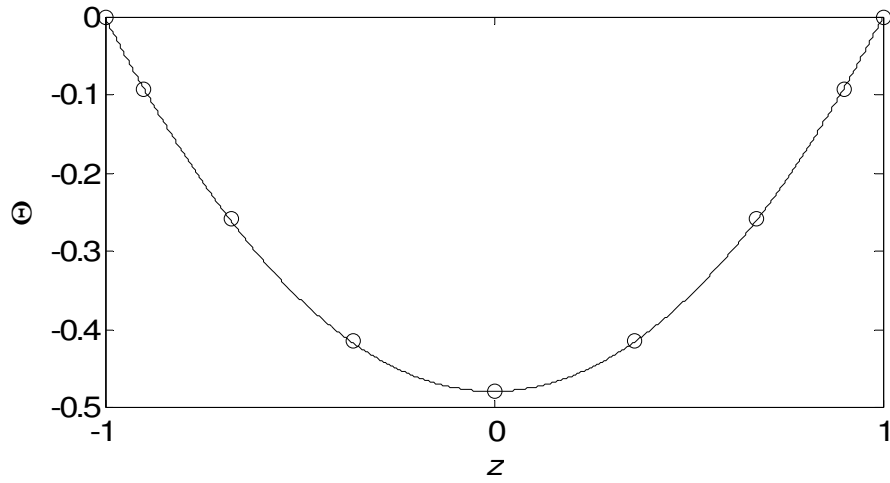


Figure 3.4  $\Theta$  vs.  $z$  at  $x = \pi/4, y = \pi/4, t = 5$

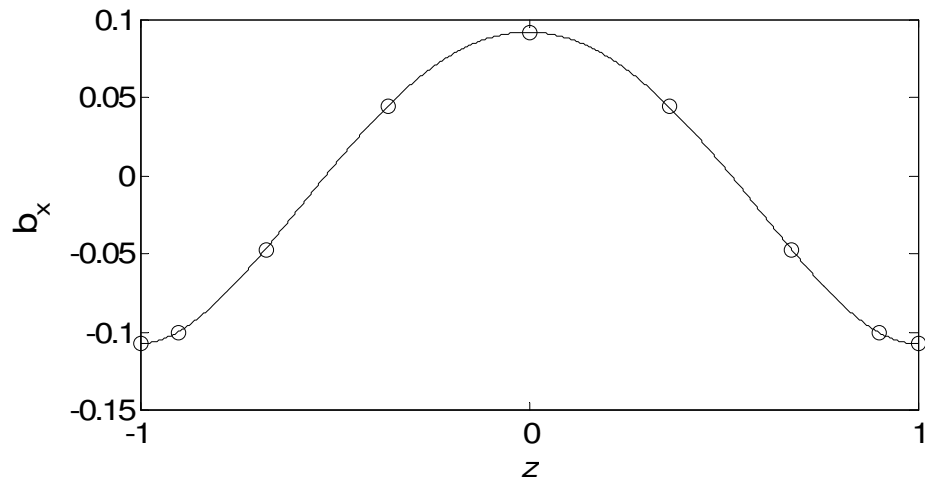


Figure 3.5  $b_x$  vs.  $z$  at  $x = \pi/4, y = \pi/4, t = 5$

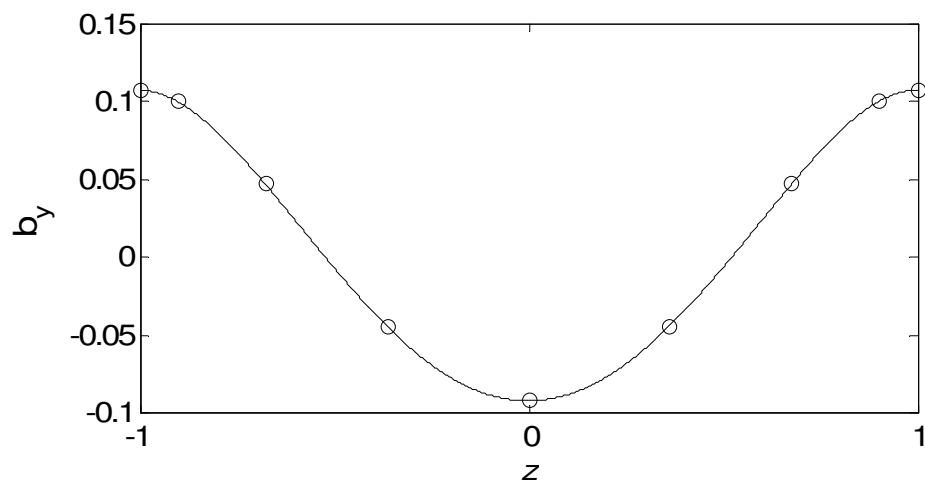


Figure 3.6  $b_y$  vs.  $z$  at  $x = \pi/4, y = \pi/4, t = 5$

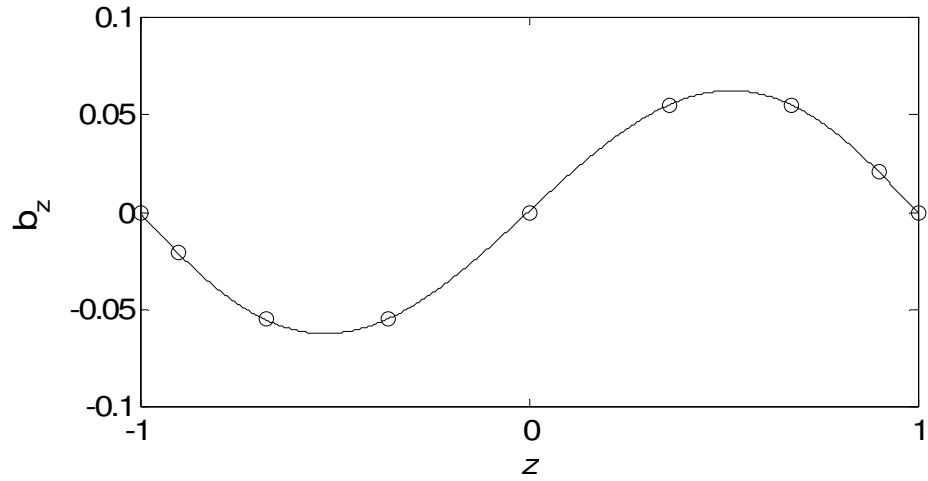


Figure 3.7  $b_z$  vs.  $z$  at  $x = \pi/4, y = \pi/4, t = 5$

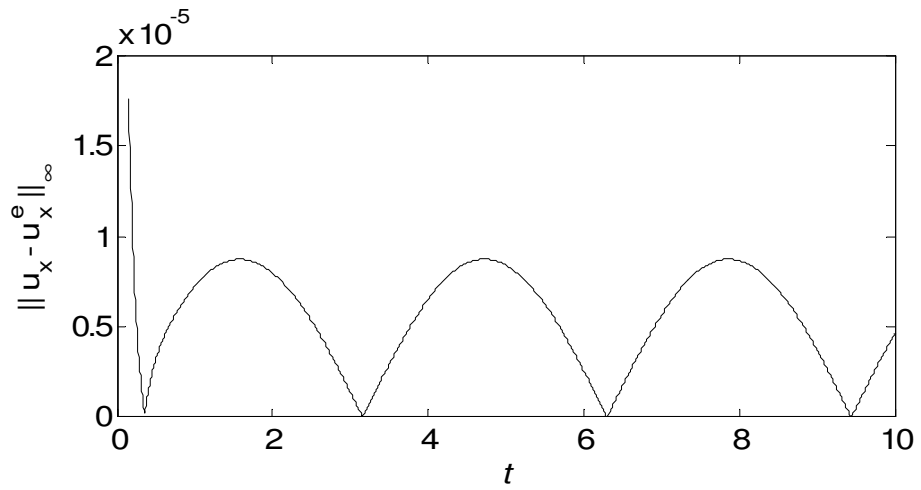


Figure 3.8 Infinite norm of error in  $\mathbf{u}_x$  vs.  $t$

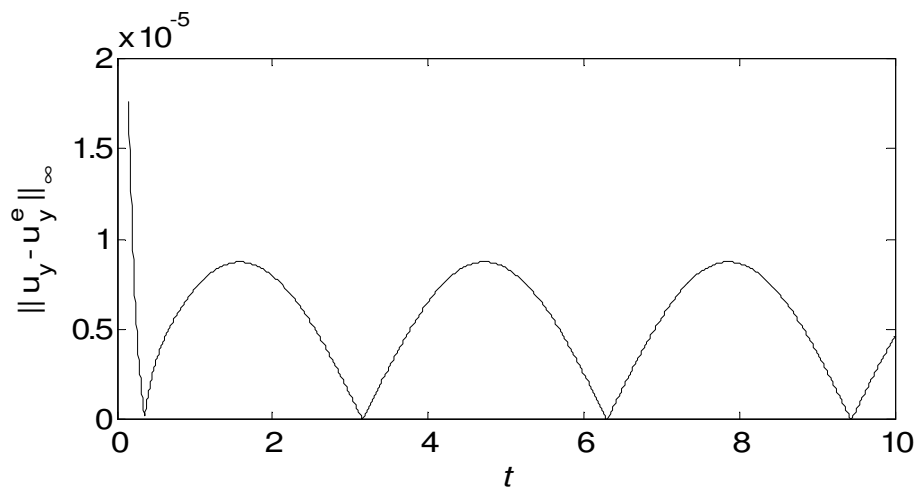


Figure 3.9 Infinite norm of error in  $\mathbf{u}_y$  vs.  $t$

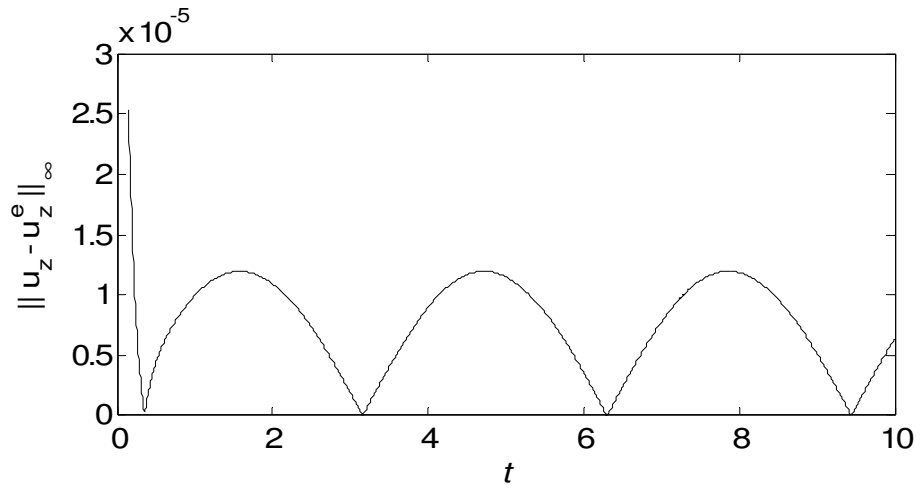


Figure 3.10 Infinite norm of error in  $u_z$  vs.  $t$

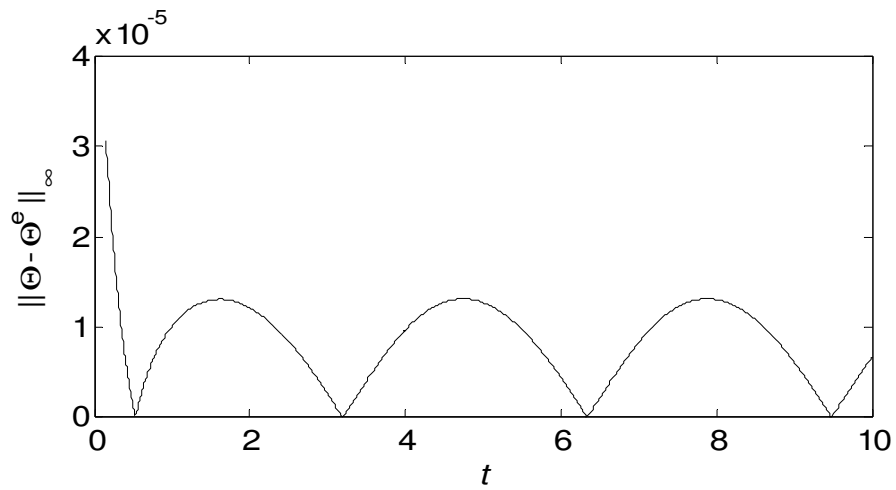


Figure 3.11 Infinite norm of error in  $\Theta$  vs.  $t$

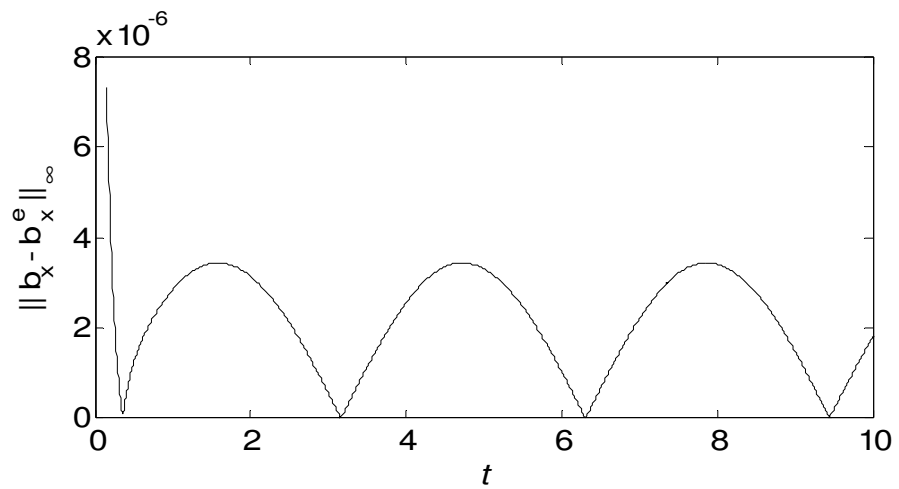


Figure 3.12 Infinite norm of error in  $b_x$  vs.  $t$

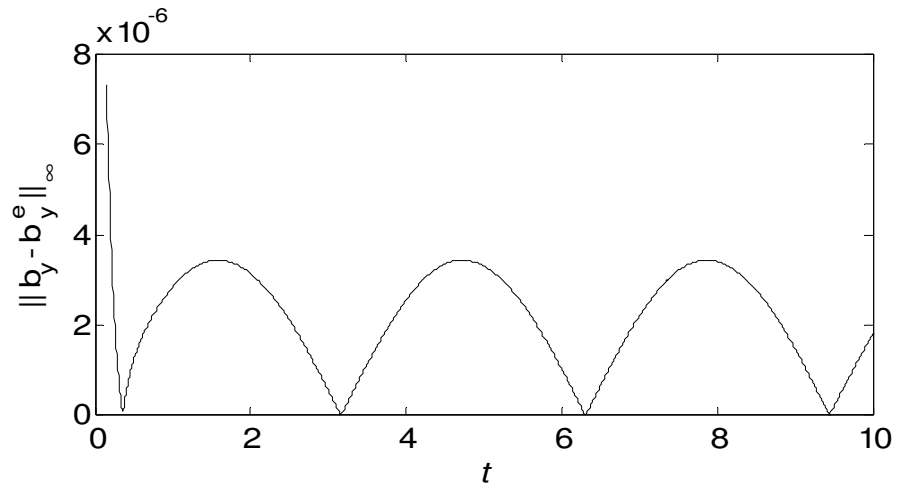


Figure 3.13 Infinite norm of error in  $\mathbf{b}_y$  vs.  $t$

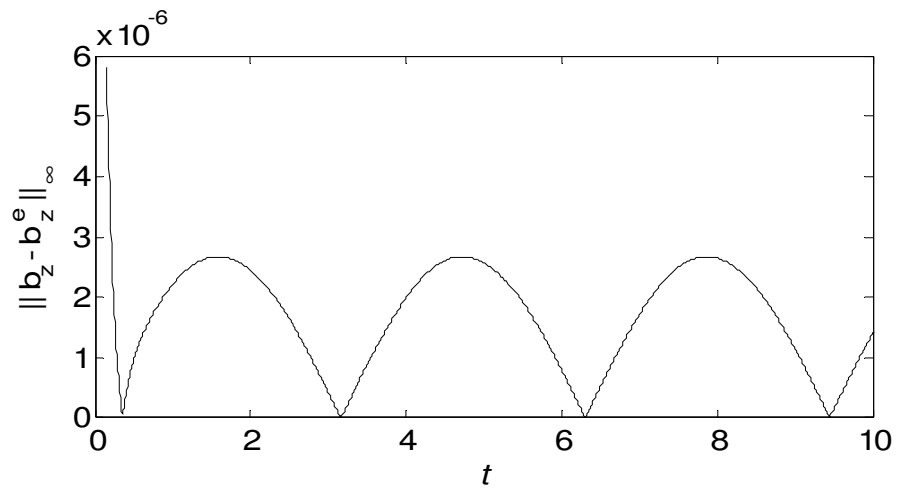


Figure 3.14 Infinite norm of error in  $\mathbf{b}_z$  vs.  $t$

## CHAPTER 4

### STRONG FORMULATION OF HYDRO-MAGNETIC EQUATION

In this chapter, an alternative technique is tried on the same problem. The continuity equation (2.80), the system of momentum equations (2.81)-(2.83) and the heat transport equation (2.84) are discretized using the earlier weak formulation, while the system of hydromagnetic equations (2.85)-(2.87) are discretized using a strong formulation. This is motivated by the fact that the induced magnetic field is in a quasi-steady relationship with the velocity field, in other words, magnetic field, in the present work, is completely linked to the velocity field in time. In fact, this relation is utilized implicitly in imposing the solenoid character of the velocity field on the induced magnetic field. Therefore, it is very convenient to compute the induced magnetic field node by node in the strong form, rather than handling it with Galerkin projection. The equations (2.85)-(2.87) are then treated in a point-wise manner at each time level and introduced into (2.81)-(2.83), explicitly. Even though the earlier weak formulation of the hydromagnetic relation generates positive definite, symmetric coefficient matrices, which are convenient to solve, as in the momentum and heat transport equations, in this chapter, the effects of using the strong form on the imposition of the solenoid character are investigated and analyzed.

The equations (2.85)-(2.87) are discretized for each wave number pair  $(k_x, k_y)$  using the expansions in terms of Hermite Legendre interpolants,  $\tilde{h}_j(z)$  (see Section 4.1), and Lagrange Legendre interpolants,  $h_j(z)$  (2.61). The resulting system of algebraic equations in terms of these expansions with summation over  $l$  and  $j$  is:

$$\left[\tilde{h}_l''(z_i) - k^2 \tilde{h}_l(z_i)\right] \hat{\mathbf{b}}_{x_l}^n = h_l(z_i) \hat{\mathbf{q}}_{x_l}^n, \quad (4.1)$$

$$\left[\tilde{h}_l''(z_i) - k^2 \tilde{h}_l(z_i)\right] \hat{\mathbf{b}}_{y_l}^n = h_l(z_i) \hat{\mathbf{q}}_{y_l}^n, \quad (4.2)$$

$$\left[h_j''(z_i) - k^2 h_j(z_i)\right] \hat{\mathbf{b}}_{z_j}^n = h_j(z_i) \hat{\mathbf{q}}_{z_j}^n \quad (4.3)$$

together with the boundary conditions (2.91):

$$\tilde{h}_l'(\pm 1) \hat{\mathbf{b}}_{x_l}^n = \tilde{h}_l'(\pm 1) \hat{\mathbf{b}}_{y_l}^n = h_j(\pm 1) \hat{\mathbf{b}}_{z_j}^n = 0 \quad (4.4)$$

where

$$\begin{bmatrix} \hat{\mathbf{b}}_x^n \\ \hat{\mathbf{b}}_y^n \end{bmatrix} = \begin{bmatrix} \hat{\mathbf{b}}_x \\ \hat{\mathbf{b}}_y \end{bmatrix} (m, n, z_l, n \Delta t) \cdot \tilde{h}_l(z) = \begin{bmatrix} \hat{\mathbf{b}}_{x_l} \\ \hat{\mathbf{b}}_{y_l} \end{bmatrix} \cdot \tilde{h}_l(z) \quad (4.5)$$

for the horizontal components and

$$\hat{\mathbf{b}}_z^n = \hat{\mathbf{b}}_z(m, n, z_j, n \Delta t) \cdot h_j(z) = \hat{\mathbf{b}}_{z_j} \cdot h_j(z) \quad (4.6)$$

for the vertical component of the induced magnetic field while the velocity field has the usual Lagrange Legendre expansion

$$\begin{bmatrix} \hat{\mathbf{q}}_x^n \\ \hat{\mathbf{q}}_y^n \end{bmatrix} = \begin{bmatrix} \hat{\mathbf{q}}_x \\ \hat{\mathbf{q}}_y \end{bmatrix} (m, n, z_l, n \Delta t) \cdot h_l(z) = \begin{bmatrix} \hat{\mathbf{q}}_{x_l} \\ \hat{\mathbf{q}}_{y_l} \end{bmatrix} \cdot h_l(z) \quad (4.7)$$

and

$$\hat{\mathbf{q}}_z^n = \hat{\mathbf{q}}_z(m, n, z_j, n \Delta t) \cdot h_j(z) = \hat{\mathbf{q}}_{z_j} \cdot h_j(z). \quad (4.8)$$

Equations from (4.1) to (4.3) can be rewritten in a more compact matrix form by the help of pseudo-spectral differentiation operators based on Hermite and Lagrange expansions:

$$\left[ \tilde{H}_{lp}^{(2)} - k^2 \tilde{H}_{lp}^{(0)} \right] \hat{\mathbf{b}}_{xl}^n = \tilde{H}_{lp}^{(0)} \hat{\mathbf{q}}_{xl}^n, \quad (4.9)$$

$$\left[ \tilde{H}_{lp}^{(2)} - k^2 \tilde{H}_{lp}^{(0)} \right] \hat{\mathbf{b}}_{yl}^n = \tilde{H}_{lp}^{(0)} \hat{\mathbf{q}}_{yl}^n, \quad (4.10)$$

$$\left[ H_{ji}^{(2)} - k^2 H_{ji}^{(0)} \right] \hat{\mathbf{b}}_{zj}^n = H_{ji}^{(0)} \hat{\mathbf{q}}_{zj}^n \quad (4.11)$$

for  $0 < i < N_z$ ,  $0 < j < N_z$  and  $0 \leq l \leq N_z$ ,  $0 \leq p \leq N_z$ .

#### 4.1 Construction of Hermite Cardinal Functions

Here, Neumann boundary conditions for the horizontal components of the induced magnetic field are embedded into the Hermite interpolants rather than adding them as additional constraints. The pseudo-spectral differentiation operators, constructed based on these Hermite interpolants enforce the boundary conditions automatically. In order to construct Hermite interpolants, (4.5) is rewritten by separating the terms corresponding to the boundary nodes and the interior nodes and adding terms corresponding to the specified derivative boundary conditions:

$$\begin{aligned} \begin{bmatrix} \hat{\mathbf{b}}_x \\ \hat{\mathbf{b}}_y \end{bmatrix} (z) = & \begin{bmatrix} \hat{\mathbf{b}}_x \\ \hat{\mathbf{b}}_y \end{bmatrix} (z_0) \cdot \tilde{h}_0(z) + \sum_{l=1}^{N_z-1} \begin{bmatrix} \hat{\mathbf{b}}_x \\ \hat{\mathbf{b}}_y \end{bmatrix} (z_l) \cdot \tilde{h}_l(z) + \begin{bmatrix} \hat{\mathbf{b}}_x \\ \hat{\mathbf{b}}_y \end{bmatrix} (z_{N_z}) \cdot \tilde{h}_{N_z}(z) \\ & + \frac{\partial}{\partial z} \begin{bmatrix} \hat{\mathbf{b}}_x \\ \hat{\mathbf{b}}_y \end{bmatrix} (z_0) \cdot \tilde{h}_0(z) + \frac{\partial}{\partial z} \begin{bmatrix} \hat{\mathbf{b}}_x \\ \hat{\mathbf{b}}_y \end{bmatrix} (z_{N_z}) \cdot \tilde{h}_{N_z}(z), \end{aligned} \quad (4.12)$$

such that

$$\begin{aligned} \hat{\mathbf{b}}_x(z_0) = \hat{\mathbf{b}}_{x0}, \hat{\mathbf{b}}_y(z_0) = \hat{\mathbf{b}}_{y0} \Rightarrow \\ \tilde{h}_0(z_0) = 1, \tilde{h}_j(z_0) = \tilde{h}_{N_z}(z_0) = \tilde{h}_0(z_0) = \tilde{h}_{N_z}(z_0) = 0, \end{aligned} \quad (4.13)$$

$$\begin{aligned}\hat{\mathbf{b}}_x(z_j) &= \hat{\mathbf{b}}_{x_j}, \hat{\mathbf{b}}_y(z_j) = \hat{\mathbf{b}}_{y_j} \Rightarrow \\ \tilde{h}_j(z_j) &= 1, \tilde{h}_0(z_j) = \tilde{h}_{N_z}(z_j) = \tilde{h}_0(z_j) = \tilde{h}_{N_z}(z_j) = 0, \end{aligned} \quad (4.14)$$

$$\begin{aligned}\hat{\mathbf{b}}_x(z_{N_z}) &= \hat{\mathbf{b}}_{x_{N_z}}, \hat{\mathbf{b}}_y(z_{N_z}) = \hat{\mathbf{b}}_{y_{N_z}} \Rightarrow \\ \tilde{h}_{N_z}(z_{N_z}) &= 1, \tilde{h}_0(z_{N_z}) = \tilde{h}_j(z_{N_z}) = \tilde{h}_0(z_{N_z}) = \tilde{h}_{N_z}(z_{N_z}) = 0, \end{aligned} \quad (4.15)$$

$$\begin{aligned}\frac{\partial}{\partial z} \hat{\mathbf{b}}_x(z_0) &= \hat{\mathbf{b}}'_{x_0} = 0, \frac{\partial}{\partial z} \hat{\mathbf{b}}_y(z_0) = \hat{\mathbf{b}}'_{y_0} = 0 \Rightarrow \\ \tilde{h}'_0(z_0) &= 1, \tilde{h}'_0(z_0) = \tilde{h}'_j(z_0) = \tilde{h}'_{N_z}(z_0) = \tilde{h}'_{N_z}(z_0) = 0, \end{aligned} \quad (4.16)$$

$$\begin{aligned}\frac{\partial}{\partial z} \hat{\mathbf{b}}_x(z_{N_z}) &= \hat{\mathbf{b}}'_{x_{N_z}} = 0, \frac{\partial}{\partial z} \hat{\mathbf{b}}_y(z_{N_z}) = \hat{\mathbf{b}}'_{y_{N_z}} = 0 \Rightarrow \\ \tilde{h}'_{N_z}(z_{N_z}) &= 1, \tilde{h}'_0(z_{N_z}) = \tilde{h}'_j(z_{N_z}) = \tilde{h}'_{N_z}(z_{N_z}) = \tilde{h}'_0(z_{N_z}) = 0, \end{aligned} \quad (4.17)$$

Here,  $j$  refers to interior grids and  $0 < j < N_z$ . Construction of polynomial functions,  $\tilde{h}_0(z), \tilde{h}_j(z), \tilde{h}_{N_z}(z)$  is as follows:

$\tilde{h}_j(z)$  is to be a unique polynomial with a double zero at  $z_0$  and at  $z_{N_z}$  with  $\tilde{h}_j(z_j) = 1$ :

$$\tilde{h}_j(z) = \frac{(z - z_0)^2 (z - z_{N_z})^2}{(z_j - z_0)^2 (z_j - z_{N_z})^2} = \frac{(z - z_0)(z - z_{N_z})}{(z_j - z_0)(z_j - z_{N_z})} h_j(z) \quad (4.18)$$

or

$$\tilde{h}_j(z) = \frac{(z^2 - 1)}{(z_j^2 - 1)} h_j(z) \quad (4.19)$$

and

$$\tilde{h}'_j(z) = \frac{2z}{(z_j^2 - 1)} h_j(z) + \frac{(z^2 - 1)}{(z_j^2 - 1)} h'_j(z), \quad (4.20)$$

$$\tilde{h}_j''(z) = \frac{2}{(z_j^2 - 1)} h_j(z) + \frac{4z}{(z_j^2 - 1)} h_j'(z) + \frac{(z^2 - 1)}{(z_j^2 - 1)} h_j''(z). \quad (4.21)$$

$\tilde{h}_0(z)$  is to be a unique polynomial with a single zero at  $z_j$  and a double zero at  $z_{N_z}$  with  $\tilde{h}_0(z_0)=1$  and  $\tilde{h}_0'(z_0)=0$ :

$$\tilde{h}_0(z) = (c_1 z + c_2) \frac{(z - z_j)(z - z_{N_z})^2}{(z_0 - z_j)(z_0 - z_{N_z})^2} = (c_1 z + c_2) \frac{(z - z_{N_z})}{(z_0 - z_{N_z})} h_0(z), \quad (4.22)$$

$$\tilde{h}_0(z_0) = 1 \Rightarrow c_2 = 1 - c_1 z_0, \quad (4.23)$$

$$\tilde{h}_0'(z_0) = 0 \Rightarrow c_1 = -\frac{1}{z_0 - z_{N_z}} - h_0'(z_0), \quad (4.24)$$

$$\tilde{h}_0(z) = \left[ (z - z_0) \left( \frac{-1}{z_0 - z_{N_z}} - h_0'(z_0) \right) + 1 \right] \frac{(z - z_{N_z})}{(z_0 - z_{N_z})} h_0(z) \quad (4.25)$$

or

$$\tilde{h}_0(z) = \left[ (1 + z) \left( \frac{1}{2} - h_0'(-1) \right) + 1 \right] \frac{1 - z}{2} h_0(z) \quad (4.26)$$

and

$$\begin{aligned} \tilde{h}_0'(z) = & \left( \frac{-z}{2} + z h_0'(-1) + 1 \right) h_0(z) \\ & + \left[ (1 + z) \left( \frac{1}{2} - h_0'(-1) \right) + 1 \right] \frac{1 - z}{2} h_0'(z), \end{aligned} \quad (4.27)$$

$$\begin{aligned} \tilde{h}_0''(z) = & -\left( \frac{1}{2} - h_0'(-1) \right) h_0(z) - \left[ 2z \left( \frac{1}{2} - h_0'(-1) \right) + 1 \right] h_0'(z) \\ & + \left[ (1 + z) \left( \frac{1}{2} - h_0'(-1) \right) + 1 \right] \frac{1 - z}{2} h_0''(z). \end{aligned} \quad (4.28)$$

$\tilde{h}_{N_z}(z)$  is to be a unique polynomial with a single zero at  $z_j$  and a double zero at  $z_0$  with  $\tilde{h}_{N_z}(z_{N_z})=1$  and  $\tilde{h}_{N_z}'(z_{N_z})=0$ :

$$\tilde{h}_{N_z}(z) = (c_3 z + c_4) \frac{(z - z_j)(z - z_0)^2}{(z_{N_z} - z_j)(z_{N_z} - z_0)^2} \quad (4.29)$$

or

$$\tilde{h}_{N_z}(z) = (c_3 z + c_4) \frac{(z - z_0)}{(z_{N_z} - z_0)} h_{N_z}(z) , \quad (4.30)$$

$$\tilde{h}_{N_z}(z_{N_z}) = 1 \Rightarrow c_4 = 1 - c_3 z_{N_z} , \quad (4.31)$$

$$\tilde{h}'_{N_z}(z_{N_z}) = 0 \Rightarrow c_3 = -\frac{1}{z_{N_z} - z_0} - \tilde{h}'_{N_z}(z_{N_z}) , \quad (4.32)$$

$$\tilde{h}_{N_z}(z) = \left[ (z - z_{N_z}) \left( \frac{-1}{z_{N_z} - z_0} - h'_{N_z}(z_{N_z}) \right) + 1 \right] \frac{(z - z_0)}{(z_{N_z} - z_0)} h_{N_z}(z) \quad (4.33)$$

or

$$\tilde{h}_{N_z}(z) = \left[ (1 - z) \left( \frac{1}{2} + h'_{N_z}(1) \right) + 1 \right] \frac{1+z}{2} h_{N_z}(z) , \quad (4.34)$$

and

$$\begin{aligned} \tilde{h}'_{N_z}(z) &= \left( \frac{-z}{2} - z h'_{N_z}(1) + 1 \right) h_{N_z}(z) \\ &\quad + \left[ (1 - z) \left( \frac{1}{2} + h'_{N_z}(1) \right) + 1 \right] \frac{1+z}{2} h'_{N_z}(z) , \end{aligned} \quad (4.35)$$

$$\begin{aligned} \tilde{h}''_{N_z}(z) &= -\left( \frac{1}{2} + h'_{N_z}(1) \right) h_{N_z}(z) - \left( 2z \left( \frac{1}{2} + h'_{N_z}(1) \right) - 1 \right) h'_{N_z}(z) \\ &\quad + \left[ (1 - z) \left( \frac{1}{2} + h'_{N_z}(1) \right) + 1 \right] \frac{1+z}{2} h''_{N_z}(z) . \end{aligned} \quad (4.36)$$

$\tilde{h}_0(z)$  and  $\tilde{h}_{N_z}(z)$  have vanishing coefficients in (4.12) so that there is no need to derive them. Pseudo-spectral differentiation matrices are constructed by using the derivatives of the polynomials derived above.

The Lagrange interpolation condition yields the zeroth order operator such that:

$$\tilde{H}_{pl}^{(0)} = \tilde{h}_l(z_p) = \delta_{lp} . \quad (4.37)$$

First order spectral operator is constructed using the equations (4.20), (4.27) and (4.35):

$$\tilde{H}_{pl}^{(1)} = \tilde{h}_l'(z_p). \quad (4.38)$$

And the second order spectral operator is defined by using the equations (4.21), (4.28) and (4.36):

$$\tilde{H}_{pl}^{(2)} = \tilde{h}_l''(z_p) \quad (4.39)$$

for  $0 \leq l \leq N_z$  and  $0 \leq p \leq N_z$ .

Differentiation operators (4.37) and (4.39) are substituted into (4.9) and (4.10).

By using rescaled versions of Legendre-Lagrange interpolants (2.52) and their first derivatives with respect to  $z$  (3.17), the usual Legendre-Lagrange interpolants:

$$h_i(z) = \bar{h}_i(z) \sqrt{w_i} \quad (4.40)$$

and their first derivatives:

$$h_i'(z) = \bar{h}_i'(z) \sqrt{w_i} \quad (4.41)$$

can be obtained by multiplying the rescaled functions with square root of the weights.

By using (4.40) and (4.41), the pseudo-spectral differentiation operators can be defined on quadrature nodes in a discretized form:

$$H_{ji}^{(0)} = h_i(z_j), \quad (4.42)$$

$$H_{ji}^{(1)} = h_i'(z_j) \quad (4.43)$$

and, second order pseudo-spectral differentiation operator can be computed by matrix multiplication:

$$H^{(2)} = H^{(1)} H^{(1)} \quad (4.44)$$

for  $0 < i < N_z$  and  $0 < j < N_z$

Discretized equations (4.9), (4.10) and (4.11) are rewritten as:

$$\left[ \tilde{H}^{(2)} - k^2 I \right] \hat{\mathbf{b}}_x^n = \hat{\mathbf{q}}_x^n, \quad (4.45)$$

$$\left[ \tilde{H}^{(2)} - k^2 I \right] \hat{\mathbf{b}}_y^n = \hat{\mathbf{q}}_y^n, \quad (4.46)$$

$$\left[ H^{(2)} - k^2 I \right] \hat{\mathbf{b}}_z^n = \hat{\mathbf{q}}_z^n \quad (4.47)$$

in the light of the derivations above.

## 4.2 Inverse of Differentiation Operators

Before substituting into the momentum equations, the discretized equations (4.45), (4.46) and (4.47) are solved for the induced magnetic field values at time level  $n$ .

$$\hat{\mathbf{b}}^n = H_{\mathbf{B}}^{-1} \hat{\mathbf{q}}^n, \quad (4.48)$$

where

$$H_{\mathbf{B}} = \begin{cases} \tilde{H}^{(2)} - k^2 I \\ H^{(2)} - k^2 I \end{cases} \quad \text{if solving for } \begin{matrix} \hat{\mathbf{b}}_x \text{ or } \hat{\mathbf{b}}_y \\ \hat{\mathbf{b}}_z \end{matrix}, \quad (4.49)$$

The inverses can be computed using the technique of collocation diagonalization, as explained in the previous chapter:

$$\tilde{H}^{(2)} = \tilde{E} \tilde{G} \tilde{E}^{-1}, \quad (4.50)$$

$$H^{(2)} = E G E^{-1}. \quad (4.51)$$

Here,  $\tilde{G}$  and  $G$  are matrices whose diagonal elements are the eigenvalues of  $\tilde{H}^{(2)}$  and  $H^{(2)}$ ,  $\tilde{E}$  and  $E$  contain the corresponding eigenvectors as their columns.

Substitution of (4.50) and (4.51) into (4.49) will give:

$$H_{\mathbf{B}} = \begin{cases} \tilde{E} \tilde{G} \tilde{E}^{-1} - k^2 I \\ E G E^{-1} - k^2 I \end{cases} \quad \text{if solving for } \begin{matrix} \hat{\mathbf{b}}_x \text{ or } \hat{\mathbf{b}}_y \\ \hat{\mathbf{b}}_z \end{matrix}, \quad (4.52)$$

Similar to the derivation in section 3.1, the inverses of the differentiation operators are written in the form:

$$\mathbf{H}_B^{-1} = \begin{cases} \tilde{E} [\tilde{G} - k^2 I]^{-1} \tilde{E}^{-1} \\ E [G - k^2 I]^{-1} E^{-1} \end{cases} \quad \text{if solving for } \begin{matrix} \hat{\mathbf{b}}_x \text{ or } \hat{\mathbf{b}}_y, \\ \hat{\mathbf{b}}_z. \end{matrix} \quad (4.53)$$

Before the numerical integration in time starts,  $\tilde{H}^{(2)}$ ,  $H^{(2)}$  and their eigen components  $\tilde{G}$ ,  $G$ ,  $\tilde{E}$  and  $E$  are evaluated. By using the technique of collocation diagonalization,  $\mathbf{H}_B^{-1}$  is obtained by simply inverting a diagonal matrix,  $[\tilde{G} - k^2 I]$  or  $[G - k^2 I]$  as follows:

$$\mathbf{H}_{Bij}^{-1} = \begin{cases} \sum_p \tilde{E}_{ip} \frac{1}{\tilde{G}_{pp} - k^2} (\tilde{E}^{-1})_{pj} \\ \sum_p E_{ip} \frac{1}{G_{pp} - k^2} (E^{-1})_{pj} \end{cases} \quad \text{if solving for } \begin{matrix} \hat{\mathbf{b}}_x \text{ or } \hat{\mathbf{b}}_y, \\ \hat{\mathbf{b}}_z. \end{matrix} \quad (4.54)$$

Similar to the indeterminacy at  $k_x = k_y = 0$  mode in the solution for the horizontal components of hydromagnetic equation in the weak formulation (3.35) and (3.36), there stands a singularity for  $\tilde{H}^{(2)}$  (4.50) at zero mode, infact  $\tilde{G}$  has a zero eigenvalue. Therefore at  $k_x = k_y = 0$ , the inverse (4.54) does not exist.

Similar to the row and column modifications in the weak case, hydromagnetic equation is modified for  $k_x = k_y = 0$ , such that:

$$\mathbf{H}_{Bij} = \begin{cases} 0 & i \neq j = N_z/2 \\ 0 & j \neq i = N_z/2 \\ 1 & i = j = N_z/2 \\ \tilde{H}_{ij}^{(2)} & i \neq N_z/2 \text{ and } j \neq N_z/2 \end{cases} \quad \text{if } \quad \text{for } t > 0 \quad (4.55)$$

and

$$\hat{\mathbf{q}}_{xi} = \begin{cases} 0 & \text{if } i = N_z/2 \\ \hat{\mathbf{q}}_{xi} & \text{if } i \neq N_z/2 \end{cases} \quad \text{for } t > 0, \quad (4.56)$$

$$\hat{\mathbf{q}}_{y_i} = \begin{cases} 0 & \text{if } i = N_z/2 \\ \hat{\mathbf{q}}_{y_i} & \text{if } i \neq N_z/2 \end{cases} \quad \text{for } t > 0. \quad (4.57)$$

There is no substantial difference between the solution algorithm of the strong formulation and that of the weak formulation except for the pseudo-spectral differential operators for the system of hydromagnetic equations. A flow chart is given including both solution paths in Figure 4.1.

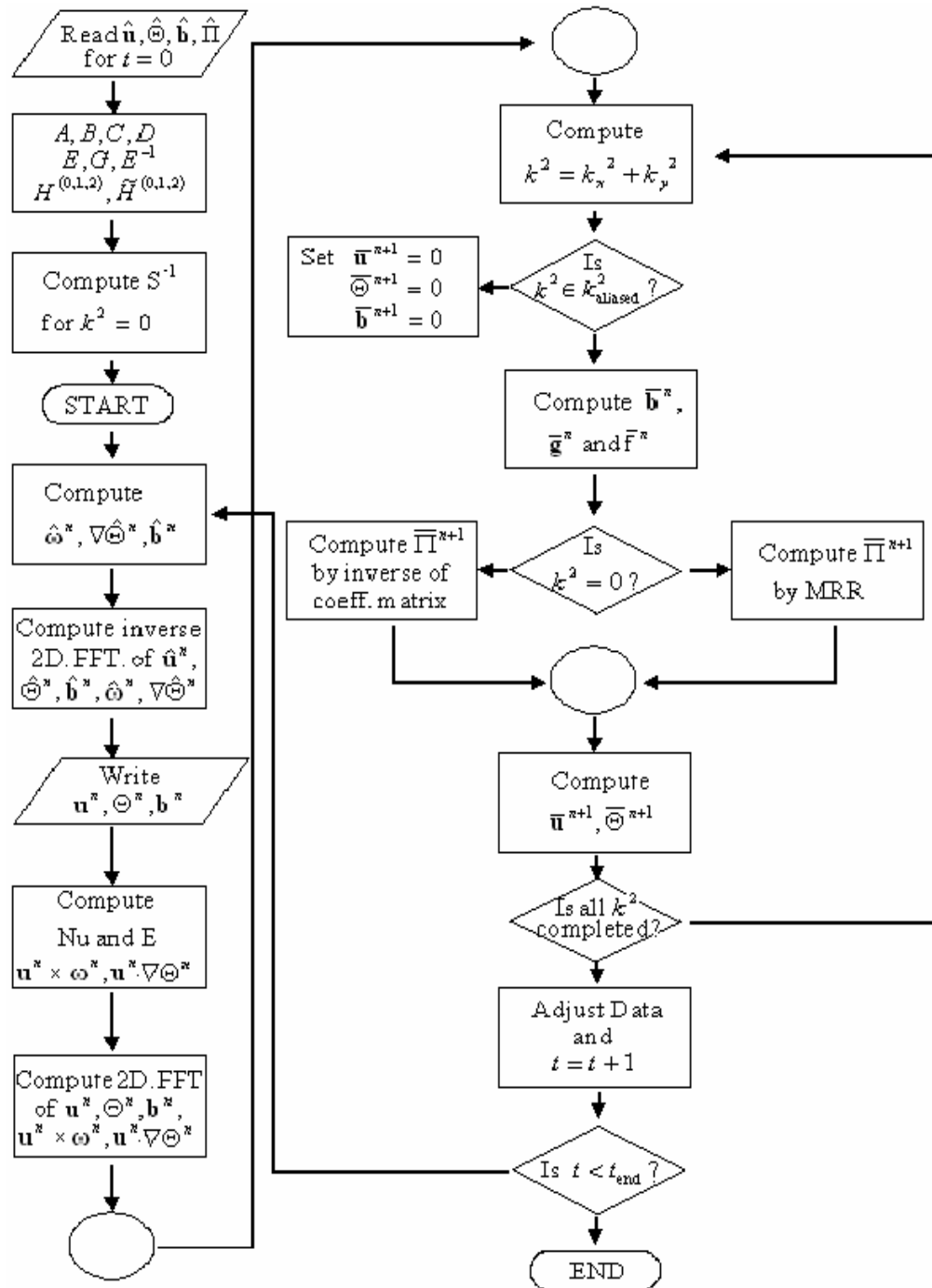


Figure 4.1 Code Flowchart

### 4.3 Test Studies

The apriori selected functions in section 3.4 are used here again as velocity, temperature and induced magnetic solution fields by adding suitable forcing terms to the model equations at the same parameter values:

$$\text{Ra}^* = \text{Pr} = 1, \text{Q}^* = \sqrt{3}, L_x = L_y = 2\pi, N_x = N_y = 16, N_z = 8, \Delta t = 0.005.$$

Similar to the weak case, right hand side of the momentum and the hydromagnetic equations are rewritten for an external magnetic field applied diagonally within the convective box. Lorentz term in (3.86) and right hand side of hydromagnetic equation (3.87) do not change.

Table 4.1 gives the infinite norm of absolute errors for the velocity, the temperature, and the induced magnetic fields. Furthermore, divergence of the velocity and the induced magnetic fields as well as derivative values of the horizontal components of the induced magnetic field at the boundaries in the cases of the weak formulation, as explained in Chapter 3, and the strong formulation are compared. In using Hermite interpolants in the strong formulation, no significant improvement over the weak formulation in the accuracy of the results is observed.

In the figures below, absolute values of Fourier coefficients of variables are shown at  $z_3 \cong -0.677$  and  $t = 5$ . As expected, the only non-trivial mode is at the wave index pair  $m = n = 1$ .

Finally, the plots of errors versus time stepping in logarithmic scale show that the error increases approximately in  $O(\Delta t^2)$  as a result of the second order time integrators.

Table 4.1 Maximum values of error for the test cases.

	<b>WEAK</b>	<b>HERMITE</b>
$\  \mathbf{u}_x - \mathbf{u}_x^e \ _\infty$	0.8729E-05	0.8731E-05
$\  \mathbf{u}_y - \mathbf{u}_y^e \ _\infty$	0.8729E-05	0.8731E-05
$\  \mathbf{u}_z - \mathbf{u}_z^e \ _\infty$	0.1195E-04	0.1195E-04
$\  \Theta - \Theta^e \ _\infty$	0.1312E-04	0.1312E-04
$\  \mathbf{b}_x - \mathbf{b}_x^e \ _\infty$	0.3433E-05	0.3433E-05
$\  \mathbf{b}_y - \mathbf{b}_y^e \ _\infty$	0.3433E-05	0.3433E-05
$\  \mathbf{b}_z - \mathbf{b}_z^e \ _\infty$	0.2673E-05	0.2673E-05
$\  \nabla \cdot \mathbf{u} \ _\infty$	0.1630E-05	0.1633E-05
$\  \nabla \cdot \mathbf{b} \ _\infty$	0.1512E-04	0.1514E-04
$\  (\partial \mathbf{b}_x / \partial z)_{z=-1} \ _\infty$	0.4552E-05	0.3653E-05
$\  (\partial \mathbf{b}_y / \partial z)_{z=-1} \ _\infty$	0.4552E-05	0.3653E-05
$\  (\partial \mathbf{b}_x / \partial z)_{z=+1} \ _\infty$	0.4552E-05	0.3653E-05
$\  (\partial \mathbf{b}_y / \partial z)_{z=+1} \ _\infty$	0.4552E-05	0.3653E-05

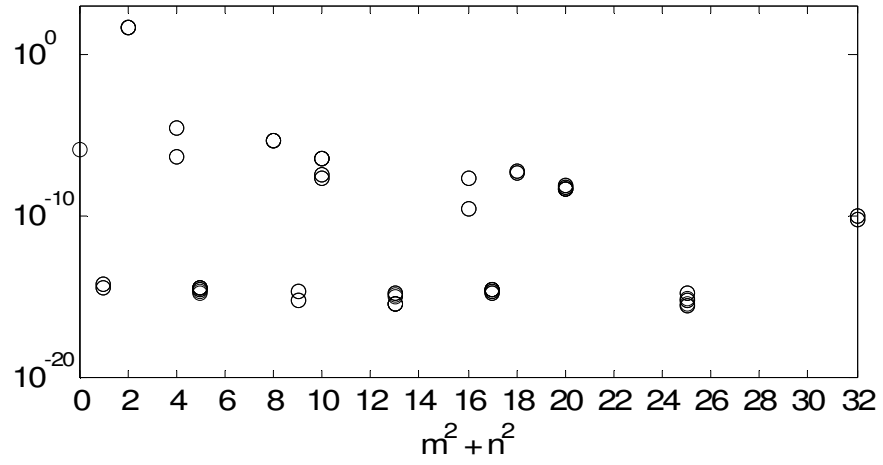


Figure 4.2  $|\bar{\mathbf{u}}_x|$  at  $z_3 = -0.677, t = 5$

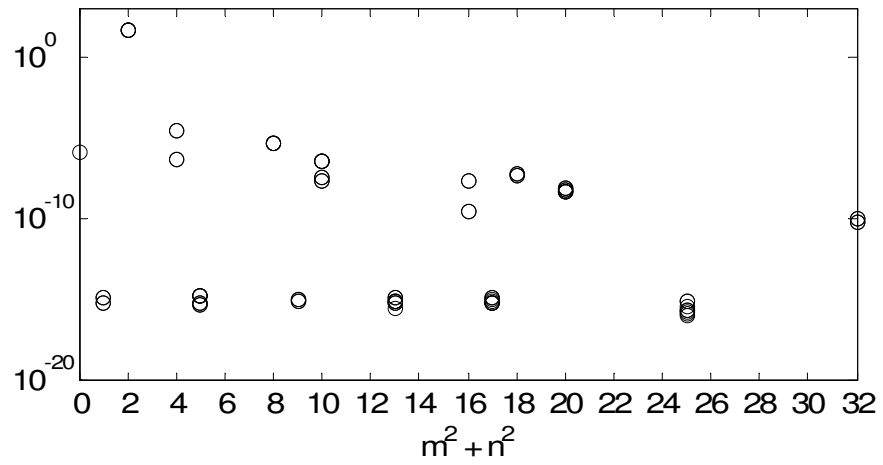


Figure 4.3  $|\bar{\mathbf{u}}_y|$  at  $z_3 = -0.677, t = 5$

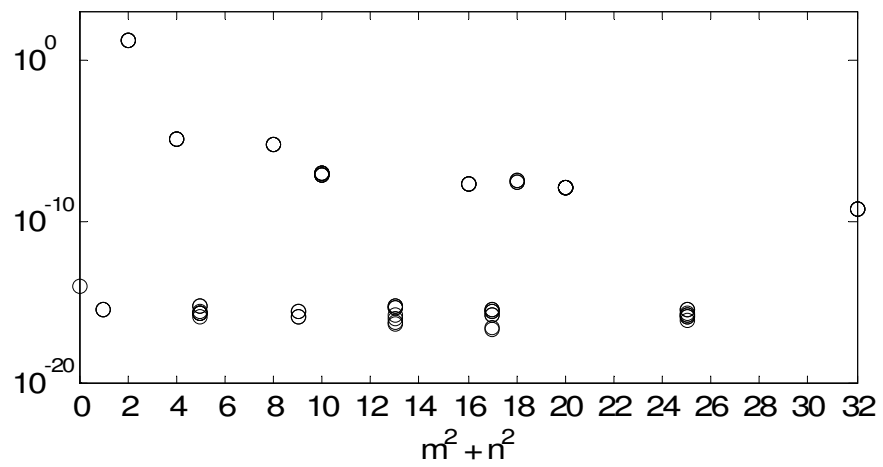


Figure 4.4  $|\bar{\mathbf{u}}_z|$  at  $z_3 = -0.677, t = 5$

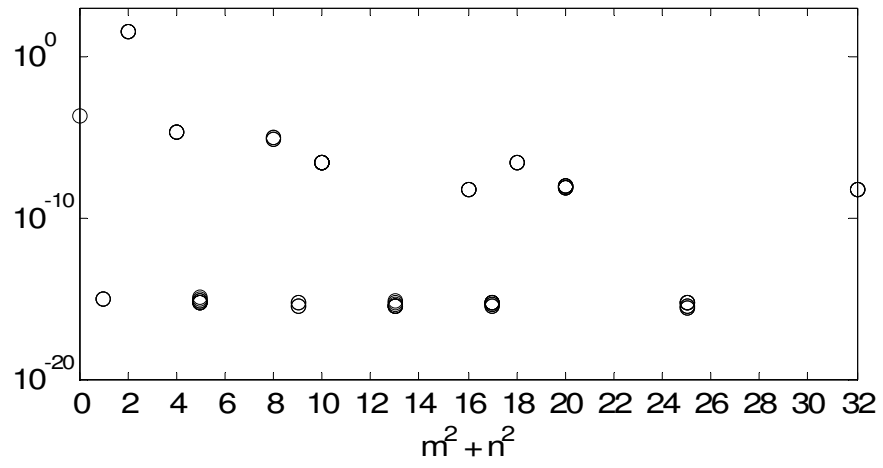


Figure 4.5  $|\Theta|$  at  $z_3 = -0.677, t = 5$

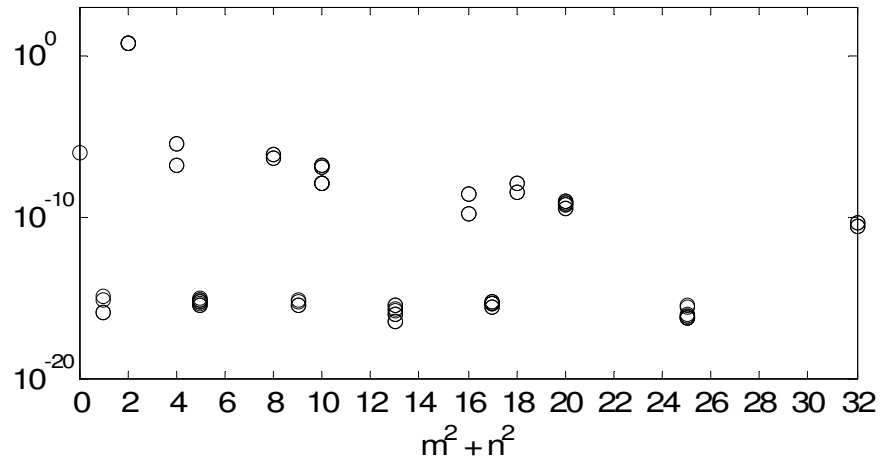


Figure 4.6  $|\bar{b}_x|$  at  $z_3 = -0.677, t = 5$

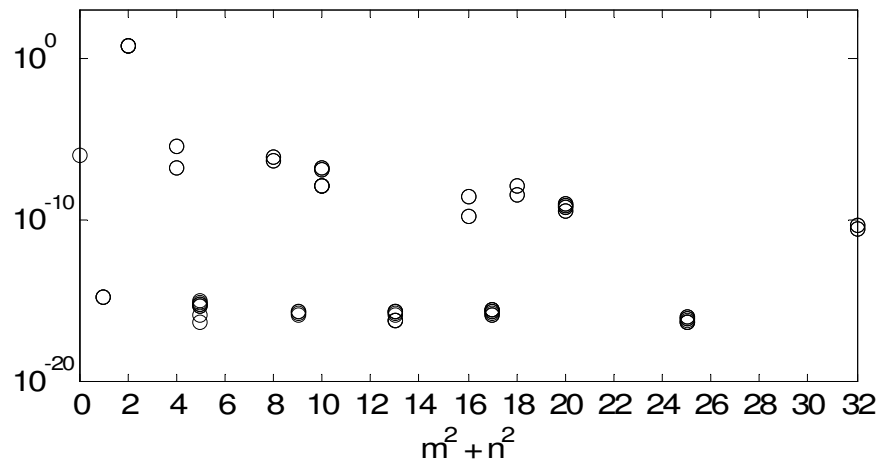


Figure 4.7  $|\bar{b}_y|$  at  $z_3 = -0.677, t = 5$

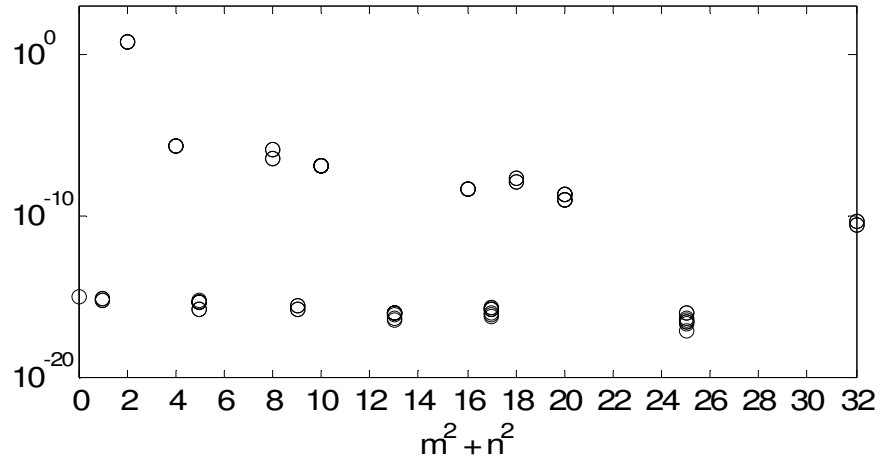


Figure 4.8  $|\bar{b}_z|$  at  $z_3 = -0.677, t = 5$

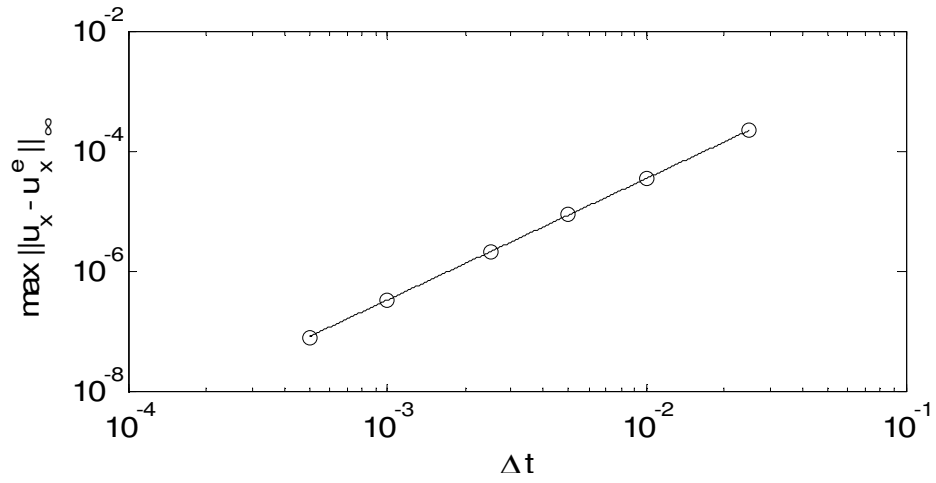


Figure 4.9 Maximum value of  $\|\mathbf{u}_x - \mathbf{u}_x^e\|_\infty$  vs.  $\Delta t$

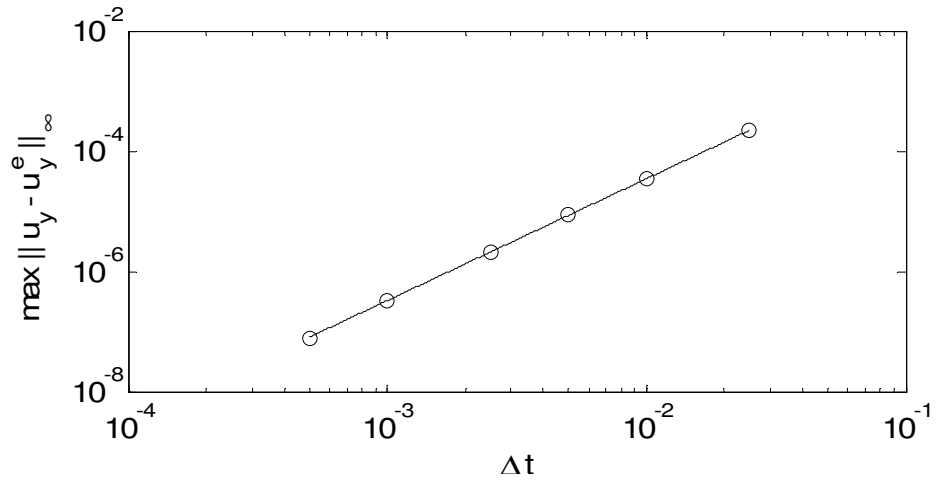


Figure 4.10 Maximum value of  $\|\mathbf{u}_y - \mathbf{u}_y^e\|_\infty$  vs.  $\Delta t$

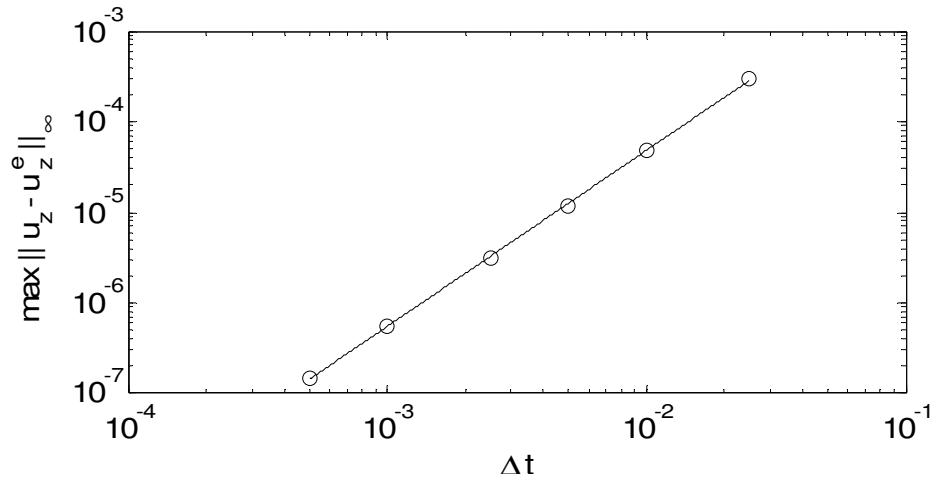


Figure 4.11 Maximum value of  $\|u_z - u_z^e\|_\infty$  vs.  $\Delta t$

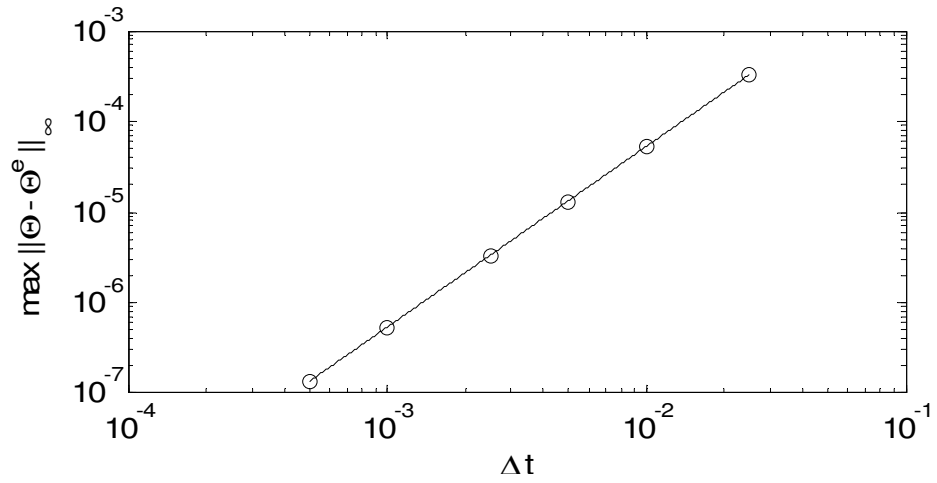


Figure 4.12 Maximum value of  $\|\Theta_x - \Theta_x^e\|_\infty$  vs.  $\Delta t$

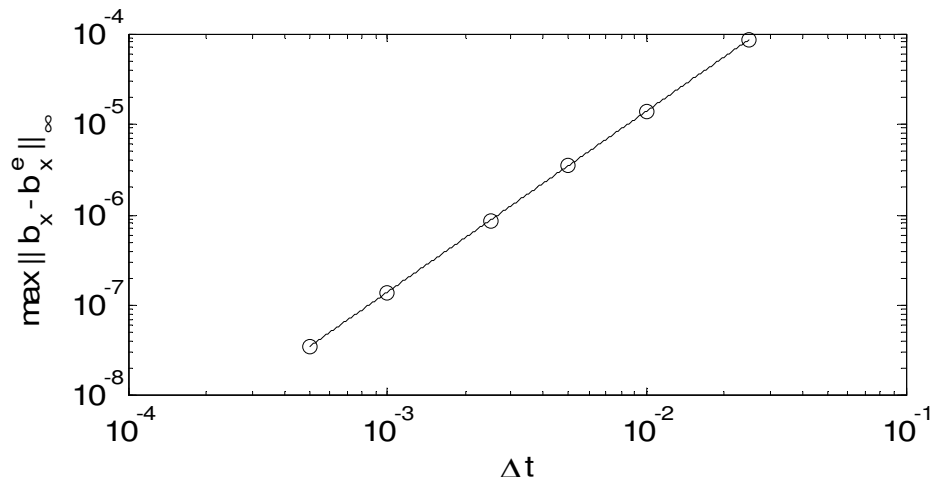


Figure 4.13 Maximum value of  $\|b_x - b_x^e\|_\infty$  vs.  $\Delta t$

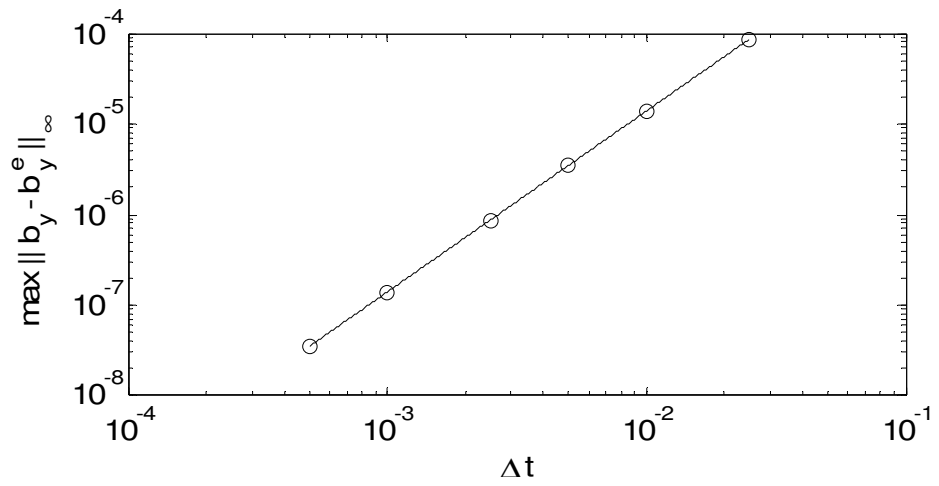


Figure 4.14 Maximum value of  $\|b_y - b_y^e\|_\infty$  vs.  $\Delta t$

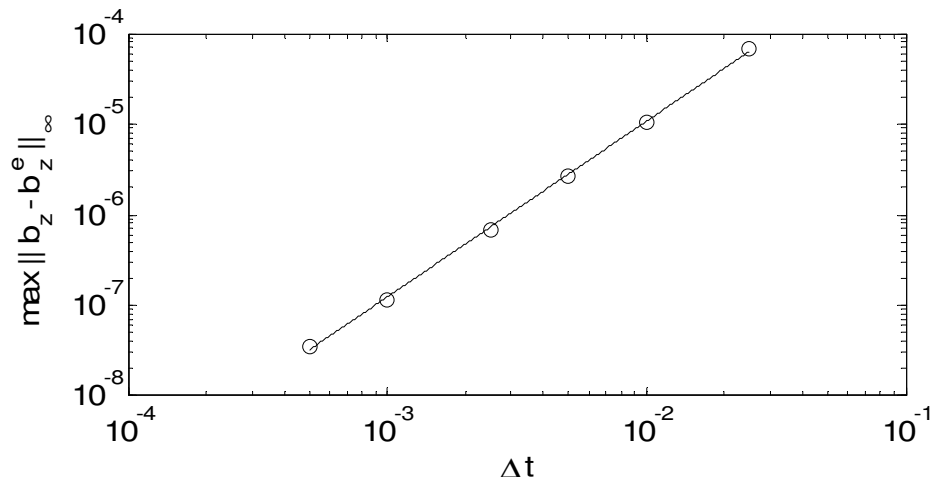


Figure 4.15 Maximum value of  $\|b_z - b_z^e\|_\infty$  vs.  $\Delta t$

## CHAPTER 5

### NUMERICAL CODE VALIDATION IN REAL CASES

In this session, a number of simulations are performed in supercritical regime. In the first section, the delay of onset of time independent instability is focused on by taking the interaction of convection with the magnetic field in the vertical direction  $z$ . In the second section, the interaction with an oblique magnetic field in the  $yz$  plane, that is, one having a horizontal component in the  $y$  direction, is investigated. The resulting oscillations and the flow patterns are discussed while comparing them with similar simulations and experiment results.

Average kinetic energy in all directions and average Nusselt number are monitored during time integration; average kinetic energy is computed by integration of inner product of the average velocity along  $z$ , that is:

$$\mathbf{E} = \frac{1}{8} \int_{-1}^{+1} \langle \mathbf{u} \rangle^2 dz . \quad (5.1)$$

Nusselt number indicates the increased efficiency of the average heat transfer between top and bottom plates due to convection in comparison to pure conduction:

$$\text{Nu} = 1 + 2 \left| \left( \frac{\partial \Theta}{\partial z} \right)_{\text{wall}} \right| . \quad (5.2)$$

Random perturbations over the conduction temperature profile are taken as initial conditions for temperature while

all the other variables are set to zero. The numerical integration in time is continued until a statistically steady regime is reached at which point data collection starts. In order to locate data collection point, for example, for a steady 2-D roll motion regime, convergence is interpreted to be reached at a level of kinetic energy in the direction of no-motion, where here it is the  $y$  direction with a level satisfying  $E_y \leq 10^{-8}$ . Each run uses the end of the previous run as initial condition.

$N_x = N_y = N_z = 16$  grid is used for simulations. Steady roll, periodic and even doubly periodic motions can be well resolved by 16 nodes in the horizontal directions. Moreover, in these simulations, models have small aspect ratios so that the spatial resolution by 16 nodes is well enough as indicated by Nu values for a number of horizontal grids in Table 5.1. Results in this table are generated at  $Ra = 50000$  and  $Q = 900$  with an aspect ratio  $\Gamma = 3:3$ . Nu for 12 and 16 nodes in the vertical differs about 10% but for 16 and 20 nodes there is hardly any change in Nu value.

In the first section, size of the convective box in the  $y$  direction is half of that is used in this test ( $\Gamma = 3:1.5$ ), while in the second section the analysis are performed in a box with an aspect ratio  $\Gamma = 1.95:1.90$  where the wavelengths of steady rolls are longer than those resulted in this mesh refinement test. Therefore mesh resolution in horizontal direction is satisfactory. Even at the regime with roll pattern in which four rolls exists in one direction of the box and with high  $Ra$ ,

i.e.  $Ra = 50000$ , using at least 16 nodes in horizontal directions provides a quite fine spatial resolution.

Table 2 Grid refinement,  $Ra = 50000$ ,  $Pr = 0.05$  and  $Q = 900$ .

	$N_x = N_y = 12$	$N_x = N_y = 16$	$N_x = N_y = 20$
$Nu$	2.7135	2.4321	2.4321

$N_z = 16$  implies that there are 17 nodes in the  $z$  direction including boundaries. Interpolation by Legendre polynomials provides denser nodal configuration near the  $z$  boundaries, thus help resolving boundary layers.  $N_z = 16$  is observed to be good enough to investigate the cases where  $Nu \leq 2.7$ . Infact, there should be at least three nodes in the thermal layer,  $\delta_\theta$  for the stability; where  $\delta_\theta$  is defined by a relation based on heat transfer rate as given in [27]:

$$\delta_\theta = \frac{1}{2 Nu}. \quad (5.3)$$

At least 16 nodes in the  $z$  direction place three nodes in the thermal layer for  $Nu \leq 2.7$ .

Typical dimensionless time step is selected in the range of  $5 \cdot 10^{-4} \leq \Delta t \leq 5 \cdot 10^{-3}$ . In any case,  $\Delta t = 5 \cdot 10^{-3}$  is tried first and if this minimum time stepping is not enough for the temporal stability, then time step is halved. This procedure is repeated until temporal stability is reached. In the first section, steady rolls for each  $(Ra, Q)$  parameter pairs are computed with  $\Delta t = 5 \cdot 10^{-3}$  but in the time dependent regime studied in the second section, time step is decreased until the temporal stability is reached. Here, total average kinetic energy is

used in place of the velocity parameter in the CFL number described in [28] in which the stability restrictions are for use in pure Rayleigh Benard convection. Based on our observations in this study, when total average kinetic energy gets greater than 30, especially in the oscillatory regime, the size of time stepping is to be selected carefully.

As a preliminary test, the code is used for a non-magnetic case. In this case  $Ra=2000$ ,  $Pr=0.71$ , and critical wave number  $\zeta=3.117$  are taken as the parameter values where the latter corresponds to an aspect ratio of  $\Gamma=2.02:2.02$  or the box dimensions of  $L_x = L_y = 4\pi/3.117$ . As a result of this run,  $Nu=1.211$  is found using a  $16 \times 16 \times 8$  grid and this compares satisfactorily with 1.212 in Clever and Busse [29].

## **5.1 Two Dimensional Stationary Flows**

In this subsection, a convective fluid (liquid metal) with a low Pr number  $Pr=0.05$  is chosen in a layer with aspect ratio  $\Gamma=3:1.5$ , and subjected to a vertical magnetic field. An analysis is performed to investigate the effects of a vertical magnetic field by studying the evolution of the convective flow under the magnetic field whose strength is gradually increased by increasing the non-dimensional Chandrasekhar number  $Q$ . Critical Chandrasekhar number,  $Q_c$  is defined as the value at which convective motions and in turn convective heat transfer starts with  $Nu > 1$ .

The first spatial pattern above  $Q_c$  is found to be a stationary system of two dimensional parallel rolls (Figure 5.1). Similar

to this velocity pattern, induced magnetic field extends in the  $y$  direction in a roll like manner (Figure 5.2). As stated in [12] and [15] that a vertical magnetic field acts towards suppression of the instabilities in this regime. In Figure 5.3, it is clear that increasing  $Q$  diminishes the energy of the motion, so  $Nu$  drops.

Sudden changes in flow pattern are observed for the cases  $Ra=30000$  at  $Q=1600$  and  $Ra=50000$  at  $Q=2750$  in the form of reorganization of flow caused by increase in number of rolls or decrease in wavelength,  $\zeta$  where it changes from  $\zeta=1.5$  to  $\zeta=1$ . Figure 5.4 shows the initial stage for  $Q=1100$  at  $t=0$ . By using this initial condition, if the magnetic field is increased to  $Q=1700$ , the kinetic energy of flows drops until around  $t=35$  (Figure 5.5), at which the rolls are reorganized until  $t=45$  (Figure 5.6 and Figure 5.7). The reorganization of the flow towards smaller horizontal scales is explained in [15] as an act towards minimizing Joule dissipation by reducing horizontal motions while increasing vertical motions since the zones of vertical motion lack Joule dissipation under vertical magnetic field. Indeed, this fact points out to the increased efficiency for heat transfer in the stationary regime while  $\zeta$  drops,  $Nu$  slightly increases.

In Table 5.2,  $Q_c$  corresponding to each  $Ra$  value is shown, computed by quadratic extrapolation of the available data just above  $Nu=1$ . They are in good agreement with the critical values which are obtained by interpolation on Table XV in [1].  $\zeta_c$  corresponding to each  $Q_c$  value is also available in this table. Extrapolated  $Q_c$  values are shown to differ

somewhat in Table 5.2 in comparison to the computed values. This may be caused by the discrepancy in the critical wavelength  $\zeta_c$  due to the restrictions in the computation imposed by the fixed aspect ratio of the convective box.

Table 5.2-  $Q_c$  ( $Nu=1$ ) for  $Ra=10000$ ,  $Ra=30000$  and  $Ra=50000$ .

<b>Ra</b>	<b><u>Present work</u></b>		<b><u>Chandrasekhar [1]</u></b>	
	$Q_c$	$\zeta$	$Q_c$	$\zeta_c$
10000	464	1.5	493	2.44
30000	1987	1.0	1990	1.92
50000	3551	1.0	3612	1.71

To demonstrate further confirmation, some test results are compared with the study of R. Mößner [20] in which aspect ratio is chosen as  $\Gamma=6:3$ , which is two times larger in  $x$  and  $y$ . Some  $Nu$  values from Figure 5.3 and the corresponding  $\zeta$  are shown in Table 5.3.  $\zeta$  is slightly larger in this work due to sidewall boundaries present in [20] in the horizontal directions which locally prevent roll action by friction or viscous damping. Additionally, in Mößner's study, the upper and lower plates are electrically insulated so that electric currents can not pass through boundaries and form a loop inside the region. Consequently, short circuit of electric currents near these surfaces, called Hartmann layers, ends up with a huge Lorentz resistance and by means of that intensity of heat transfer drops. This fact can be seen from  $Nu$  values in Table 5.3,  $Nu$  has a greater value for each case

except for  $Ra=50000$  and  $Q=2500$ . Infact, this case is special, because, in this study, dimensionless length in  $x$  direction being only half of that used in [20], is not sufficient, to include one more wave, therefore  $\zeta$  comes out to be slightly larger for  $Ra=50000$  and  $Q=2500$ . In other words, there exists three waves when  $Q<2500$  and the number of waves increases to five after the flow is reorganised when  $Q=2500$  in [20]. On the other hand, in the present work, there are two waves until  $Q=2750$  and due to the space restrictions only one additional wave develops when  $Q=2750$ .

Table 5.3: Nu and  $\zeta$ .  $Pr=0.05$ . Present work with  $\Gamma=3:1.5$  and  $\Gamma=6:3$  at [20]

Ra	Q	Present work		R.Möβner [17]	
		Nu	$\zeta$	Nu	$\zeta$
10000	50	2.39	1.5	-	-
	200	1.81	1.5	-	-
	400	1.18	1.5	-	-
30000	400	2.56	1.5	2.19	2.0
	900	1.86	1.5	1.57	2.0
	1400	1.52	1.0	-	-
	1900	1.07	1.0	-	-
50000	900	2.43	1.5	2.25	2.0
	2000	1.60	1.5	-	-
	2500	1.27	1.5	1.33	1.2
	2750	1.42	1.0	-	-
	3000	1.28	1.0	-	-

Results of our study are also compared with the correlation given in [21], an experimental research by Aurnou and Olson. In this study, a low Prandtl number fluid ( $Pr = 0.0023$ ), liquid gallium is used in a large convection tank ( $\Gamma = 8:8$ ). A correlation signifying basic balance between buoyancy and Lorentz force is established by combining it with the heat transfer due to convective motions:

$$Nu = 0.23 \left( \frac{Ra}{Q} \right)^{0.5 \pm 0.03} \quad \text{for } 25 < \frac{Ra}{Q} < 60. \quad (5.4)$$

This correlation is only valid in a specific range of  $Ra / Q$ . As shown in Figure 5.8, the best fit to the data in this specific range selected from Figure 5.3 have approximately a slope of 0.5 as suggested by (5.4).

Absence of parallel side walls and absence of Hartmann breaking on top and bottom rigid boundaries leads to an increase in  $Nu$  in the present work. Insulated or not ideally conducting boundaries in this experimental study cause inhibition of motion by means of Hartmann layers in which there exist currents parallel to the walls.

As  $Ra$  decreases, strength of the magnetic field,  $Q$  required for the onset of a steady motion, also drops. Power-law fit (5.4) to the  $Nu-Ra$  results in [21] is obtained for a constant value  $Q = 670$ . This law is shown to hold in the present study within the range of  $(Ra, Q)$  values specified in [21].

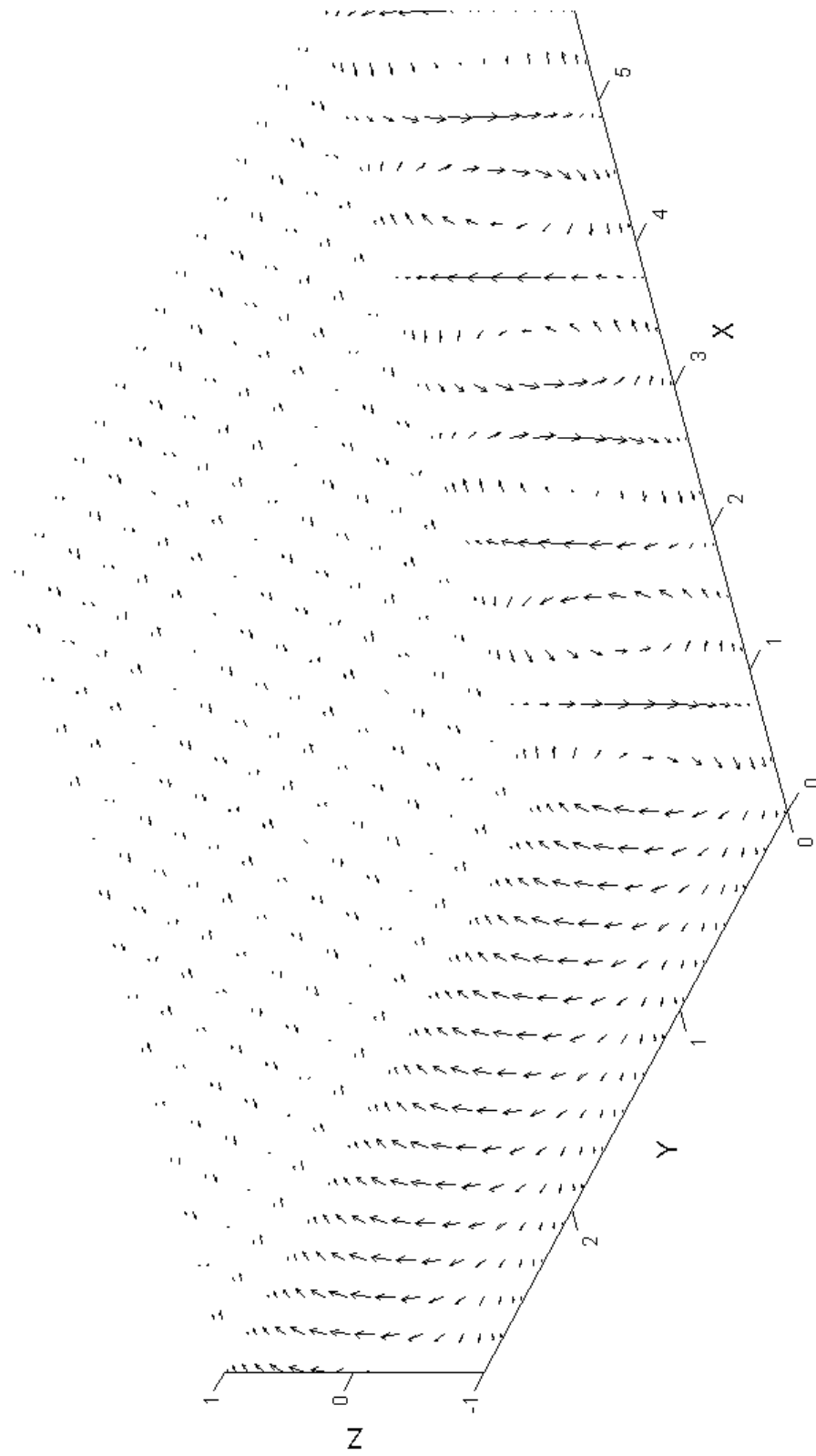


Figure 5.1 Velocity field,  $Ra=30000$ ,  $Pr=0.05$  and  $Q=1700$ .

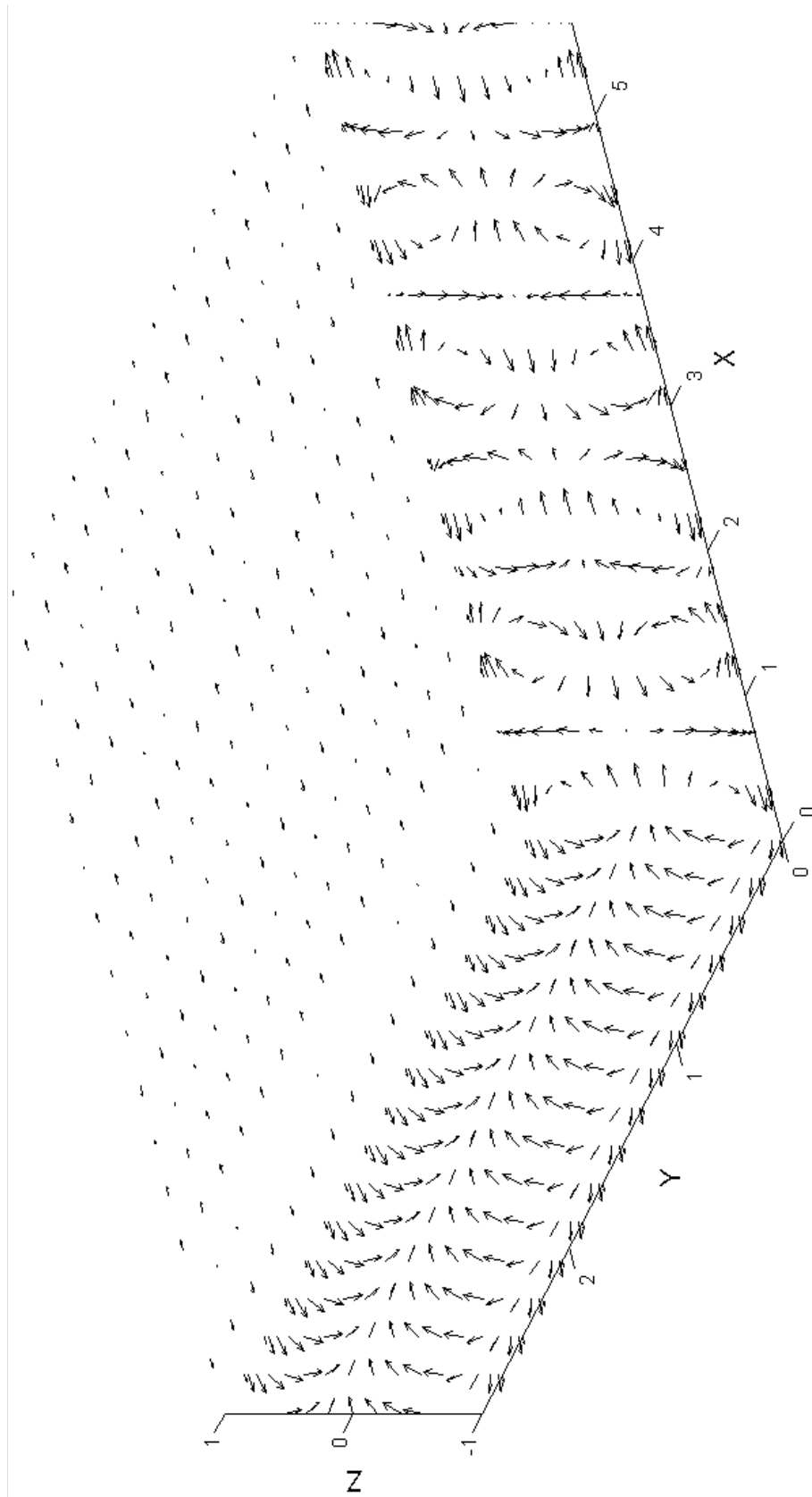


Figure 5.2 Induced magnetic field,  $Ra=30000$ ,  $Pr=0.05$ ,  $Q=1700$ .

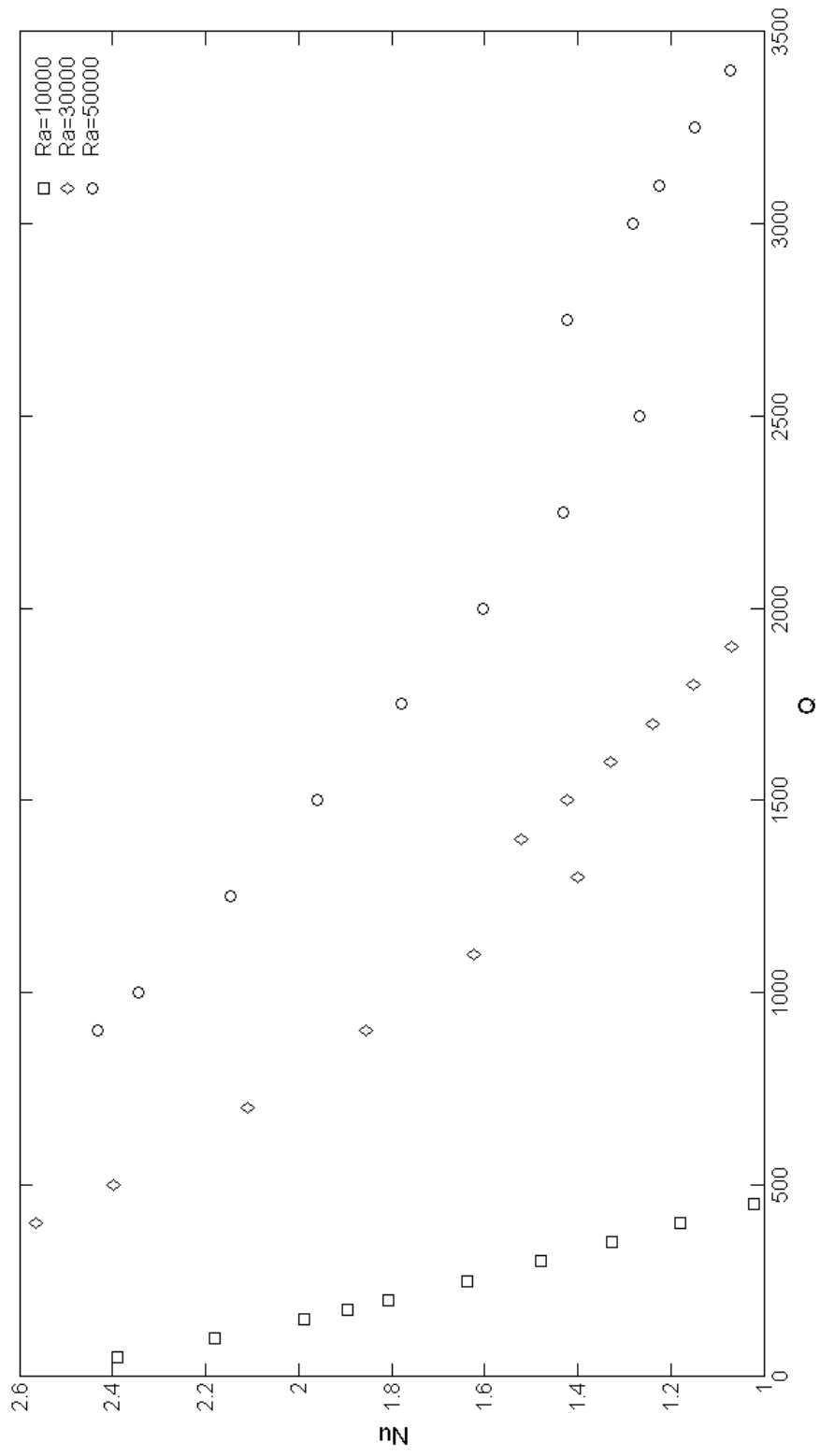


Figure 5.3 Nu vs. Q with Ra=10000, Ra=30000 and Ra=50000 for Pr=0.05.

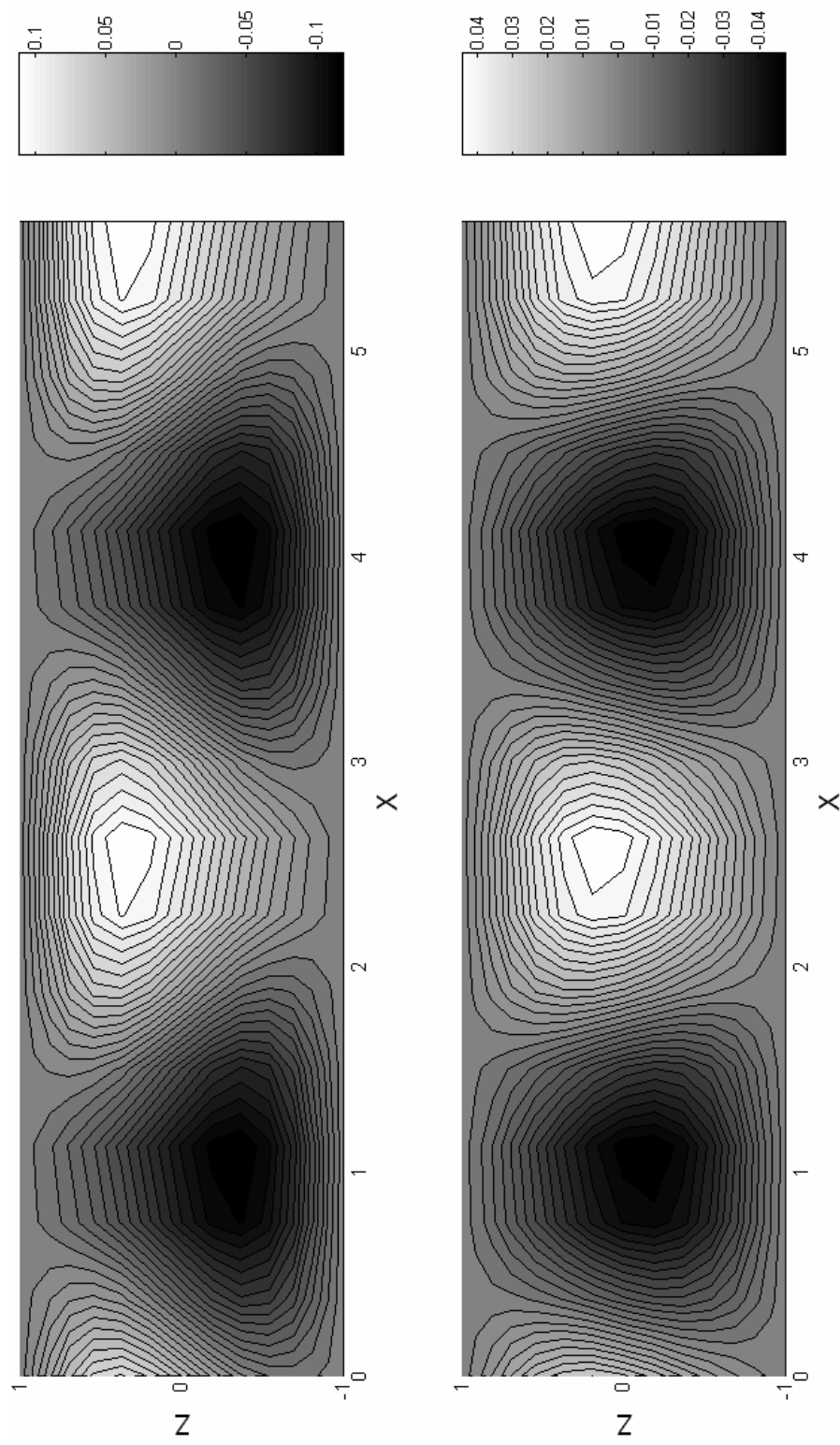


Figure 5.4 Temperature contours on  $xz$  plane at  $y=0.375$ .  $Ra=30000$ ,  $Pr=0.05$  and  $Q=1700$ . Restructuring of rolls from steady case at  $Q=1100$ .  $t=0$  and  $t=2$ .

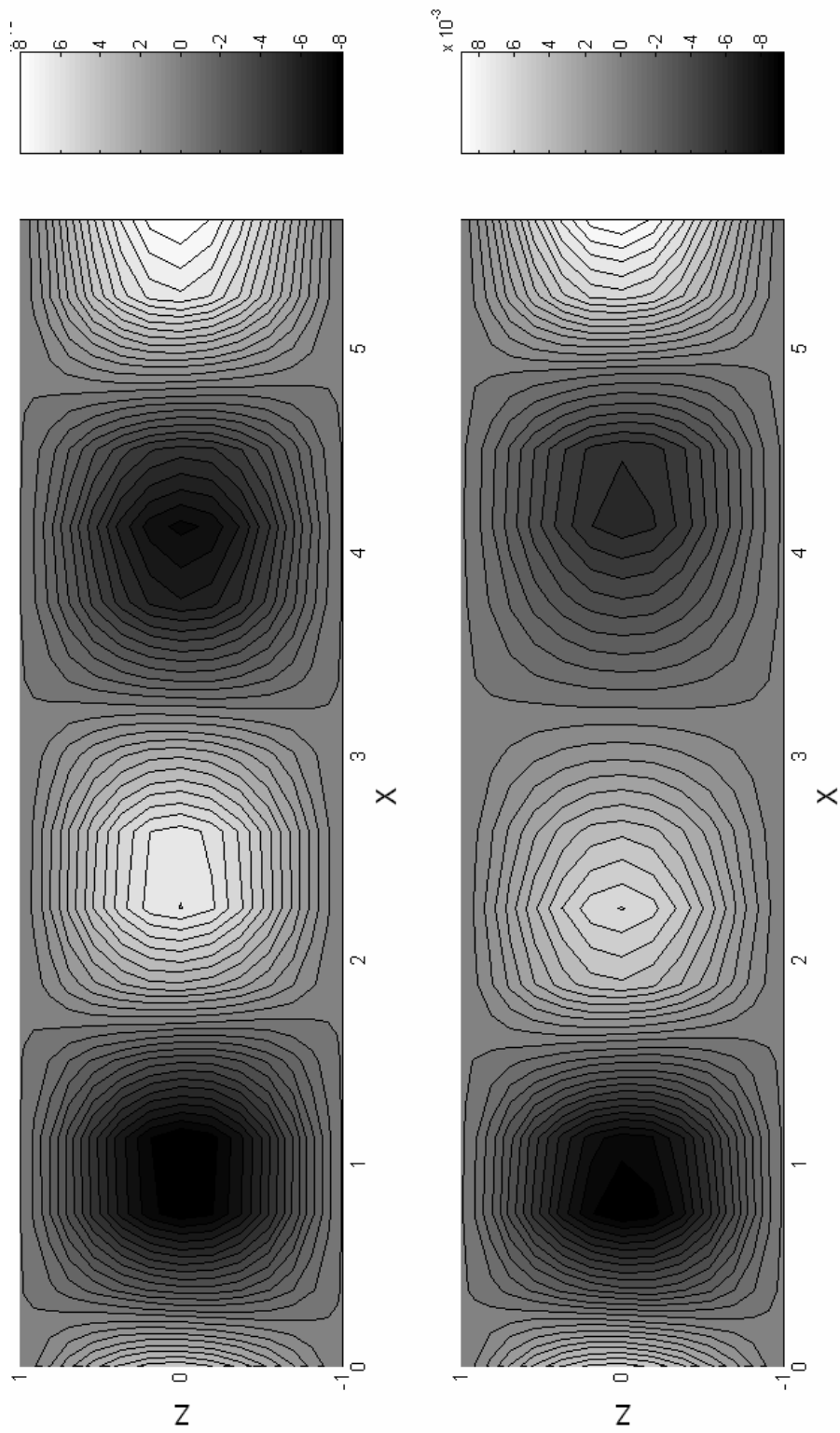


Figure 5.5 Temperature contours on xz plane at  $y=0.375$ .  $Ra=30000$ ,  $Pr=0.05$  and  $Q=1700$ . Restructuring of rolls from steady case at  $Q=1100$ .  $t=34$  and  $t=36$ .

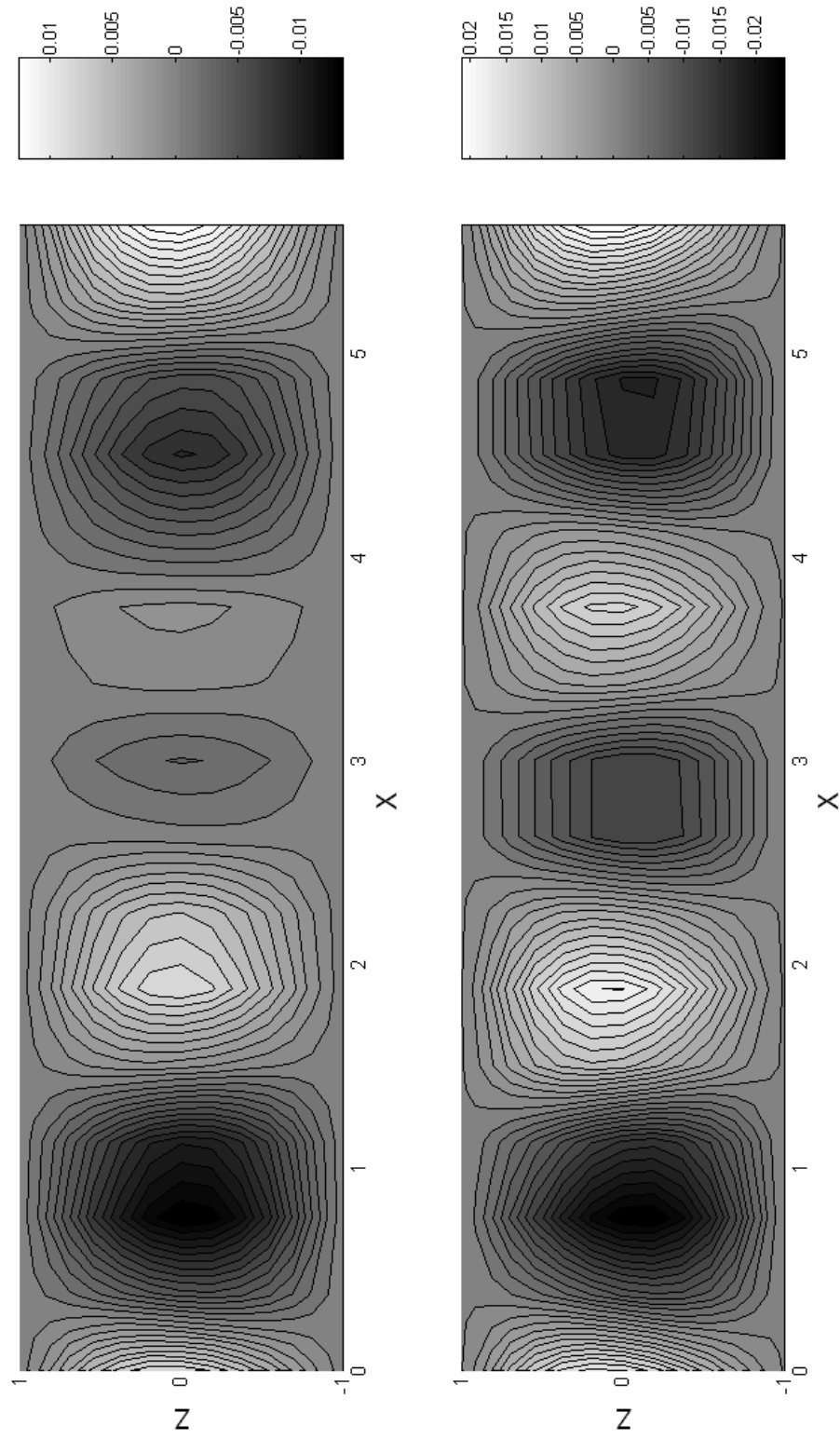


Figure 5.6 Temperature contours on xz plane at  $y=0.375$ .  $Ra=30000$ ,  $Pr=0.05$  and  $Q=1700$ . Restructuring of rolls from steady case at  $Q=1100$ .  $t=38$  and  $t=42$ .

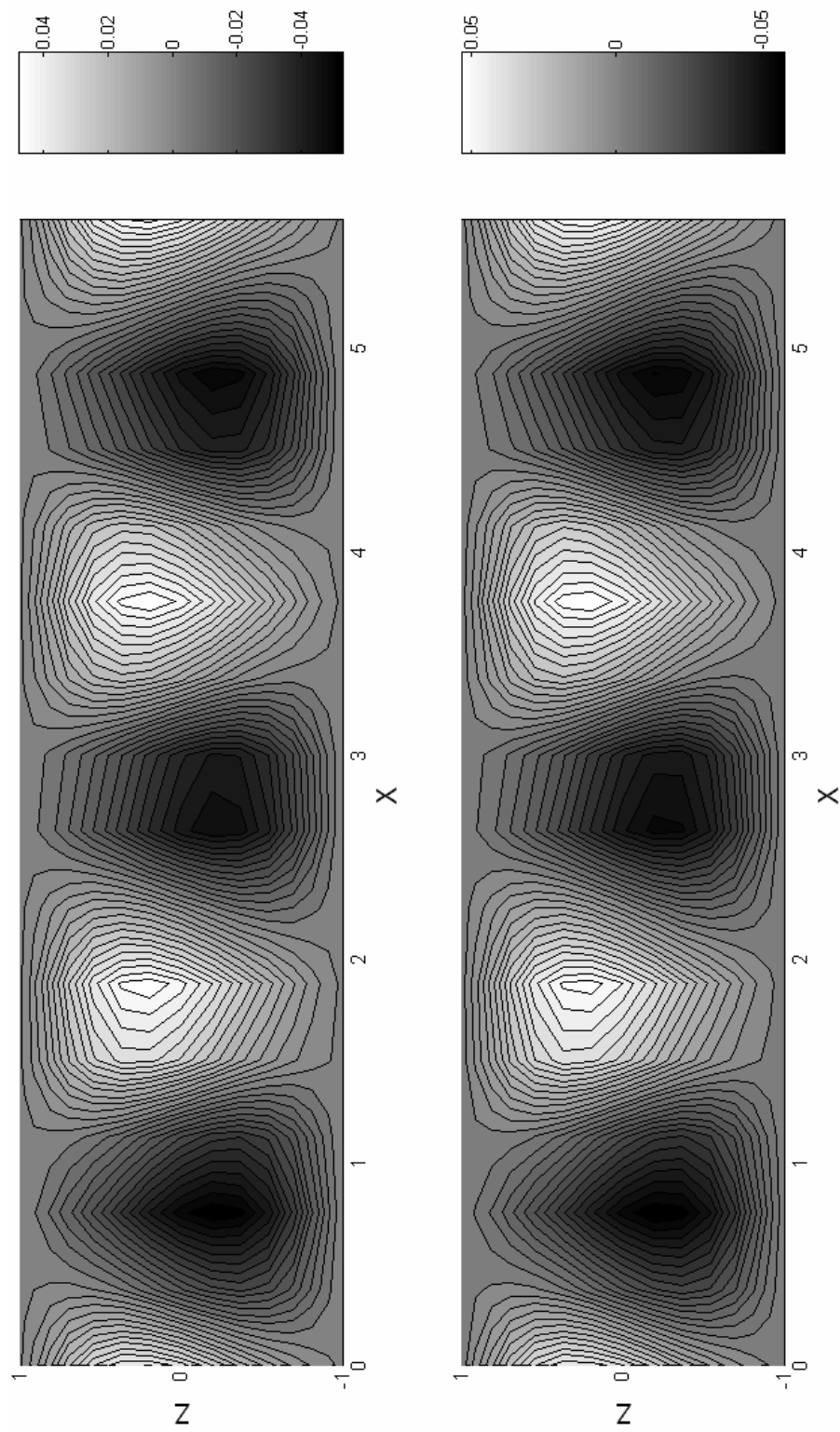


Figure 5.7 Temperature contours on xz plane at  $y=0.375$ .  $Ra=30000$ ,  $Pr=0.05$  and  $Q=1700$ . Restructuring of rolls from steady case at  $Q=1100$ .  $t=43$  and  $t=45$ .

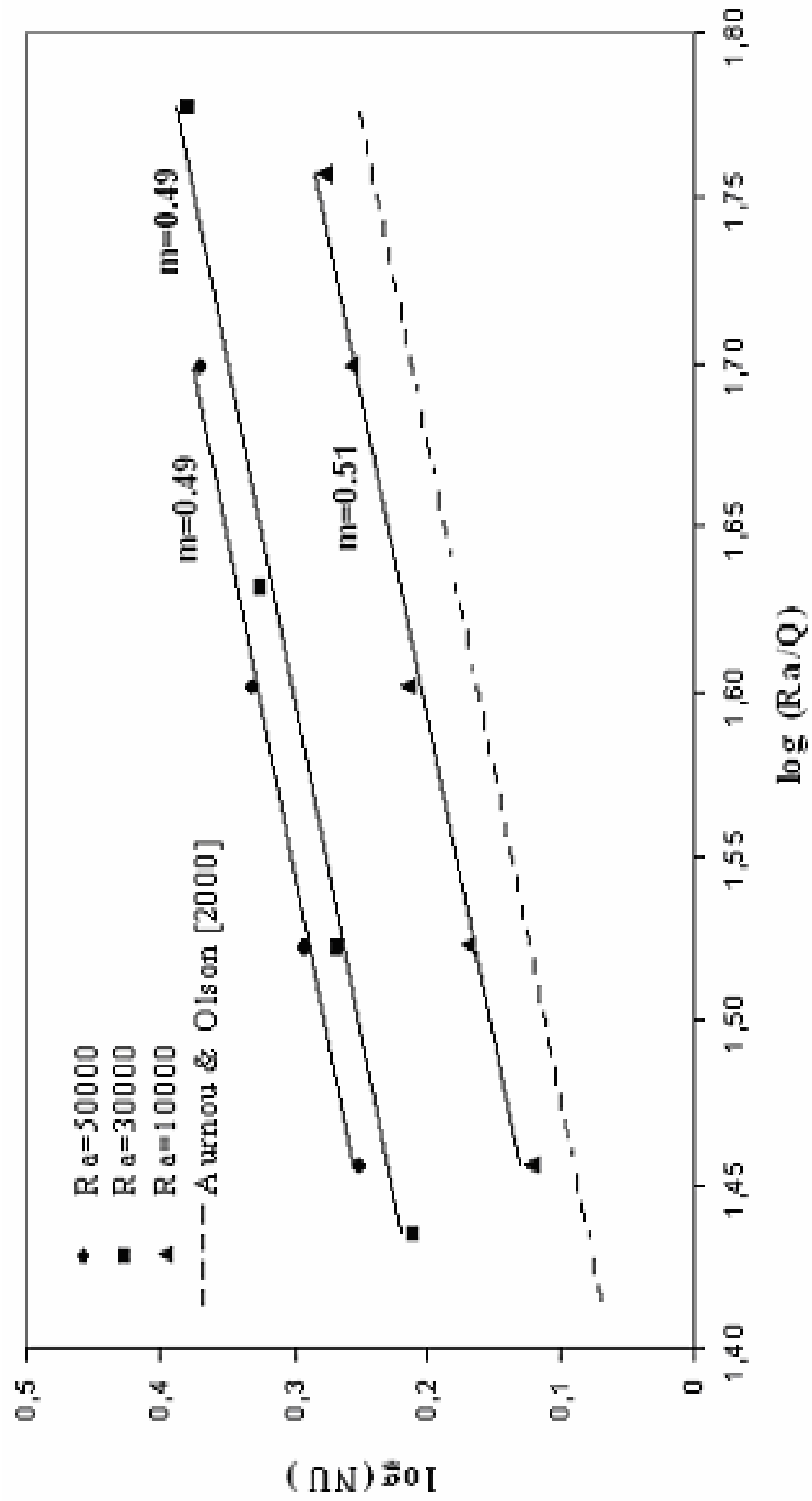


Figure 5.8 Nu vs. Ra/Q in log scale.

## 5.2 Time Dependent Flows

In the previous section, inhibition of convection rolls at given value of Ra is investigated under the varying strength of a vertical magnetic field. This time, the strength of the magnetic field is kept constant at a particular value, while Ra across the fluid layer is increased and the direction angle  $\chi$  of the external magnetic field is changed in the  $yz$  plane measured from the horizontal. The aspect ratio  $\Gamma = 1.95:1.90$ ,  $Pr = 0.1$  and  $Q = 100$  are chosen in order to be able to compare with the results of Clever and Busse [13] for the case  $\chi = 90^\circ$ . In Figure 5.9, Nu–Ra relation for pure convection ( $Q = 0$ ) and for various direction angles of external field are illustrated.

Critical values are given in Table 5.4 computed by extrapolation of values in the steady regime. It is clear that they are all slightly greater than those given in [13], because a larger aspect ratio is used in the present work which translates into a wavelength of  $\zeta = 2\pi/1.95 = 3.2$ . This value is smaller than that is used in the work of Busse and Clever [13] except for the case of pure convection. Results from present work approach to the critical Ra values in [13] when critical value of wavelength,  $\zeta_c$  is closer to  $\zeta = 3.2$ .

The critical value of Ra,  $Ra_c$ , for the onset of the convective motion increases with increasing  $\chi$  for a given Q, that is with decreasing the horizontal component of the inclined magnetic field (Figure 5.9). It means that onset of convection is delayed by the vertical component of the inclined magnetic field. Chandrasekhar [1], Busse [13] and

Burr [16] state that the horizontal component of magnetic field along roll direction has no effect on the steady convection rolls unless the roll solution is close to losing its stability. This fact is also seen in this study. Stationary system of parallel rolls occurs at slightly above  $Ra_c$  as usual. Since oscillatory instability of rolls is much more effectively inhibited by the magnetic field and by the orientation angle in comparison to the onset of convection leading to the roll motion, the stability range of roll motion is enlarged by the effect of these parameters. A rapid drop in the slope of the Nu-versus-Ra curve seems to occur immediately as the steady region gives way to the oscillatory regime. These rolls appear to oscillate with travelling waves at  $Ra=12000$  for  $\chi = 90^\circ$  but infact, these waves are formed in  $10000 < Ra < 12000$  range.

Figures 5.10 and 5.11 show the steady parallel rolls in the  $x y$  plane. Flow moves in opposite directions between half layers, in which  $z = 0$  is the mid-plane. In the second figure, it is shown that velocity vectors depart from the hot region to cold region.

In the study of Clever and Busse [13], oscillations are stated to begin at  $Ra=11090$  which is in agreement with the present work. In gathering Nu values from [13], the added restriction of vanishing average pressure is taken into consideration. In general, except for slight differences in oscillatory regime, results are seemed to be compatible with the semi-analytical treatment in [13]. When the results of inclined magnetic field imposed are analyzed, it seems that

horizontal components of external field delay oscillatory instability more efficiently than the vertical. In fact, Busse et al. [13] states that the horizontal field has a more inhibiting effect on the oscillatory instability than the vertical field. The regime on which inclined magnetic field is applied is stable in a larger range of Ra when compared with the flow influenced by purely vertical magnetic field. In the steady regime, horizontal component does not play an essential role, in other words, as horizontal magnetic field strength grows, change in Nu becomes insignificant until Ra is 2800 however heat transfer efficiency and stability come into prominence in the regime of the oscillatory instability. It appears that travelling wave motion is the dominant feature at the onset of the unsteady regime of the usual Rayleigh Benard convection ( $Q=0$ ) and the magneto-convection ( $Q=100$ ) with all angles except for the case,  $\chi = 30^\circ$  .

The amplitude of oscillations rises when  $Ra > 12000$  for  $\chi = 60^\circ$  ,  $Ra > 14000$  for  $\chi = 45^\circ$  ,  $Ra > 18000$  for  $\chi = 30^\circ$  . Periodic motion is observed in the case of  $\chi = 60^\circ$  , where the velocity in the  $x$  direction shows the major harmonic behaviour. Figures 5.12 and 5.13 show the variation of the  $x$  component of the velocity field at a point  $x = 0.4875$ ,  $y = 0.475$  and  $z = -0.9109$  in the oscillatory regime. Here, the frequency of these waves is approximately 0.9. The flow sequence is depicted in the interval from  $t = 10$  to  $t = 10.45$ , and at  $t = 10.45$  a half-period duration of this motion is nearly completed (from Figures 5.14 to 5.17). In fact, the period computed using the frequency diagram (Figure 5.18) for the time variation in  $\mathbf{u}_x$  at the given point is 1.005.

By extending these studies towards the greater Ra values for  $\chi = 60^\circ$ , there seems to be some other periodic modes contributing to the flow. In the time variation of  $u_x$ ,  $u_y$ ,  $u_z$  and  $\Theta$ , additional waves with smaller periods mount onto the major wave (Figures 5.20 and 5.21). Oscillations in the form of travelling waves appear along the temperature contours in the horizontal plane from  $t=10$  to  $t=10.45$  in Figures 5.22 to 5.25. In these figures, nearly half of the travelling wave motion is shown. Complexity in the flow increases with waves having larger frequencies. On the other hand, the period of travelling waves gets smaller, decreasing from 1.005 to 0.870 (Figure 5.26). This fact can be seen clearly in the frequency spectrum plots; here the most energetic peak is shifted. In this frequency diagram, besides the peaks representing the main periodic behaviour in the flow, there exist peaks at various frequency values.

Table 5.4- Extrapolated values of  $Ra_c$  ( $Nu=1$ ) from Figure 5.9 for  $Q=0$  and  $Q=100$  at  $\chi = 30^\circ$ ,  $\chi = 45^\circ$ ,  $\chi = 60^\circ$  and  $\chi = 90^\circ$ .

	Q = 0	Q = 100 $\chi = 30^\circ$	Q = 100 $\chi = 45^\circ$	Q = 100 $\chi = 60^\circ$	Q = 100 $\chi = 90^\circ$
$\zeta_c$ B.C. [1990]	3.12	3.45	3.68	3.86	4.01
$Ra_c$ ( $\zeta = 3.2$ ) P.W.	1746	2327	2846	3434	3998
$Ra_c$ ( $\zeta = \zeta_c$ ) B.C. [1990]	1708	2281	2800	3291	3757

Transition to the oscillatory regime follows two dimensional steady parallel roll motion for  $\chi$  at  $45^\circ$ ,  $60^\circ$  and  $90^\circ$ .

However at  $\chi = 30^\circ$ , some other instability pattern seems to occur following the steady roll motion, differing from oscillations with travelling waves. Two new types of instability are presented in [13] which can be observed when the external magnetic field is applied in the horizontal direction, namely, monotonic wrinkle and oscillatory tilt. Monotonic wrinkle exhibits itself as closed contours located inside a roll pattern. In the present work, only the monotonic wrinkle is observed during the steady regime only at  $\chi = 30^\circ$  driving the flow into a three dimensional steady state. Time-independent 3D rolls keep their steadiness until Ra is 15000. The closed contours inside the monotonic wrinkle region start expanding and shrinking periodically after as Ra is increased from 15000 to 20000 (Figures 5.28 to 5.30). In these figures, time sequence from  $t = 5$  to  $t = 7$  is shown for the case Ra=18000 at which the period is exactly 2. Frequency spectrum of the temperature variation at the point  $x = 0.4875$ ,  $y = 0.475$  and  $z = -0.9109$  shows the peak exactly at this single period.

The other type of instability, which is observed specifically in the case of the inclined magnetic field imposed, is the oscillatory tilt. In this case, the dimensions in the horizontal directions are reduced by half and the aspect ratio is taken as  $\Gamma = 0.975:0.95$ . Flow pattern in the  $xy$  plane with the temperature contours shows asymmetric waves but this pattern eventually shifts to the left as demonstrated by the time sequences from  $t = 5.1$  to  $t = 5.68$  in Figures 5.33 to 5.41. Exact value of the period of the motion of the oscillatory tilt is 0.533. In the frequency spectrum (Figure 5.42), oscillatory

tilt action is shown by the peak with the greatest amplitude and the other peak may be associated with the asymmetric wave motion in the flow.

The relationship between kinetic and magnetic energy versus the orientation angle in Figure 5.43 implies that by the help of these unusual pattern formations, i.e. the monotonic wrinkle, the onset of oscillatory regime is still delayed even though the flow motion gains much more kinetic energy. Kinetic energy of motion increases as the direction of the external magnetic field approaches horizontal. On the contrary, strength of the induced magnetic field in all directions decreases to negligible levels. This observation shows that flow under the effect of a horizontal magnetic field emerges as more energetic due to less Joule dissipation and stable.

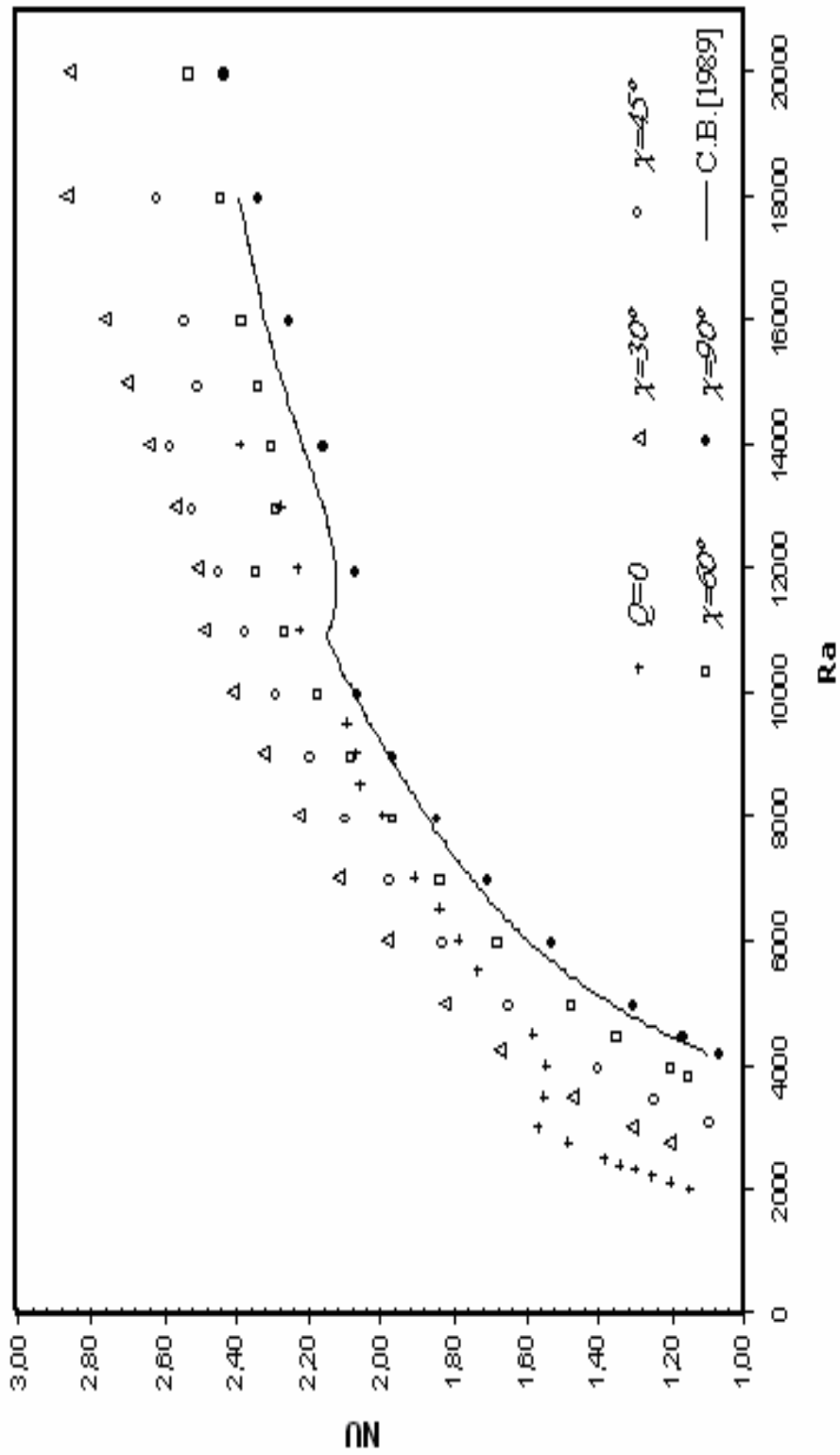


Figure 5.9 Nu vs. Ra for Pr=0.1 when Q=100.

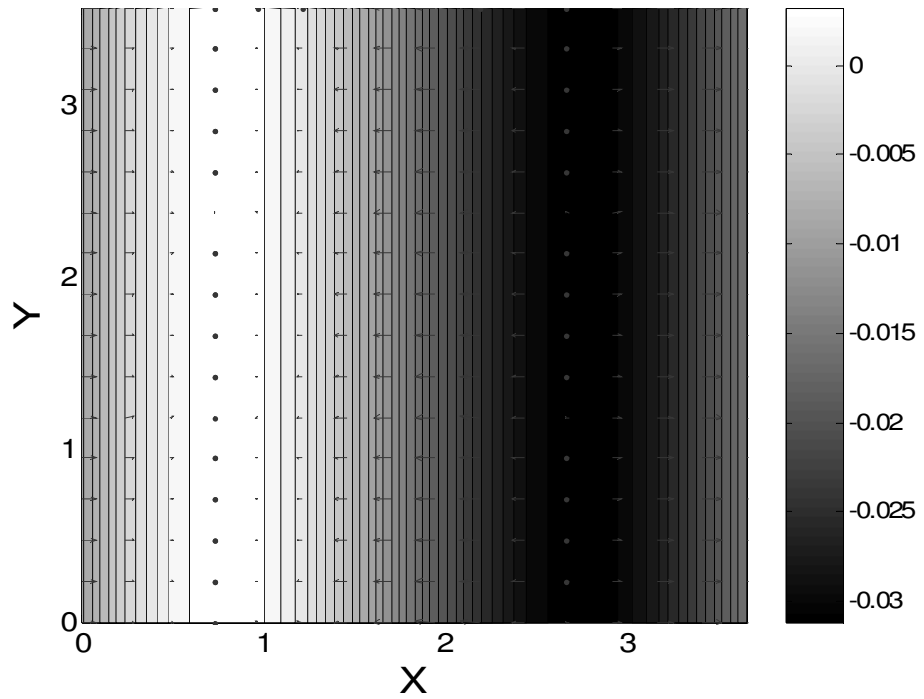


Figure 5.10 Velocity field and  $\Theta$  contours on  $xy$  plane at  $z = -0.9109$ ,  $Ra = 10000$ ,  $Pr = 0.1$ ,  $Q = 100$  and  $\chi = 90^\circ$ . ( $\Gamma = 1.95 : 1.90$ )

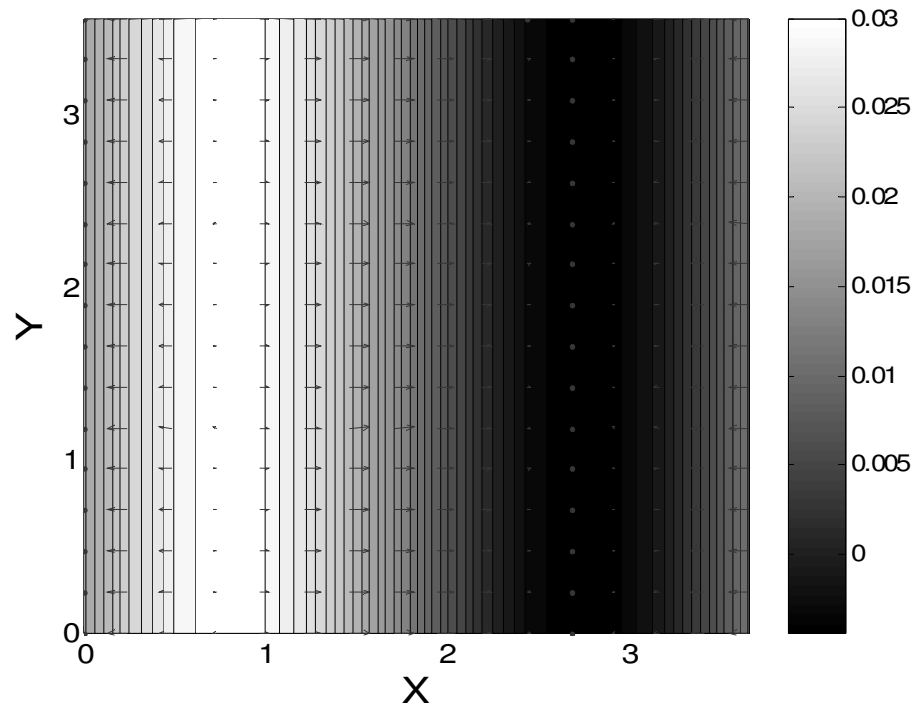


Figure 5.11 Velocity field and  $\Theta$  contours on  $xy$  plane at  $z = 0.9109$ ,  $Ra = 10000$ ,  $Pr = 0.1$ ,  $Q = 100$  and  $\chi = 90^\circ$ . ( $\Gamma = 1.95 : 1.90$ )

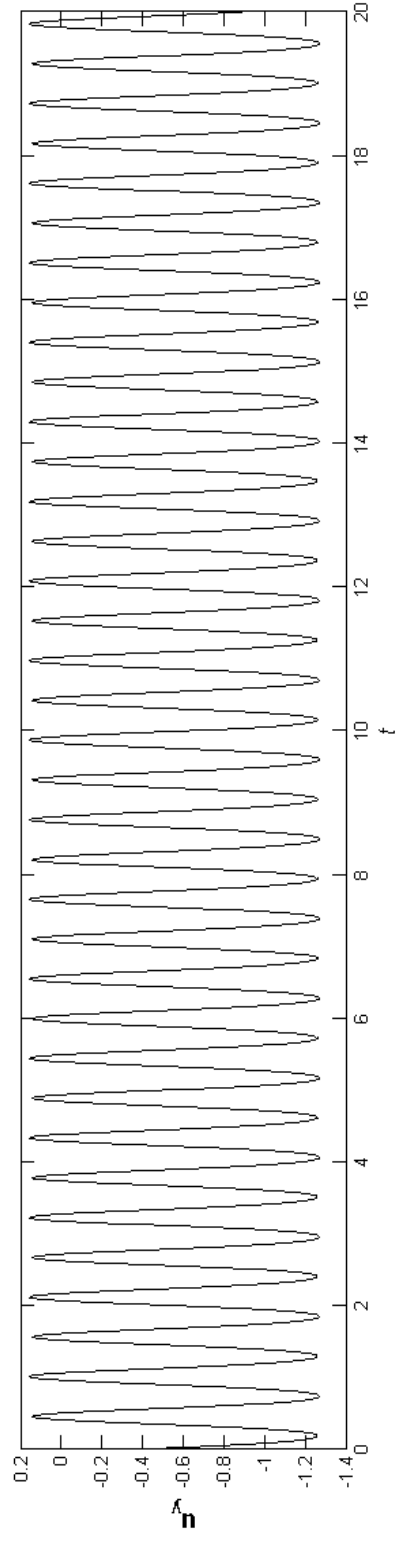
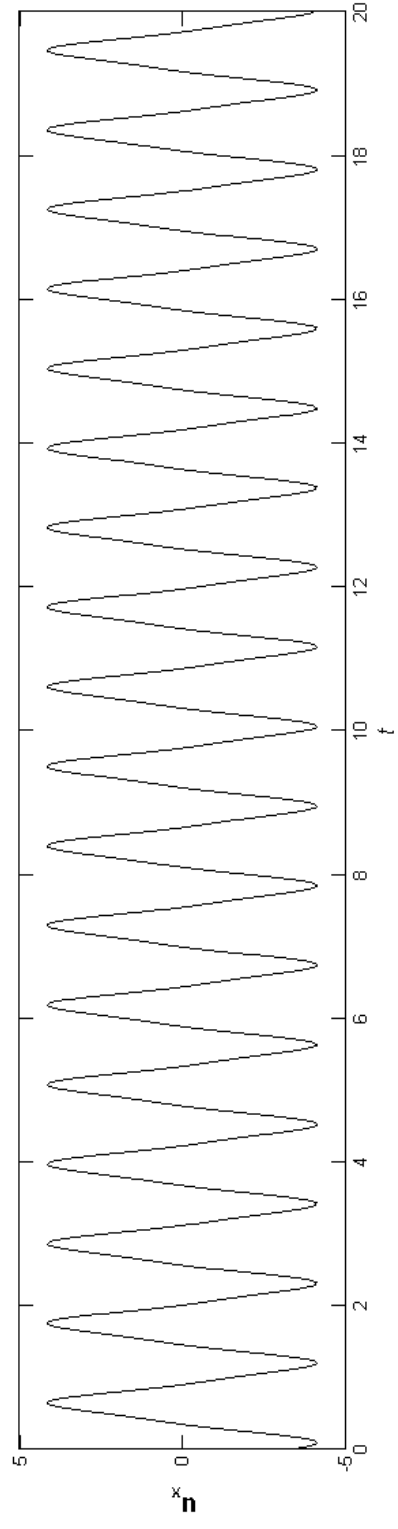


Figure 5.12 x and y components of velocity field vs.t at  $x=0.4875$ ,  $y=0.475$  and  $z=-0.9109$  for  $Ra=14000$ ,  $Pr=0.1$ ,  $Q=100$  and inc. angle is 60 degree.

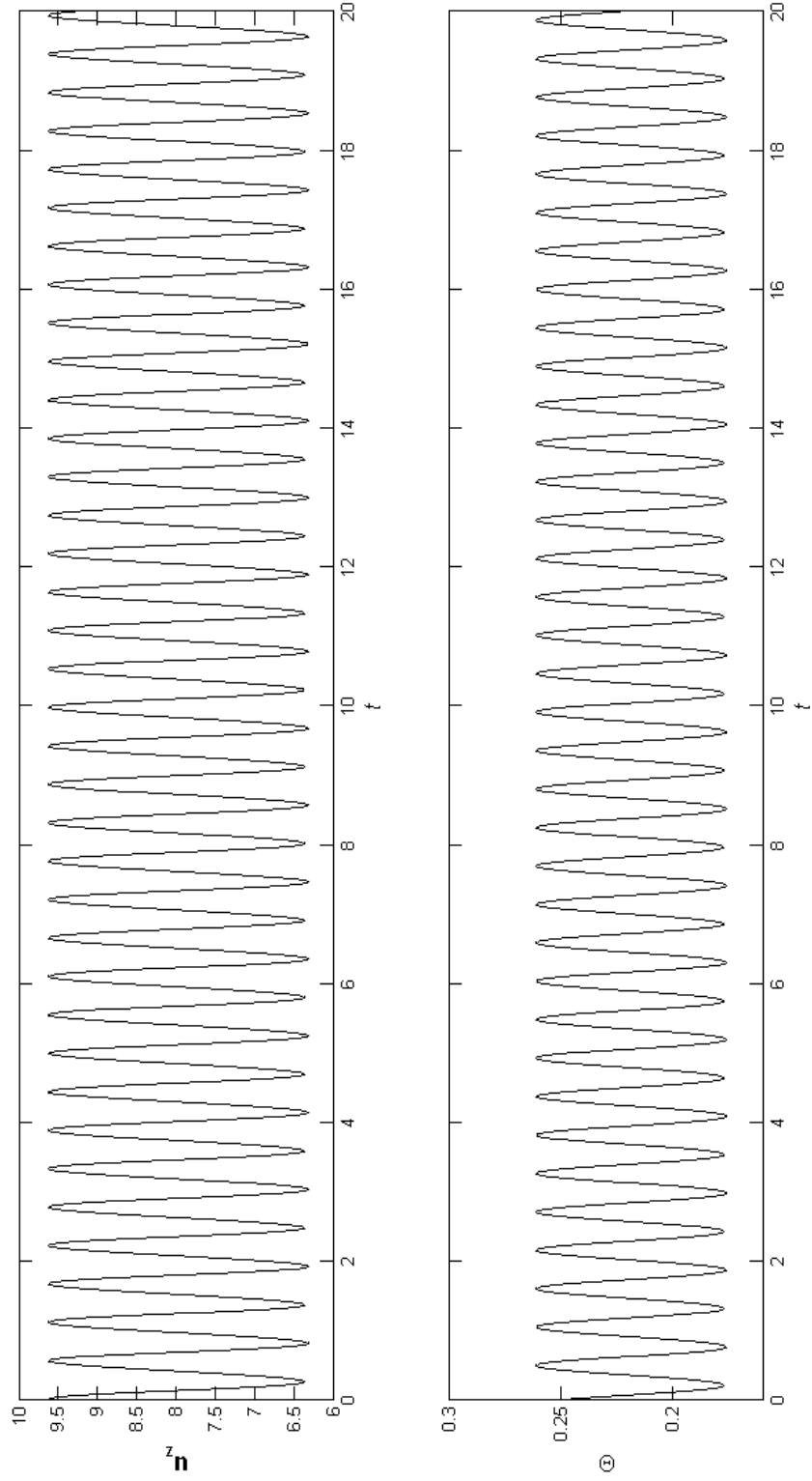


Figure 5.13 z component of velocity and temperature fields vs.t at  $x=0.4875$ ,  $y=0.475$  and  $z=-0.9109$  for  $Ra=14000$ ,  $Pr=0.1$ ,  $Q=100$  and inc. angle is 60 degree.

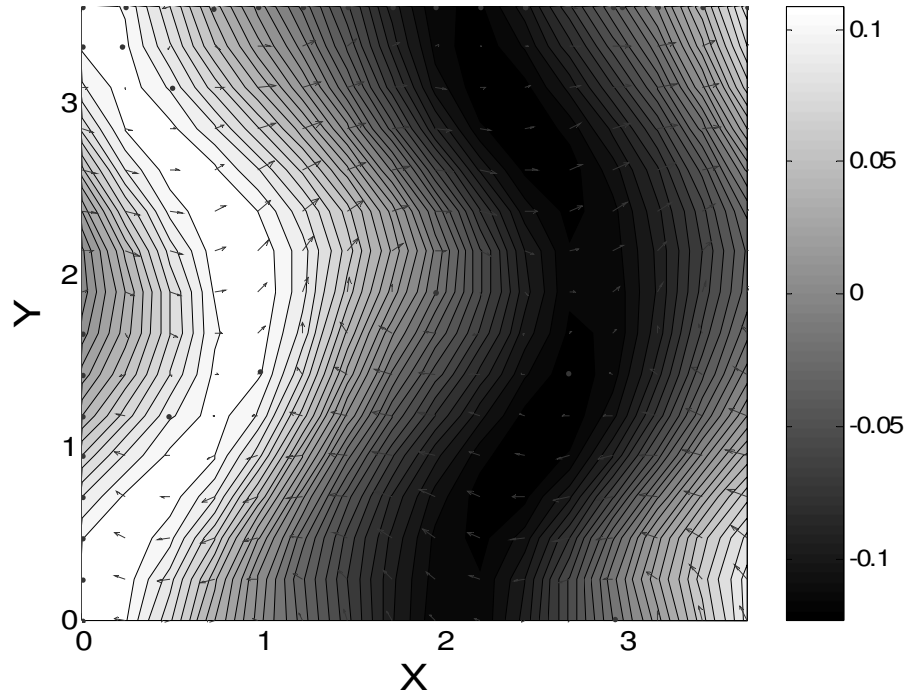


Figure 5.14 Velocity field and  $\Theta$  contours on  $xy$  plane at  $z=0$  and  $t=10$ .  $Ra=14000$ ,  $Pr=0.1$ ,  $Q=100$  and  $\chi=60^\circ$ . ( $\Gamma=1.95:1.90$ )

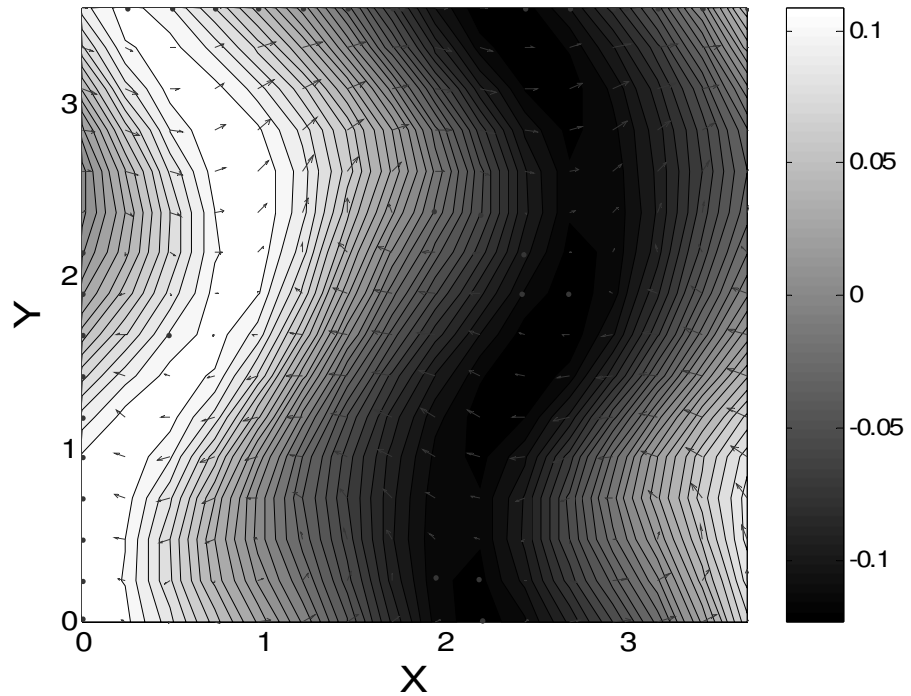


Figure 5.15 Velocity field and  $\Theta$  contours on  $xy$  plane at  $z=0$  and  $t=10.15$ .  $Ra=14000$ ,  $Pr=0.1$ ,  $Q=100$  and  $\chi=60^\circ$ . ( $\Gamma=1.95:1.90$ )

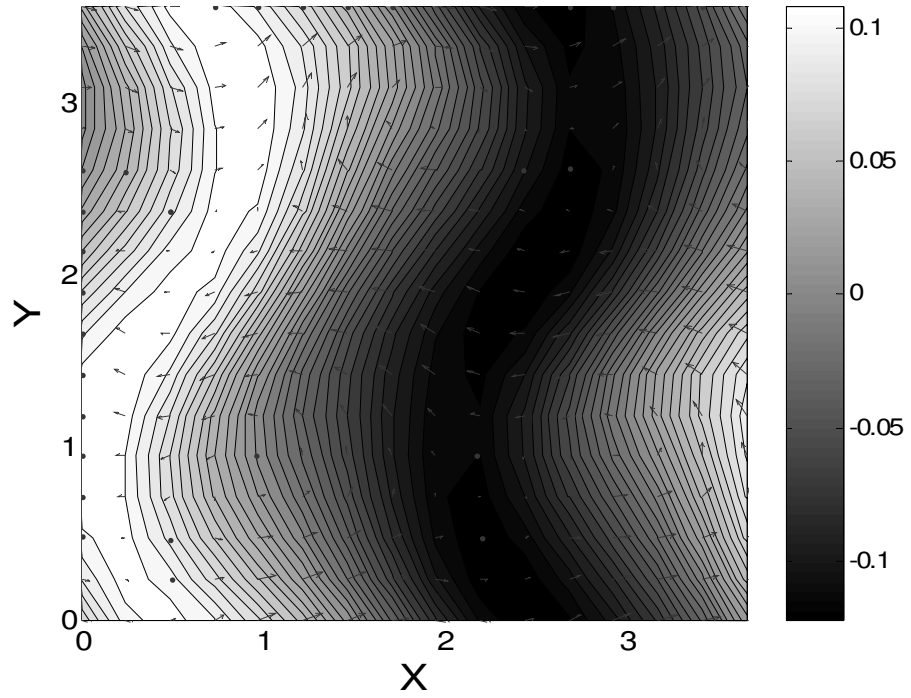


Figure 5.16 Velocity field and  $\Theta$  contours on  $xy$  plane at  $z=0$  and  $t=10.30$ .  $Ra=14000$ ,  $Pr=0.1$ ,  $Q=100$  and  $\chi=60^\circ$ . ( $\Gamma=1.95:1.90$ )

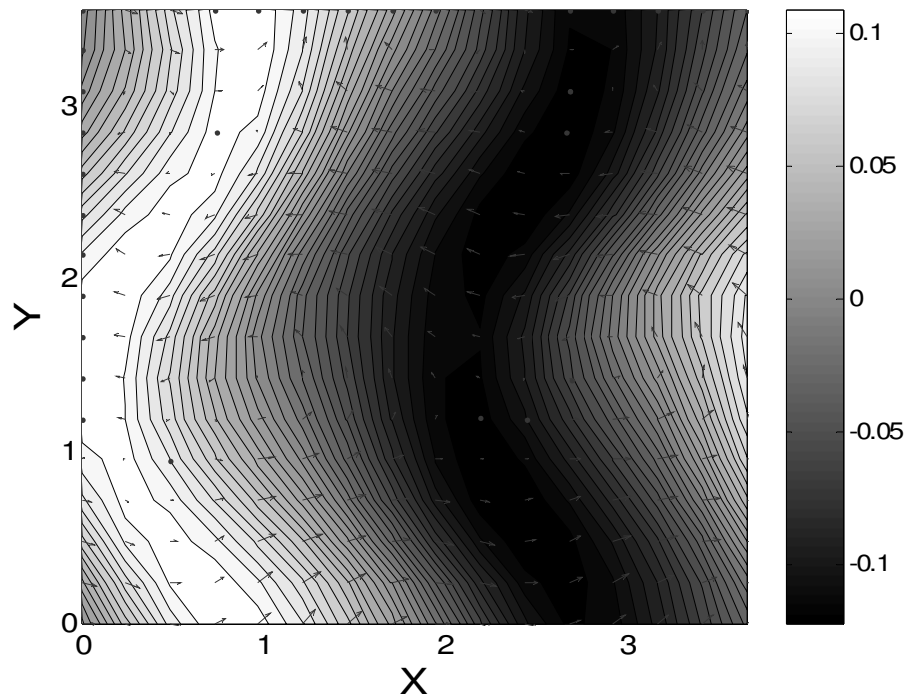


Figure 5.17 Velocity field and  $\Theta$  contours on  $xy$  plane at  $z=0$  and  $t=10.45$ .  $Ra=14000$ ,  $Pr=0.1$ ,  $Q=100$  and  $\chi=60^\circ$ . ( $\Gamma=1.95:1.90$ )

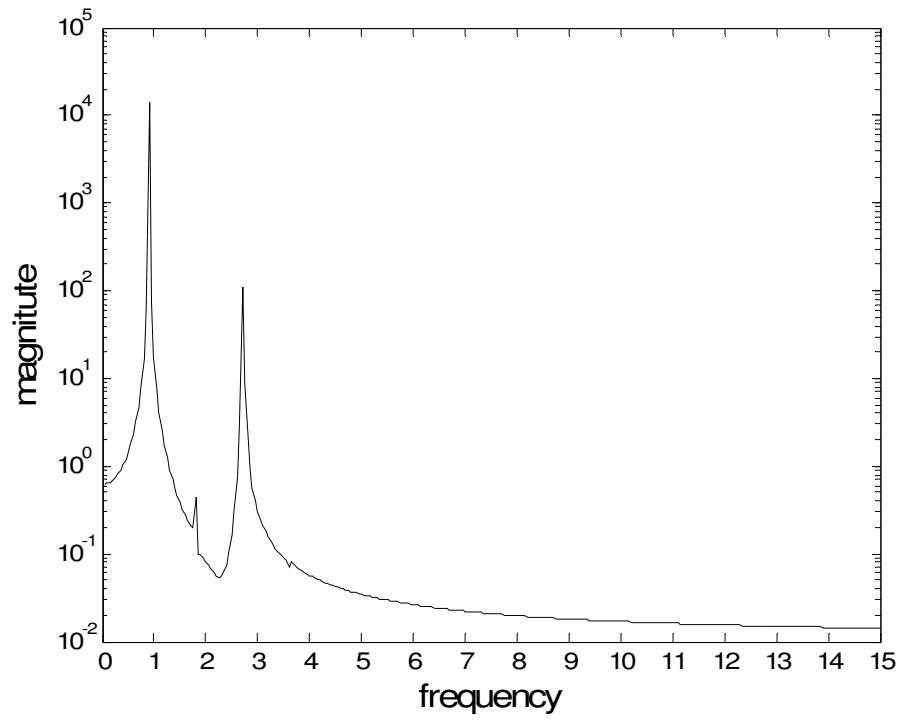


Figure 5.18 Frequency spectrum of  $u_x$  at  $x = 0.4875$ ,  $y = 0.475$  and  $z = -0.9109$  for  $Ra = 14000$ ,  $Pr = 0.1$ ,  $Q = 100$  and  $\chi = 60^\circ$ . ( $\Gamma = 1.95 : 1.90$ )

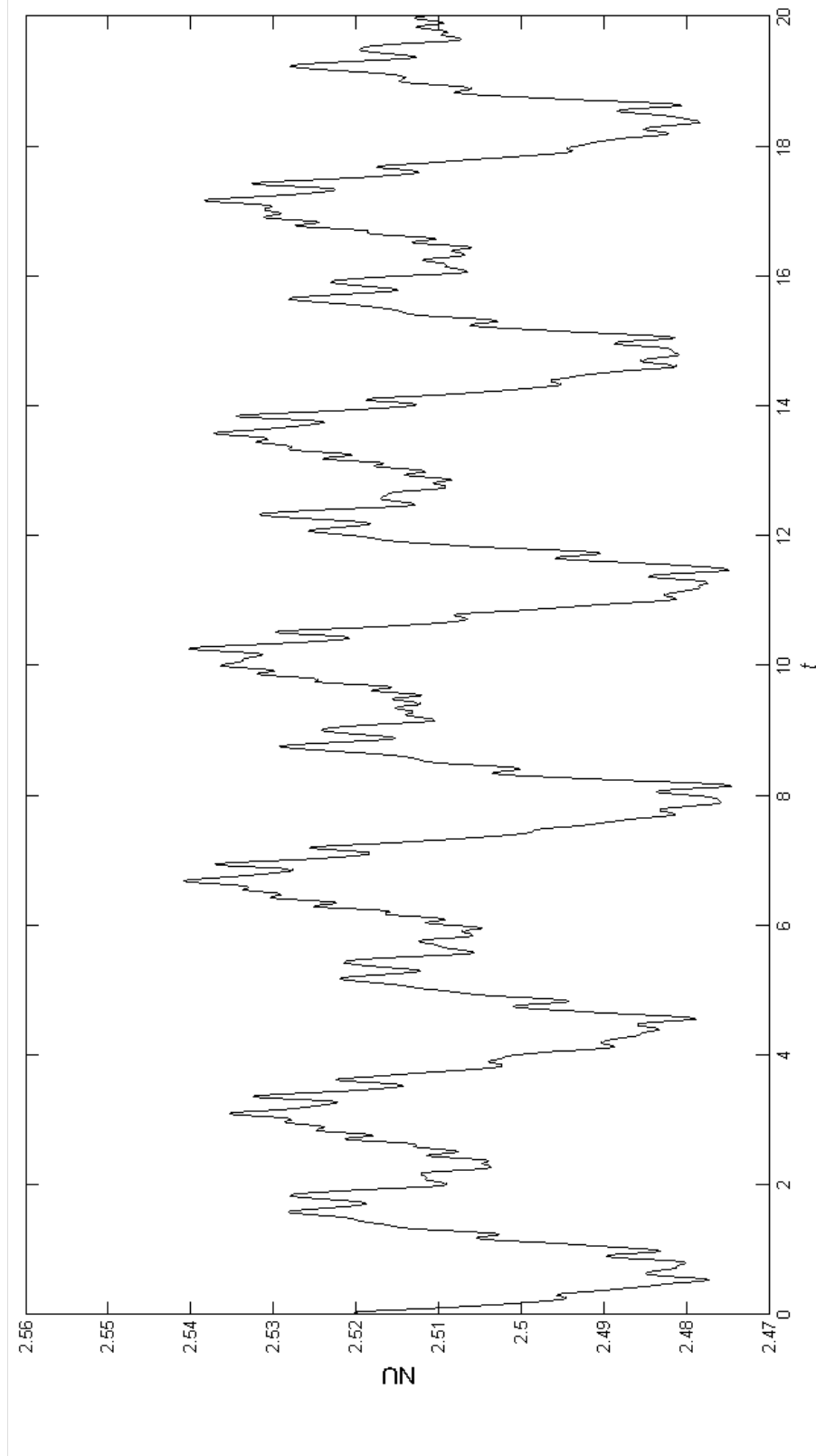


Figure 5.19 Nu vs.  $t$  at  $z=0$  for  $Ra=20000$ ,  $Pr=0.1$ ,  $Q=100$  and inc. angle is 60 degree.

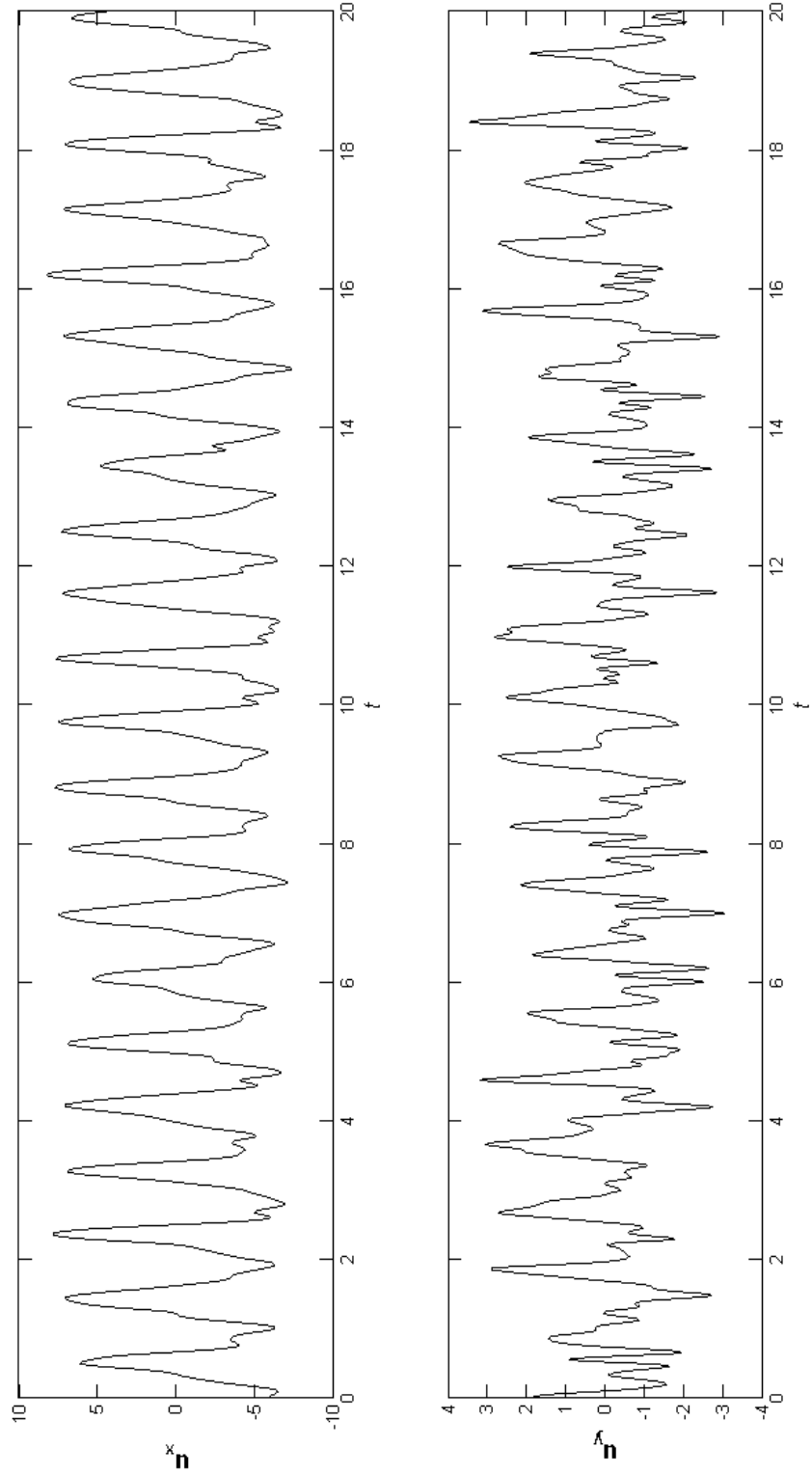


Figure 5.20 x and y components of velocity field vs.t at  $x=0.4875$ ,  $y=0.475$  and  $z=-0.9109$  for  $Ra=20000$ ,  $Pr=0.1$ ,  $Q=100$  and inc. angle is 60 degree.

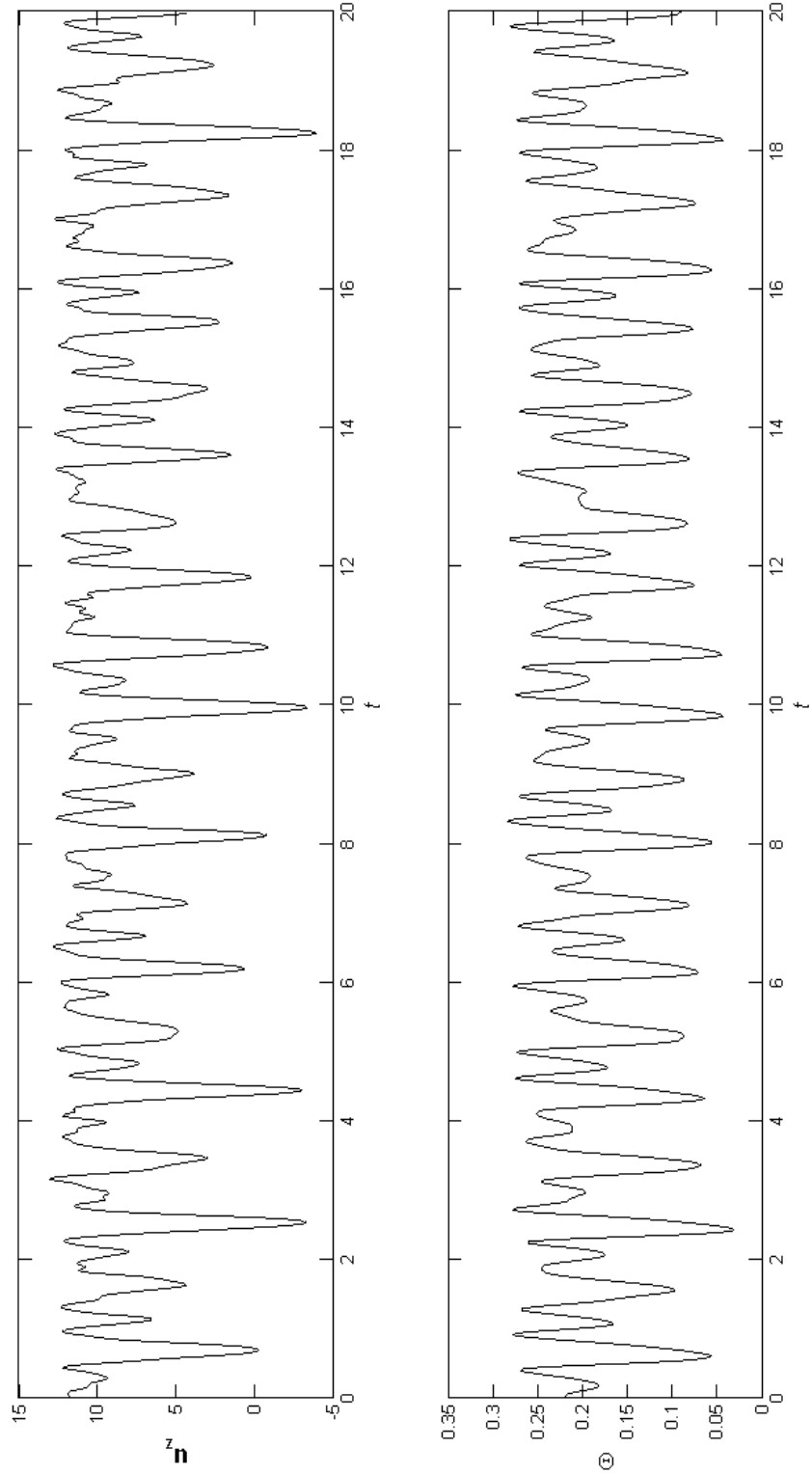


Figure 5.21 z component of velocity and temperature fields vs.t at  $x=0.4875$ ,  $y=0.475$  and  $z=-0.9109$  for  $Ra=20000$ ,  $Pr=0.1$ ,  $Q=100$  and inc. angle is 60 degree.

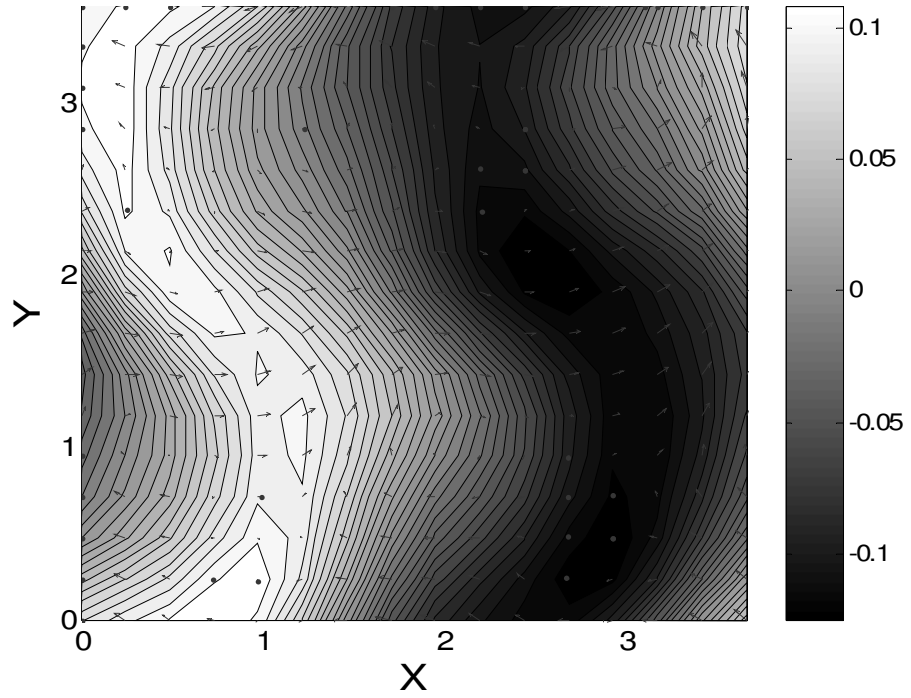


Figure 5.22 Velocity field and  $\Theta$  contours on  $xy$  plane at  $z=0$  and  $t=10$ .  $Ra=20000$ ,  $Pr=0.1$ ,  $Q=100$  and  $\chi=60^\circ$ . ( $\Gamma=1.95:1.90$ )

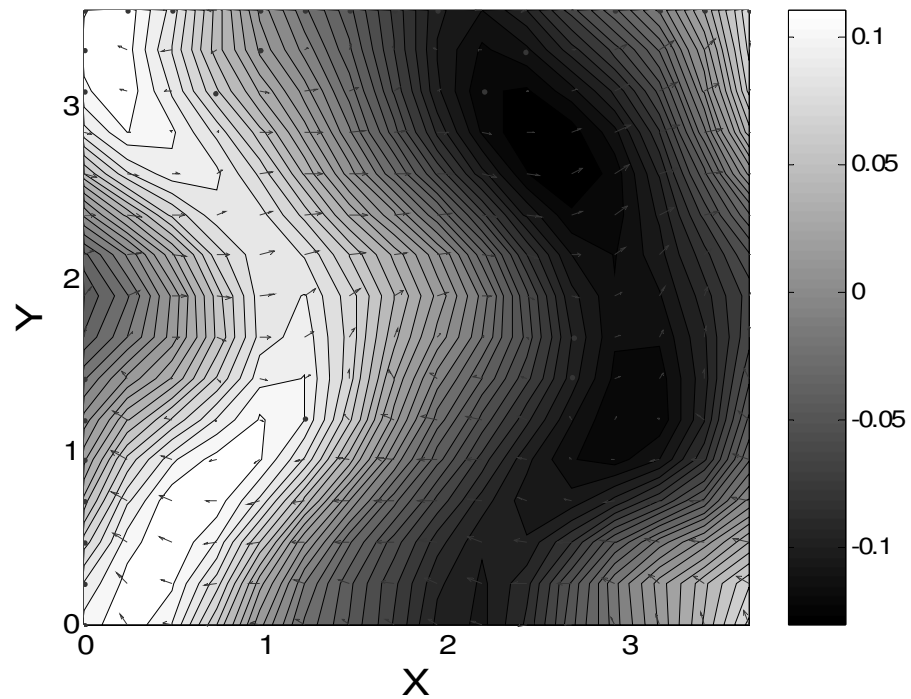


Figure 5.23 Velocity field and  $\Theta$  contours on  $xy$  plane at  $z=0$  and  $t=10.15$ .  $Ra=20000$ ,  $Pr=0.1$ ,  $Q=100$  and  $\chi=60^\circ$ . ( $\Gamma=1.95:1.90$ )

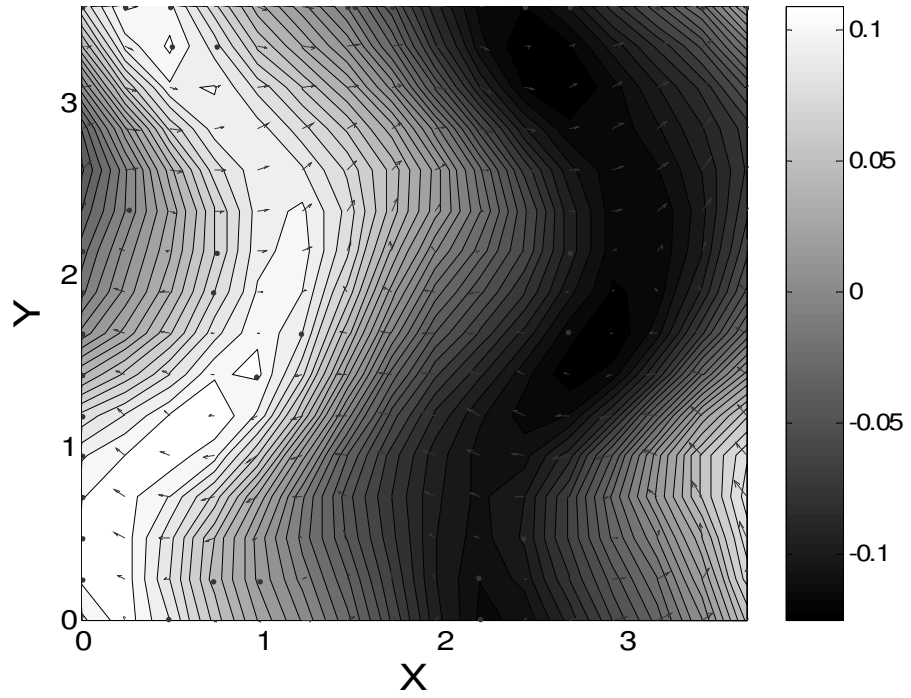


Figure 5.24 Velocity field and  $\Theta$  contours on  $xy$  plane at  $z=0$  and  $t=10.30$ .  $Ra=20000$ ,  $Pr=0.1$ ,  $Q=100$  and  $\chi=60^\circ$ . ( $\Gamma=1.95:1.90$ )

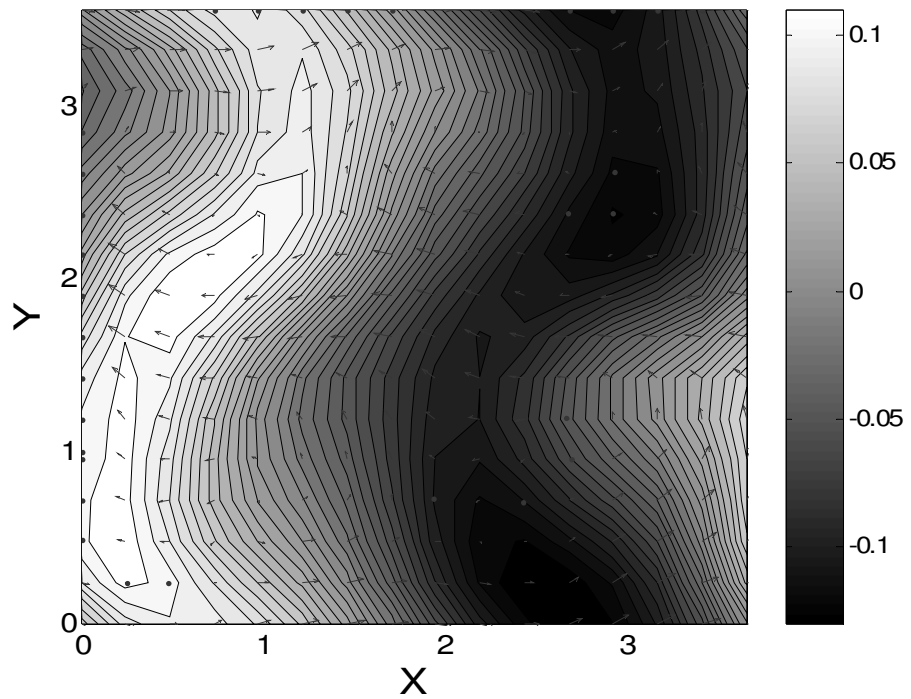


Figure 5.25 Velocity field and  $\Theta$  contours on  $xy$  plane at  $z=0$  and  $t=10.45$ .  $Ra=20000$ ,  $Pr=0.1$ ,  $Q=100$  and  $\chi=60^\circ$ . ( $\Gamma=1.95:1.90$ )

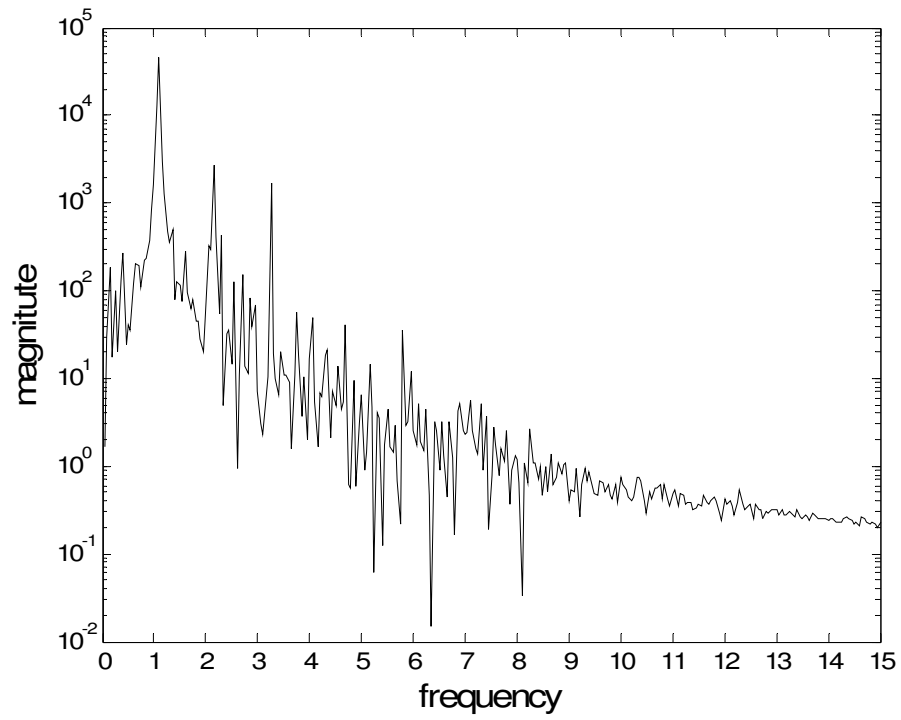


Figure 5.26 Frequency spectrum of  $u_x$  at  $x = 0.4875$ ,  $y = 0.475$  and  $z = -0.9109$  for  $Ra = 20000$ ,  $Pr = 0.1$ ,  $Q = 100$  and  $\chi = 60^\circ$ . ( $\Gamma = 1.95 : 1.90$ )

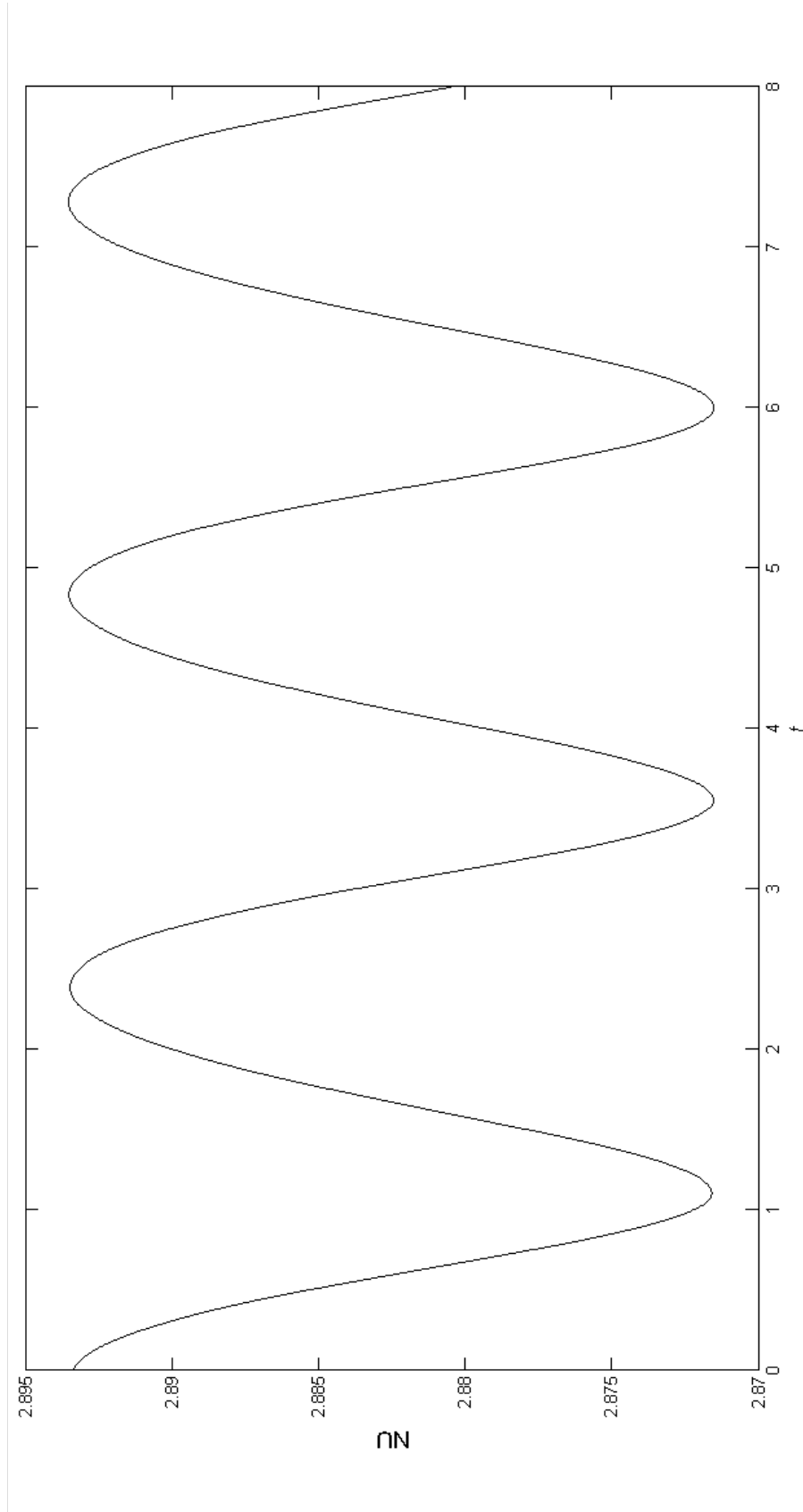


Figure 5.27 Nu vs.  $t$  at  $z=0$  for  $Ra=18000$ ,  $Pr=0.1$ ,  $Q=100$  and inc. angle is 30 degree.

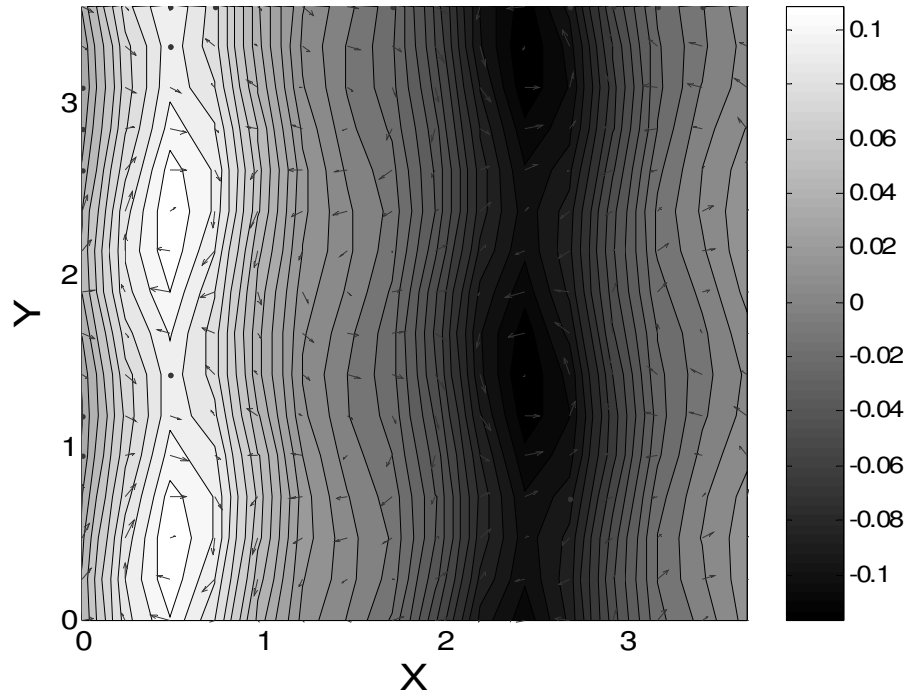


Figure 5.28 Velocity field and  $\Theta$  contours on  $xy$  plane at  $z=0$  and  $t=5$ .  $Ra=18000$ ,  $Pr=0.1$ ,  $Q=100$  and  $\chi=30^\circ$ . ( $\Gamma=1.95:1.90$ )

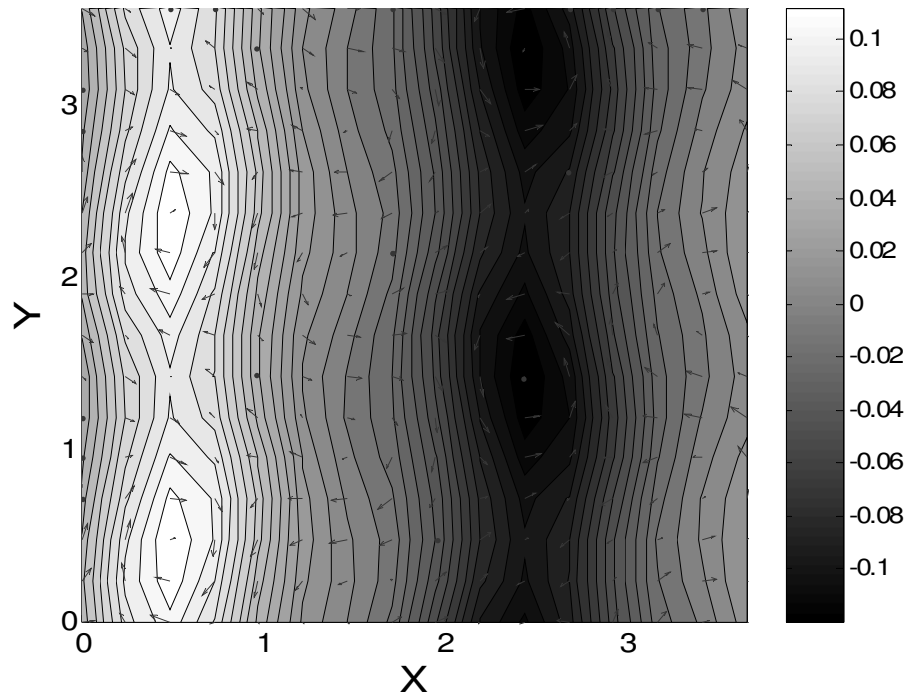


Figure 5.29 Velocity field and  $\Theta$  contours on  $xy$  plane at  $z=0$  and  $t=6$ .  $Ra=18000$ ,  $Pr=0.1$ ,  $Q=100$  and  $\chi=30^\circ$ . ( $\Gamma=1.95:1.90$ )

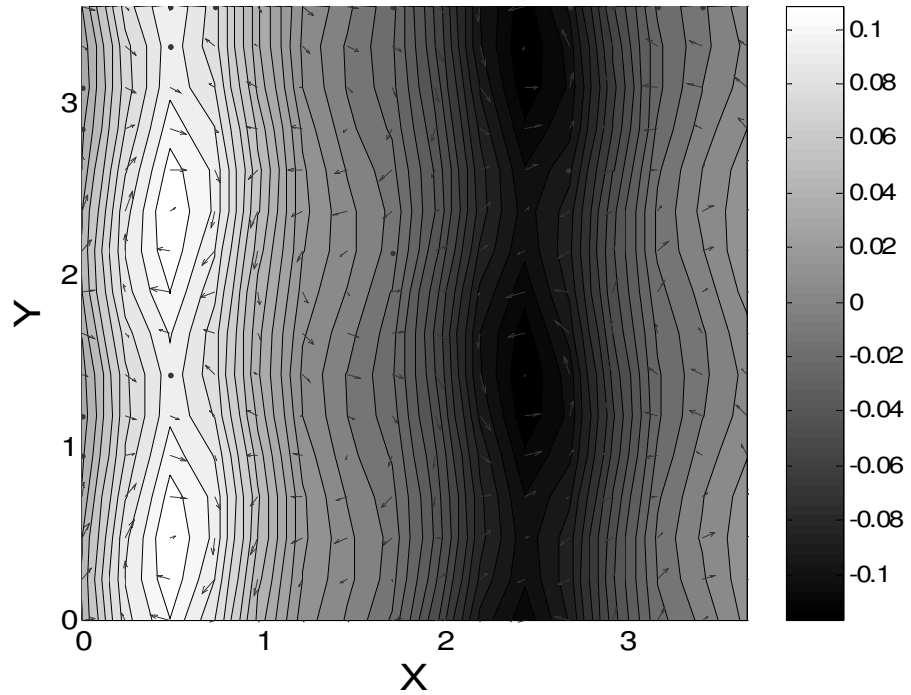


Figure 5.30 Velocity field and  $\Theta$  contours on  $xy$  plane at  $z = 0$  and  $t = 7$ .  $Ra = 18000$ ,  $Pr = 0.1$ ,  $Q = 100$  and  $\chi = 30^\circ$ . ( $\Gamma = 1.95 : 1.90$ )

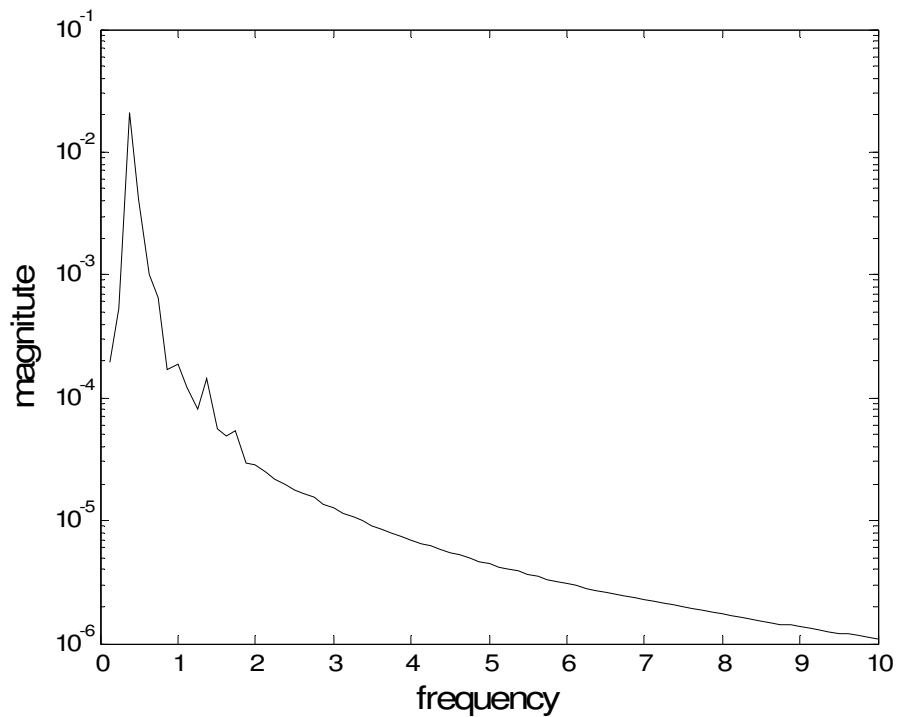


Figure 5.31 Frequency spectrum of  $\Theta$  at  $x = 0.4875$ ,  $y = 0.475$  and  $z = -0.9109$  for  $Ra = 18000$ ,  $Pr = 0.1$ ,  $Q = 100$  and  $\chi = 30^\circ$ . ( $\Gamma = 1.95 : 1.90$ )

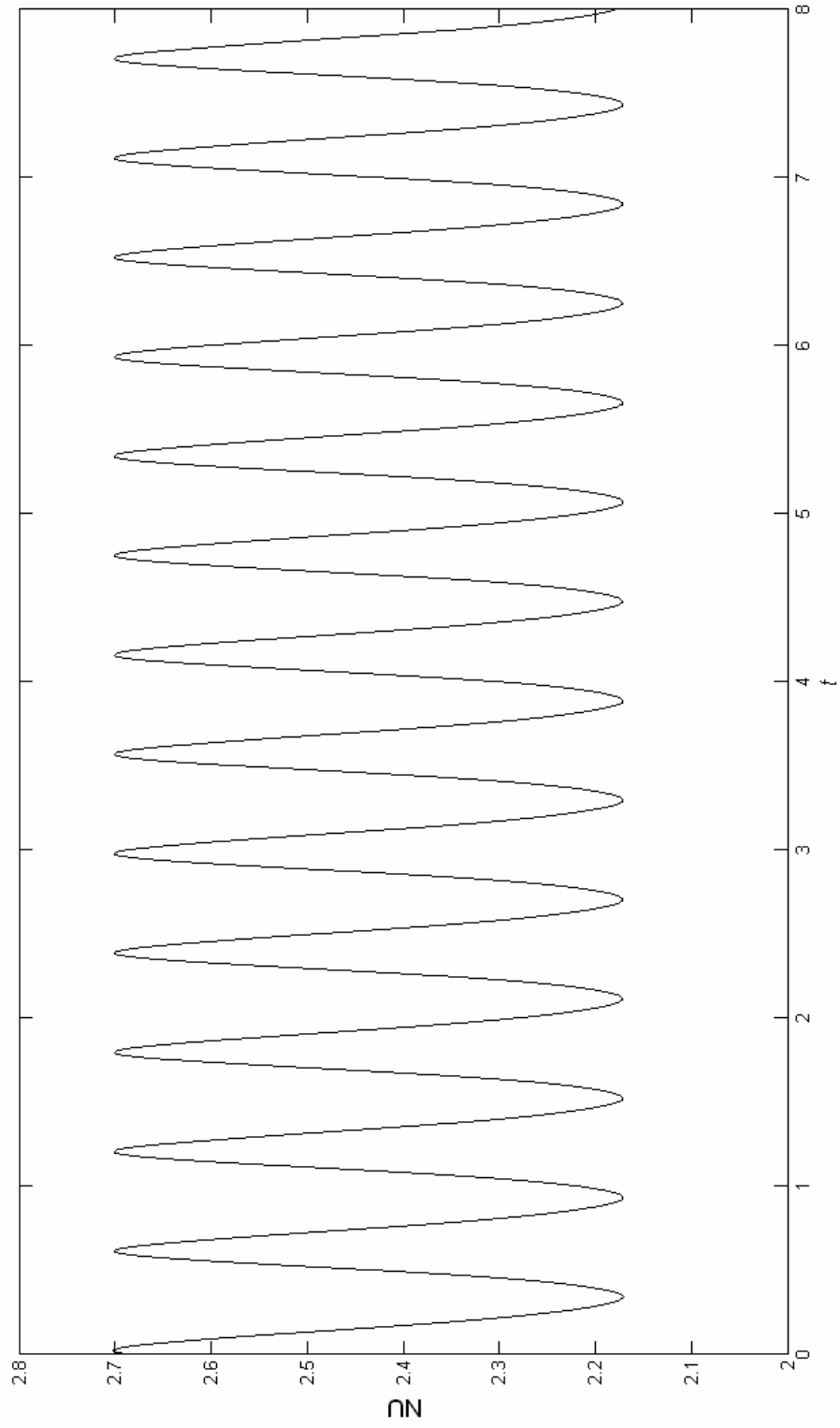


Figure 5.32 Nu vs.  $t$  at  $z=0$  for  $Ra=18000$ ,  $Pr=0.1$ ,  $Q=100$  and inc. angle is 30 degree with halved asp ratio.

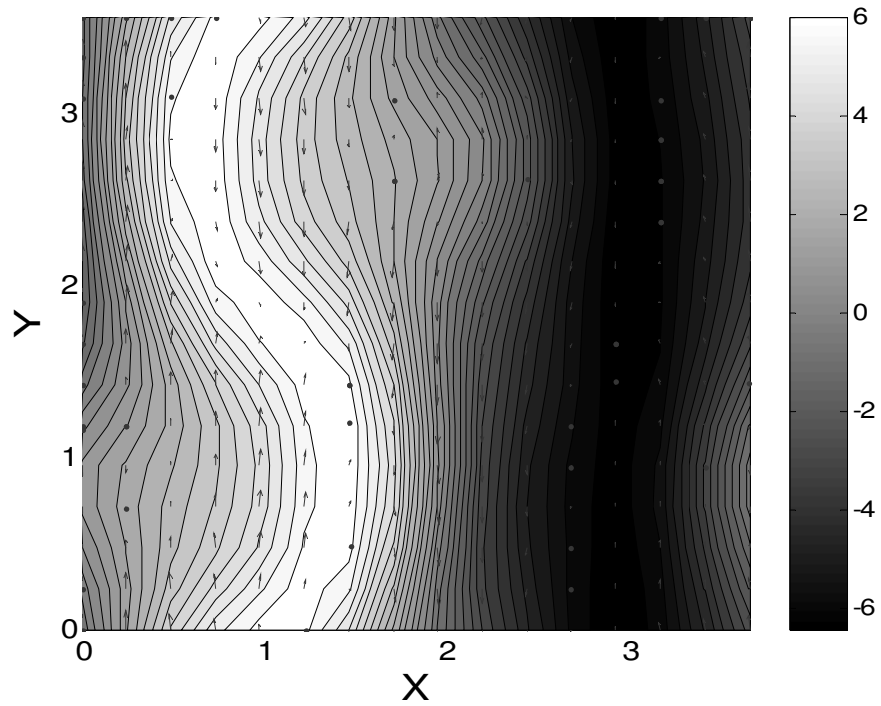


Figure 5.33 Velocity field and  $\Theta$  contours on  $xy$  plane at  $z=0$  and  $t=5.1$ .  $Ra=18000$ ,  $Pr=0.1$ ,  $Q=100$  and  $\chi=30^\circ$ . ( $\Gamma=0.975:0.95$ )

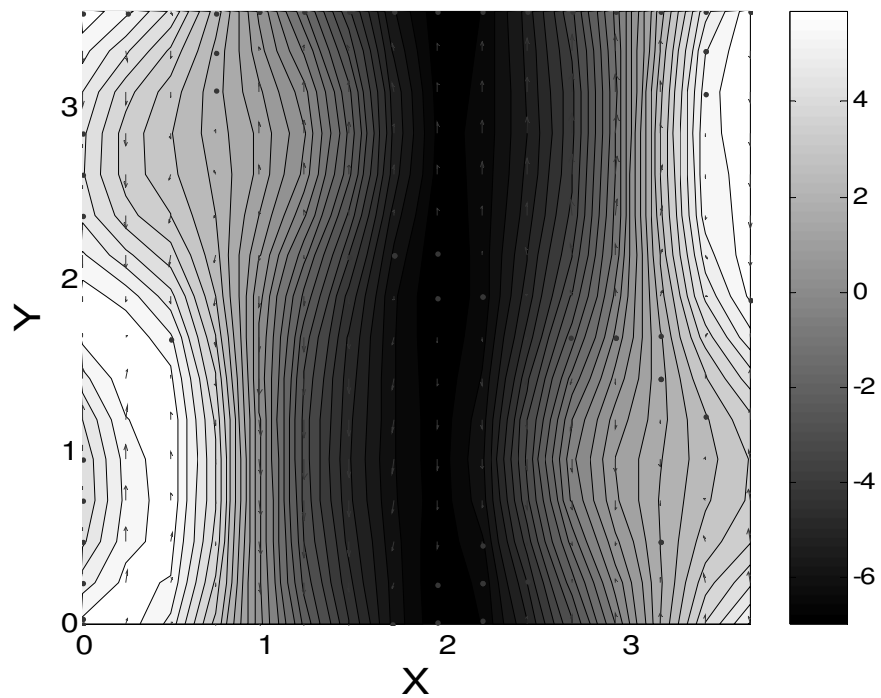


Figure 5.34 Velocity field and  $\Theta$  contours on  $xy$  plane at  $z=0$  and  $t=5.1725$ .  $Ra=18000$ ,  $Pr=0.1$ ,  $Q=100$  and  $\chi=30^\circ$ . ( $\Gamma=0.975:0.95$ )

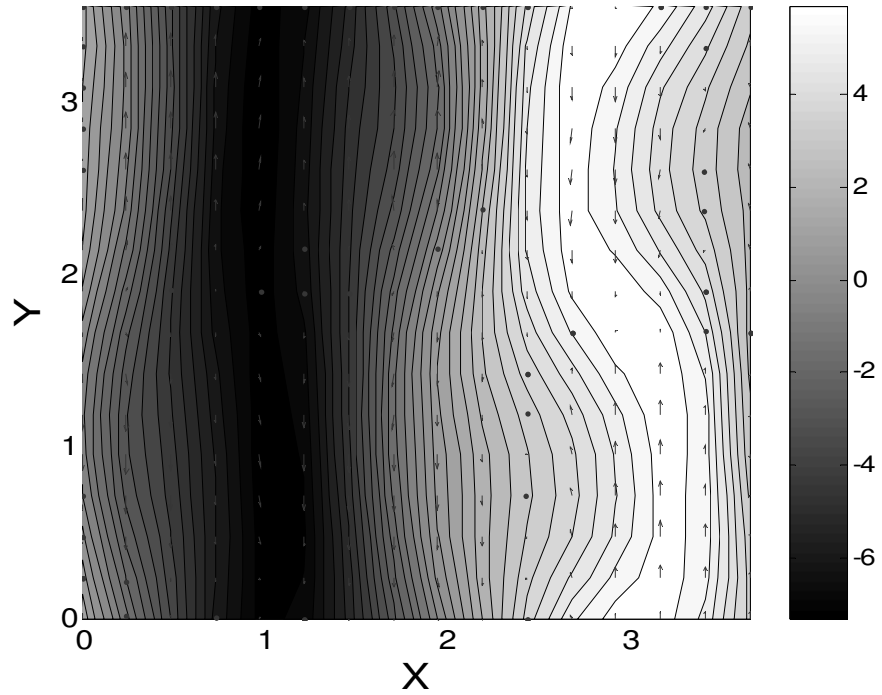


Figure 5.35 Velocity field and  $\Theta$  contours on  $xy$  plane at  $z=0$  and  $t=5.245$ .  $Ra=18000$ ,  $Pr=0.1$ ,  $Q=100$  and  $\chi=30^\circ$ . ( $\Gamma=0.975:0.95$ )

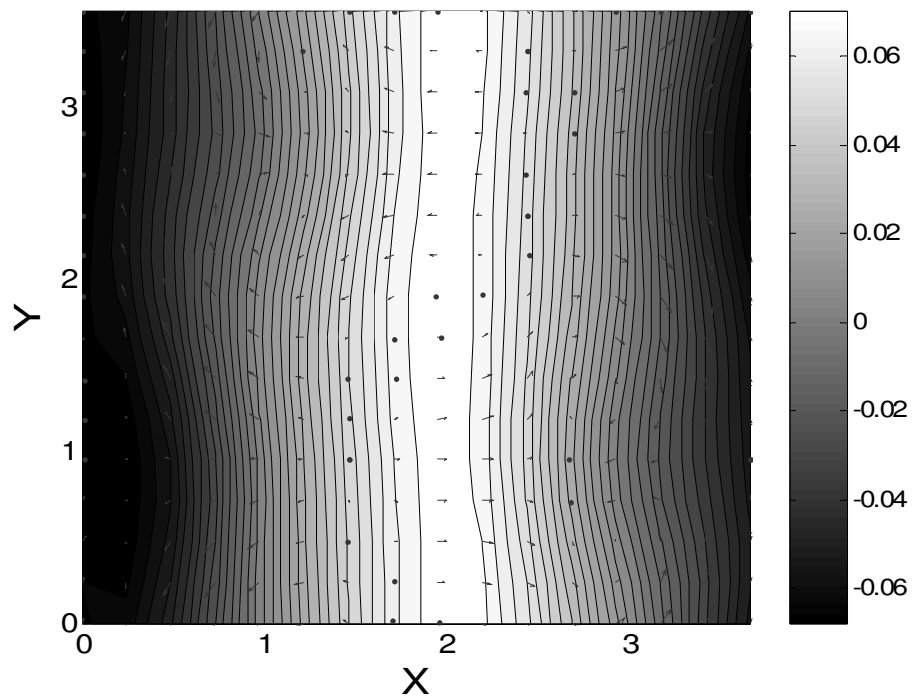


Figure 5.36 Velocity field and  $\Theta$  contours on  $xy$  plane at  $z=0$  and  $t=5.3175$ .  $Ra=18000$ ,  $Pr=0.1$ ,  $Q=100$  and  $\chi=30^\circ$ . ( $\Gamma=0.975:0.95$ )

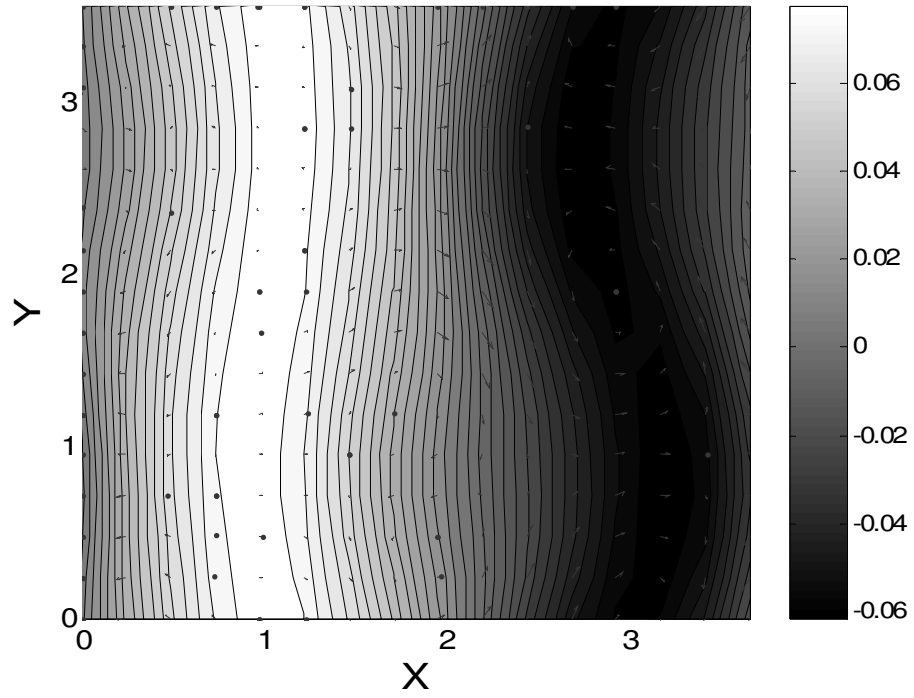


Figure 5.37 Velocity field and  $\Theta$  contours on  $xy$  plane at  $z=0$  and  $t=5.39$ .  $Ra=18000$ ,  $Pr=0.1$ ,  $Q=100$  and  $\chi=30^\circ$ . ( $\Gamma=0.975:0.95$ )

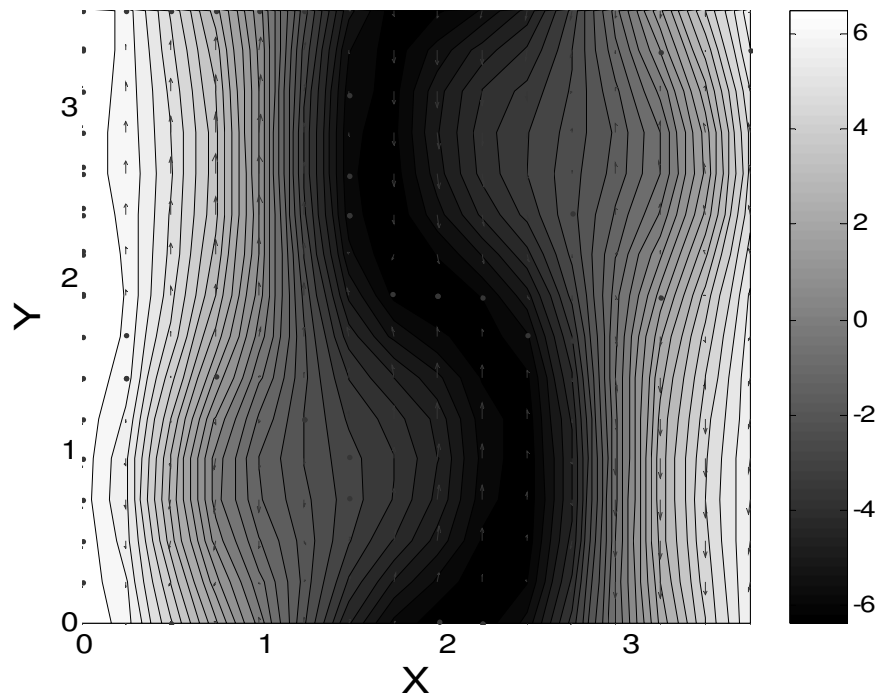


Figure 5.38 Velocity field and  $\Theta$  contours on  $xy$  plane at  $z=0$  and  $t=5.4625$ .  $Ra=18000$ ,  $Pr=0.1$ ,  $Q=100$  and  $\chi=30^\circ$ . ( $\Gamma=0.975:0.95$ )

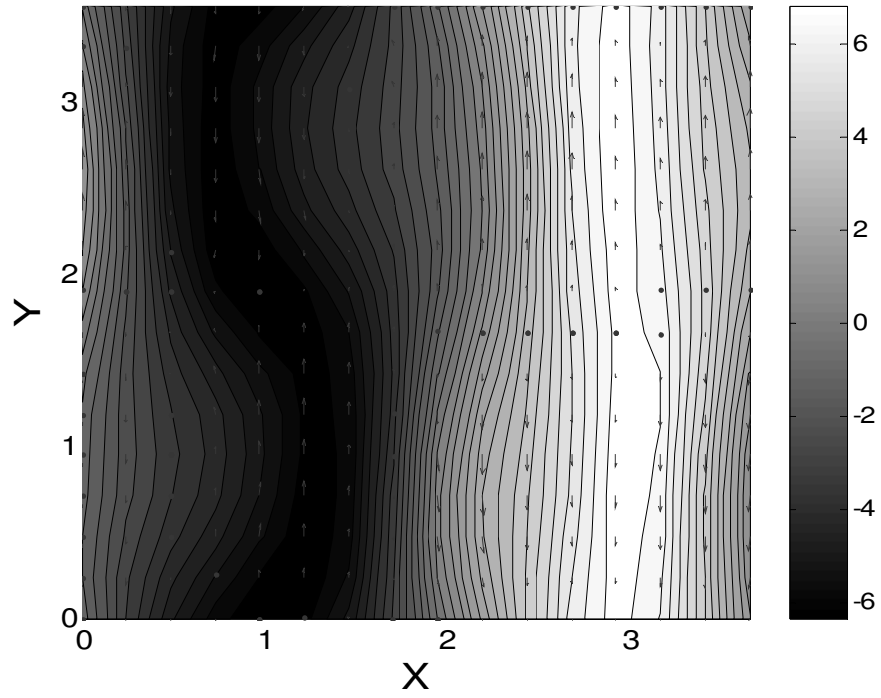


Figure 5.39 Velocity field and  $\Theta$  contours on  $xy$  plane at  $z=0$  and  $t=5.535$ .  $Ra=18000$ ,  $Pr=0.1$ ,  $Q=100$  and  $\chi=30^\circ$ . ( $\Gamma=0.975:0.95$ )

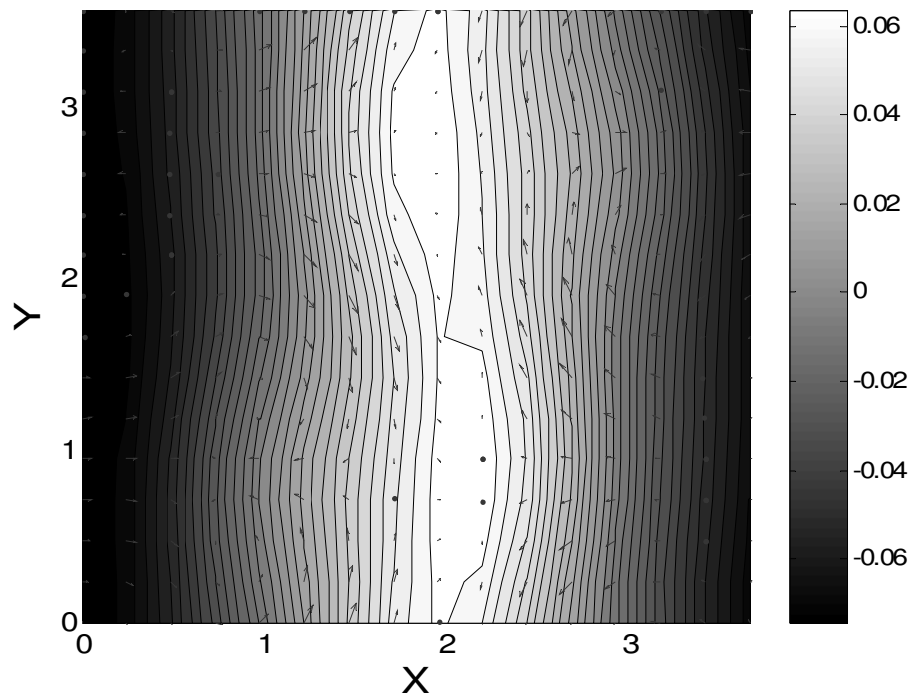


Figure 5.40 Velocity field and  $\Theta$  contours on  $xy$  plane at  $z=0$  and  $t=5.6075$ .  $Ra=18000$ ,  $Pr=0.1$ ,  $Q=100$  and  $\chi=30^\circ$ . ( $\Gamma=0.975:0.95$ )

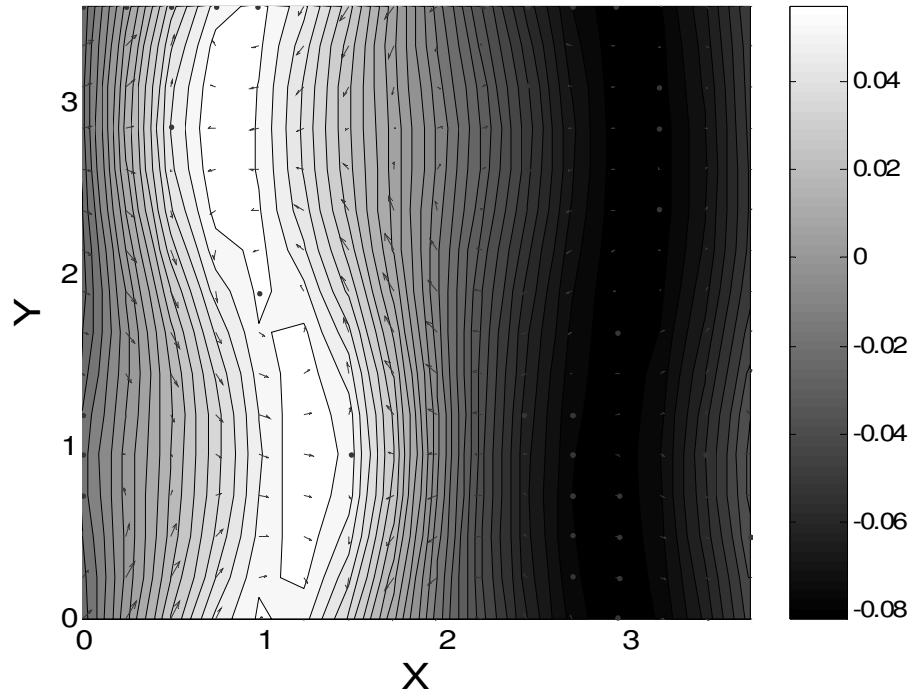


Figure 5.41 Velocity field and  $\Theta$  contours on  $xy$  plane at  $z = 0$  and  $t = 5.68$ .  $Ra = 18000$ ,  $Pr = 0.1$ ,  $Q = 100$  and  $\chi = 30^\circ$ . ( $\Gamma = 0.975 : 0.95$ )

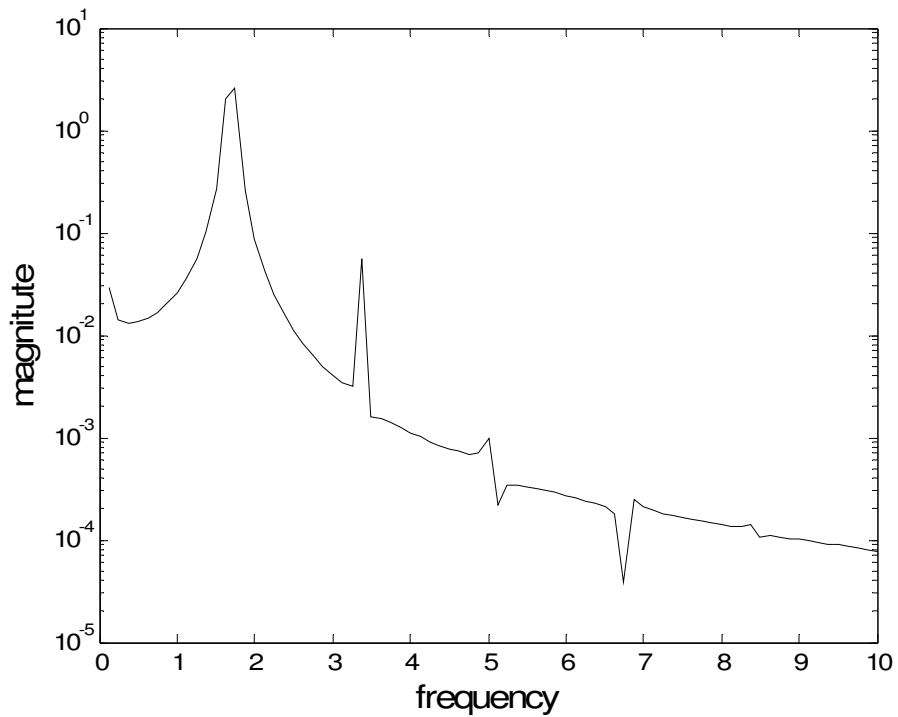


Figure 5.42 Frequency spectrum of  $\Theta$  at  $x = 0.24375$ ,  $y = 0.2375$  and  $z = -0.9109$  for  $Ra = 18000$ ,  $Pr = 0.1$ ,  $Q = 100$  and  $\chi = 30^\circ$ . ( $\Gamma = 0.975 : 0.95$ )

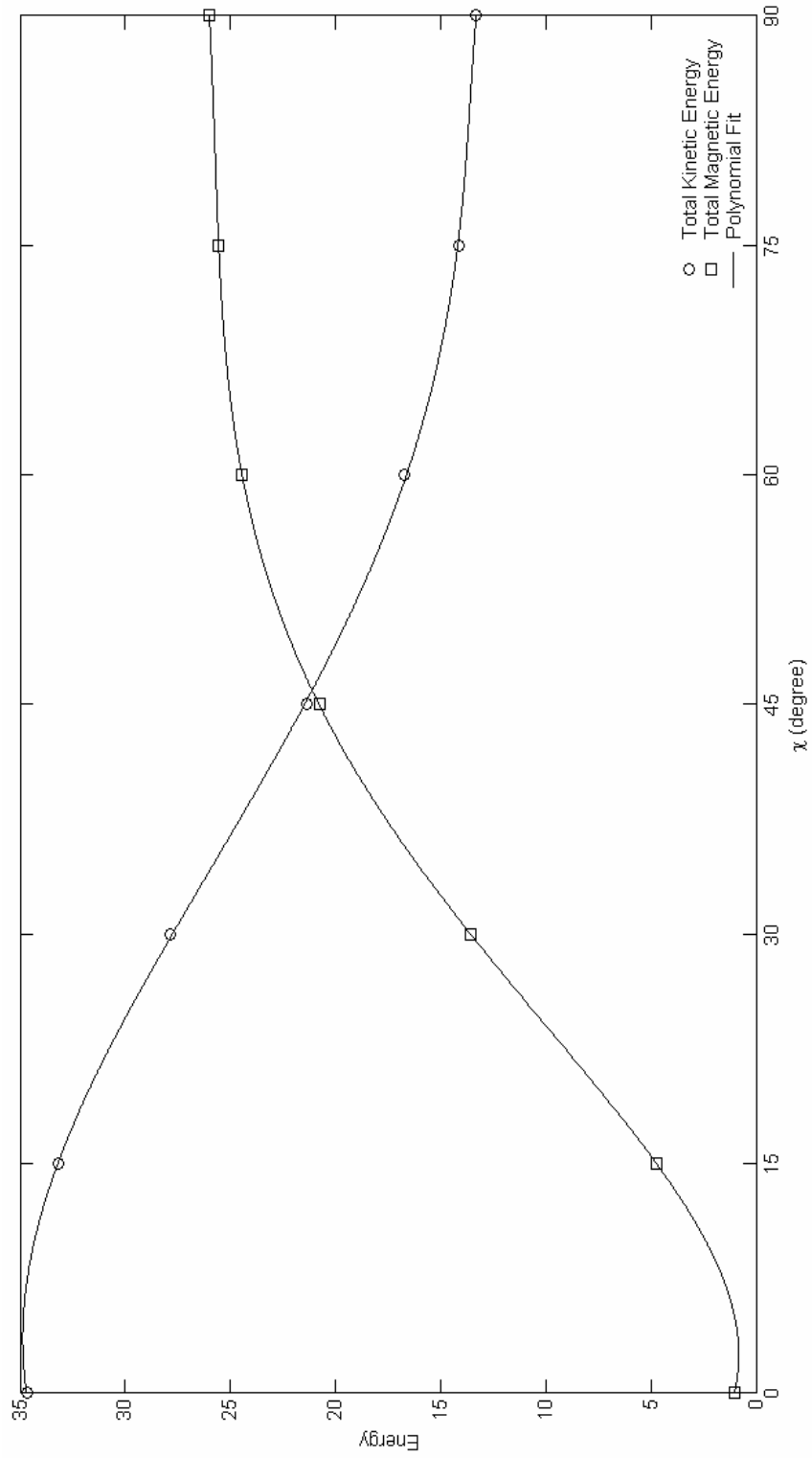


Figure 5.43 Total kinetic energy magnetic energy vs. incl angle for Ra=10000.

## CHAPTER 6

### A LOW DIMENSIONAL APPROXIMATION SCHEME TO MAGNETO-CONVECTION

In this part of the study, a low dimensional model is formulated for magneto-convection flow by adapting the pure Rayleigh-Benard convection to the case of magneto-convection. This approach permits a fast algorithm by constructing a basis for the pure convection flow then projecting it in to the magneto-convection flow.

Rayleigh-Benard convection is governed by dimensionless Boussinesq equations:

$$\nabla \cdot \mathbf{u} = 0 \quad (6.1)$$

$$\frac{\partial \mathbf{u}}{\partial t} = \mathbf{u} \times \boldsymbol{\omega} - \nabla \Pi + \text{Pr Ra}^* \Theta \mathbf{e}_z + \text{Pr} \nabla^2 \mathbf{u} \quad (6.2)$$

$$\frac{\partial \Theta}{\partial t} + (\mathbf{u} \cdot \nabla) \Theta = \mathbf{e}_z \cdot \frac{\mathbf{u}}{2} + \nabla^2 \Theta \quad (6.3)$$

All quantities have been made dimensionless by the normalization given in Chapter 2. The flow takes place in a periodic square box with an aspect ratio  $\Gamma = (s/2 : s/2)$ . The boundary conditions are imposed as the no-slip flow conditions:

$$\mathbf{u} = \Theta = 0 \quad \text{at } z = \mp 1 \quad (6.4)$$

in the vertical and periodic in the horizontal  $x$  and  $y$  directions.

The assumption of periodicity in the horizontal directions allows the use of Fourier series expansions of the dependent flow variables, similar to the (2.42) but this time for the case of pure convection:

$$\begin{bmatrix} \mathbf{u} \\ \Theta \\ \Pi \end{bmatrix} (x, y, z_i, t) = \sum_m \sum_n \begin{bmatrix} \hat{\mathbf{u}} \\ \hat{\Theta} \\ \hat{\Pi} \end{bmatrix} (m, n, z_i, t) \cdot \exp[i(m\zeta \cdot x + n\eta \cdot y)] \quad (6.5)$$

In the vertical direction, the velocity and temperature variables are expanded in terms of scaled Legendre-Lagrange interpolants as before:

$$\begin{bmatrix} \hat{\mathbf{u}} \\ \hat{\Theta} \end{bmatrix} (m, n, z_i, t) = \sum_{j=0}^{N_z} \begin{bmatrix} \bar{\mathbf{u}} \\ \bar{\Theta} \end{bmatrix} (m, n, z_j, t) \cdot \bar{h}_j(z_i) = \begin{bmatrix} \bar{\mathbf{u}} \\ \bar{\Theta} \end{bmatrix} (m, n, z_i, t) \cdot \bar{h}_i(z_i) \quad (6.6)$$

while the pressure is expanded in terms of Legendre polynomials

$$\hat{\Pi}(m, n, z_i, t) = \sum_{j=1}^{N_z-1} \bar{\Pi}(m, n, j, t) \cdot L_{j-1}(z_i) \quad (6.7)$$

## 6.1 Karhunen-Loeve Decomposition

KL procedure is used to generate an orthogonal basis from an ensemble of snapshots of realizations [30-32]. The elements of the basis set are the eigen functions of the integral equation,

$$\iiint_{\Omega} R(\mathbf{x}, \mathbf{x}') \Psi^q(\mathbf{x}') d\mathbf{x}' = \lambda_q \Psi^q(\mathbf{x}) \quad (6.8)$$

the kernel of which is the two-point correlation tensor

$$R_{ij}(\mathbf{x}, \mathbf{x}') = \langle v_i(\mathbf{x}, t) v_j(\mathbf{x}', t) \rangle \quad (6.9)$$

Here,  $v$  generically represent a physically relevant variable, such as temperature and/or velocity in the context of thermal convection. Generally, three indices are required to specify a basis set in three spatial dimensions.  $q$  represents these indices (see below).

The angle bracket denotes ensemble average. If the process is statistically stationary, ergodicity permits replacement of the ensemble average by an average over time. The existence of a countably infinite number of orthogonal eigenfunctions spanning the space follows from Hilbert-Schmidt theory. An element of the space can be expressed in the form of a modal decomposition

$$v(\mathbf{x}, t) = \sum_q a_q(t) \Psi^q(\mathbf{x}) \quad (6.10)$$

and the expansion coefficients are statistically orthogonal

$$\langle a_q(t) a_p^*(t) \rangle = \lambda_q \delta_{qp}. \quad (6.11)$$

For  $v$  representing the flow, each eigenvalue,  $\lambda_q$ , represents the mean energy of the flow projected on the direction  $\Psi^q$  in the function space.

Translational invariance of the flow in the horizontal directions implies that the eigenfunctions are in the form

$$\Psi_j^q(\mathbf{x}) \equiv \Psi_j(m, n, k; \mathbf{x}) = \Phi_j^q(z) \exp(2\pi i (m x/s_x + n y/s_y)) \quad (6.12)$$

where  $q = (m, n, k)$  and  $k$  is the vertical quantum number. The integral equation (6.8) to be solved is now reduces to

$$s_x s_y \int_{-1}^1 dz' \hat{R}_{ij}(m, n, z, z') \Phi_j(m, n, z') = \lambda(m, n) \Phi_i(m, n, z) \quad (6.13)$$

which is to be solved for  $\Phi_i(m,n,z)$  for each  $|m| < N_x/2$  and  $|n| < N_y/2$ . Further invariance of the system from (6.1) to (6.4) under rotational, when the convective box has square planform,  $s_x = s_y$ , and reflectional symmetries in the horizontal and reflectional symmetry in the vertical mid plane ( $z=0$ ) render the eigen solutions maximum 8-fold degenerate [33], i.e.:

Table 6.1 Symmetry group elements

	Symmetry Group Element	Action
Identity	I	$\{\mathbf{u}_x, \mathbf{u}_y, \mathbf{u}_z, \Theta, x, y, z\}$
Rotation by 90°	R	$\{-\mathbf{u}_y, \mathbf{u}_x, \mathbf{u}_z, \Theta, -y, x, z\}$
Rotation by 180°	R <sup>2</sup>	$\{-\mathbf{u}_x, -\mathbf{u}_y, \mathbf{u}_z, \Theta, -x, -y, z\}$
Rotation by 270°	R <sup>3</sup>	$\{\mathbf{u}_y, -\mathbf{u}_x, \mathbf{u}_z, \Theta, y, -x, z\}$
Reflection in $x$	F	$\{-\mathbf{u}_x, \mathbf{u}_y, \mathbf{u}_z, \Theta, -x, y, z\}$
Diagonal Flip	FR	$\{\mathbf{u}_y, \mathbf{u}_x, \mathbf{u}_z, \Theta, y, x, z\}$
Reflection in $y$	FR <sup>2</sup>	$\{\mathbf{u}_x, -\mathbf{u}_y, \mathbf{u}_z, \Theta, x, -y, z\}$
Diagonal Flip	FR <sup>3</sup>	$\{-\mathbf{u}_y, -\mathbf{u}_x, \mathbf{u}_z, \Theta, -y, -x, z\}$
Vertical Flip	Z	$\{\mathbf{u}_x, \mathbf{u}_y, -\mathbf{u}_z, -\Theta, x, y, -z\}$

Eigen-values of (6.13) would have symmetries:

$$\lambda_{(\pm m, \pm n, k)} = \lambda_{(\pm m, \mp n, k)} = \lambda_{(\pm m, \pm n, k)} = \lambda_{(\pm m, \mp n, k)} \quad (6.14)$$

and either odd or even in  $z=0$ . In fact, the action of the symmetry group is;

$$\{I, R, R^2, R^3, F, FR, FR^2, FR^3\} \times \{I, Z\} \quad (6.15)$$

with 16 elements expands the existing database 16-fold and lead to a sharper and representative set of KL modes.

This set of KL modes may be paired in such a way to provide a convenient parametric representation of the flow database in the terms of real and physical flowlets,  $v^q$ ,

$$v(\mathbf{x}, t) = \sum_q v^q = \sum_q \{a_q(t) \Psi^q(\mathbf{x}) + a_{q^*}(t) \Psi^{q^*}(\mathbf{x})\} \quad (6.16)$$

where the summation index  $q$  runs through the conjugate pairs of the K-L modes  $\{q, q^*\}$  defined by

$$q = (m, n, k) \quad \text{and} \quad q^* = (-m, -n, k) \quad (6.17)$$

where

$$\Psi^{q^*} = (\Psi^q)^* \quad \text{and} \quad a_{q^*} = a_q^* \quad (6.18)$$

with

$$a_q = (\Psi^q, v)_x = \int \sum_i v_i(\mathbf{x}, t) (\Psi_i^q(\mathbf{x}))^* d\mathbf{x} \quad (6.19)$$

Here,  $( )^*$  represents complex conjugation.

## 6.2 Adaptation on Magneto-convection Model

Consider a database generated by numerically solving the governing equations from (6.1) to (6.4), using the numerical scheme described earlier for a particular set of the parameter values, say,  $\{\text{Ra}^0, \text{Pr}^0, s_x = s_y = s \text{ and } \Gamma = s/2 : s/2\}$ , so selected to result in a database with sufficiently rich dynamical content. The resulting flow database  $v = [\mathbf{u}_x, \mathbf{u}_y, \mathbf{u}_z](\mathbf{x}, t)$  and  $v = [\Theta](\mathbf{x}, t)$  can then separately be

used to construct mechanical  $\mathbf{U}_j(m,n,k;z)$ ,  $j=1,2,3$  and thermal  $\theta(m,n,k;z)$  KL basis which are in turn used to parameterise the database and to study the underlying dynamics of the flow.

$$\mathbf{u}_j(\mathbf{x},t) = \sum_q a_q(t) \mathbf{U}_j^q(z) \exp(2\pi i (m x/s_x + n y/s_y)), \quad (6.20)$$

$$\Theta(\mathbf{x},t) = \sum_q c_q(t) \theta^q(z) \exp(2\pi i (m x/s_x + n y/s_y)), \quad (6.21)$$

where mechanical and thermal KL basis are defined with Fourier coefficients as:

$$\mathbf{U}^q(z; x, y) = \mathbf{U}_j^q(z) \exp(2\pi i (m x/s_x + n y/s_y)) \quad (6.22)$$

$$\theta^q(z; x, y) = \theta_j^q(z) \exp(2\pi i (m x/s_x + n y/s_y)) \quad (6.23)$$

These computed KL modes, as they satisfy spatial constraints and carry independent features of the flow, form a convenient basis for reducing governing equations to a relatively low dimensional dynamical system via Galerkin projection. Further, their divergence-free nature causes the pressure gradient term to drop during projection.

In particular, a low dimensional approximation to thermal convection in the presence of a magnetic field under quasi-steady approximation is of interest. The dimensionless form of the governing equations for magneto-convection is given from (2.28) to (2.32).

Beside with boundary conditions for velocity  $\mathbf{u} = (\mathbf{u}_x, \mathbf{u}_y, \mathbf{u}_z)$  and temperature fields  $\Theta$  given by (6.4), perfectly

conducting boundary conditions are assumed for induced magnetic field,  $\mathbf{b} = (\mathbf{b}_x, \mathbf{b}_y, \mathbf{b}_z)$ , such that (2.37) is valid for this case.

The quasi-steady link (2.32) between the velocity field and the induced magnetic field facilitates the use of KL basis, (6.22) and (6.23), in order to construct a relatively low dimensional KL based dynamical model of the governing equations from (2.28) to (2.32). First, an approximation of the flow

$$\mathbf{u} \approx \mathbf{u}_S = \sum_{q \in S} a_q(t) \mathbf{U}^q(z; x, y), \quad (6.24)$$

$$\Theta \approx \Theta_S = \sum_{q \in S} c_q(t) \Theta^q(z; x, y), \quad (6.25)$$

in terms of a set of KL modes selected based on their physical importance is to be obtained. Here,  $S$  denotes index set of the selected KL modes. This approximation is, in turn, forced to satisfy the governing momentum (6.2), and heat (6.3) equations using Galerkin projection;

$$\left( \mathbf{U}^q(z; x, y), R_{\mathbf{u}}(\mathbf{u}_S, \Theta_S) \right)_x = 0, \quad (6.26)$$

$$\left( \Theta^q(z; x, y), R_{\Theta}(\mathbf{u}_S, \Theta_S) \right)_x = 0, \quad (6.27)$$

resulting in a dynamical system

$$\frac{d}{dt} a_q = F U_q(a_i, c_j), \quad (6.28)$$

$$\frac{d}{dt} c_q = F T_q(a_i, c_j), \quad (6.29)$$

for  $q, i, j \in S$ , where

$$F U_q \equiv \text{Ra}^* \text{Pr} P U(q; i) c_i + \text{Pr} D U(q; i) a_i + N U(q; i, j) a_i a_j + Q^* \text{Pr} M U(q; i) a_i, \quad (6.30)$$

$$F T_q \equiv P T(q; i) a_i + D T(q; i) c_i + N T(q; i, j) a_i c_j. \quad (6.31)$$

Using the index vector representations  $q = (q_1, q_2, k_q)$ ,  $i = (i_1, i_2, k_i)$  and  $j = (j_1, j_2, k_j)$ , the coefficients are

$$PU(q; i) = \left( \mathbf{U}^q(z; x, y), \Theta^i(z; x, y) \mathbf{e}_z \right)_x, \quad (6.32)$$

$$PT(q; i) = \left( \Theta^q(z; x, y), \frac{1}{2} \mathbf{U}_3^i(z; x, y) \right)_x, \quad (6.33)$$

$$DU(q; i) = \left( \mathbf{U}^q(z; x, y), \nabla^2 \mathbf{U}^i(z; x, y) \right)_x, \quad (6.34)$$

$$DT(q; i) = \left( \Theta^q(z; x, y), \nabla^2 \Theta^i(z; x, y) \right)_x, \quad (6.35)$$

$$MU(q; i) = \left( \mathbf{U}^q(z; x, y), \left[ (\cos \chi \mathbf{e}_y + \sin \chi \mathbf{e}_z) \cdot \nabla \right] \mathbf{B}^i(z; x, y) \right)_x \quad (6.36)$$

for  $q_1 = i_1$ ,  $q_2 = i_2$ ,

$$NU(q; i, j) = \left( \mathbf{U}^q, \mathbf{U}^i \times (\nabla \times \mathbf{U}^j) \right)_x, \quad (6.37)$$

$$NT(q; i, j) = \left( \Theta^q, -(\mathbf{U}^i \cdot \nabla) \Theta^j \right)_x \quad (6.38)$$

for  $q_1 = i_1 + j_1$ ,  $q_2 = i_2 + j_2$ . In the computation of the coefficients  $NU(q; i, j)$  the satisfaction of the triad relation

$$NU(q; i, j) + NU(-i; -q, j) + NU(-j; i, -q) = 0, \quad (6.39)$$

where  $-q = (-q_1, -q_2, k_q)$ , is verified.

Computation of the Lorentz forcing term in (6.36)  $\left( \mathbf{U}^i(z; x, y), \left[ (\cos \chi \mathbf{e}_y + \sin \chi \mathbf{e}_z) \cdot \nabla \right] \mathbf{B}^i(z; x, y) \right)_x$  requires special attention. The substitution of the KL expansion (6.24) into the quasi-steady approximation (2.32) yields the differential equation

$$\left[ \frac{d^2}{dz^2} - \gamma^2 (m^2 + n^2) \right] \mathbf{B}^q(z) = - \left( i n \gamma \cos \chi + \sin \chi \frac{d}{dz} \right) \mathbf{U}^q(z) \quad (6.40)$$

to be solved for each  $q = (m, n, k)$  subject to

$$\frac{d\mathbf{B}_x^q}{dz} = \frac{d\mathbf{B}_y^q}{dz} = \mathbf{B}_z^q = 0 \quad \text{at } z = \mp 1. \quad (6.41)$$

Note that  $\mathbf{B}^q(z; x, y) = \mathbf{B}^q(z) \exp(2\pi i(m x/s + n y/s))$  and  $\gamma = 2\pi/s$ . The apparent non-uniqueness in  $\mathbf{B}_x(z)$  and  $\mathbf{B}_y(z)$  for  $m = n = 0$  can be removed by adding an artificial and convenient additional constraint.

### 6.3 KL Description of Motion

In this section, an application of low dimensional model is tested by creating a database for the steady roll motion in the case of pure Rayleigh Benard convection. Data is generated with the parameters  $Ra = 30000$ ,  $Pr = 0.1$  and  $\Delta t = 5 \cdot 10^{-4}$  in a square box planform for which the aspect ratio is selected as  $\Gamma = 2:2$  by using a  $24 \times 24 \times 24$  grid. In this case, flow motion is in such a complicated form that all physical variables have highly considerable fluctuations over time. Therefore, a number of data samples are taken from dataset for the modal decomposition with KL to provide characteristic modes of physical variables. Two-point correlation tensor (6.9) is obtained at a time,  $t$  and the eigenfunctions,  $\mathbf{U}_j^q(z)$  and  $\Theta_j^q(z)$  is calculated for a set of  $q = (m, n, k)$  by (6.13). By the help of the quasi steady link between velocity and induced magnetic field (6.40), the characteristic vectors for the induced magnetic field  $\mathbf{B}_j^q(z)$  are computed subjected with the boundary conditions (6.41) for the set  $q = (m, n, k)$ . A couple of eigenfunctions for the velocity and temperature fields and of the corresponding induced magnetic field is shown in Figures 6.1 to 6.6. It should be noted that the eigenfunctions follow certain

symmetries such as oddness and evenness around the mid-plane  $z=0$  as well as the quantum number  $k$  increases, in general, zero crossings increase indicating that more structures are embedded in the eigenfunctions for higher  $k$ .

Table 6.2 Mechanical KL modes for the first five.

Index	$q$	Degeneracy	%
1	(1,0,1)	4	7.9
2	(1,1,1)	4	3.4
3	(1,0,2)	4	2.7
4	(1,0,3)	4	2.0
5	(1,1,2)	4	1.0

Table 6.3 Thermal KL modes for the first five.

Index	$q$	Degeneracy	%
1	(0,0,1)	1	53
2	(1,0,1)	4	7.2
3	(1,1,1)	4	2.2
4	(2,0,1)	4	0.24
5	(2,1,1)	8	0.16

The most energetic five mechanical modes involve only 17 percent of energy in summation (Table 6.2). Thermal modes are different in order and first five of them cover 62 percent (Table 6.3). The eigenvectors are arranged according to how

much they contribute into the motion which is basically related with corresponding eigenvalues. The ratio of an eigenvalue to the summation of them gives the information on energy.

Summation values of energy percentages for first five modes show some other modes should also be covered to resemble a good approximation to the dynamical picture of the motion for the parameter  $Ra^0 = 30000$ . Figures 6.1 to 6.6 give an idea for vertical variation of eigenvectors. Here, degeneracy implies the number of the elements in a symmetry group, for example, eigenvalues and the eigenvectors of the symmetrical modes  $(1,0,1), (0,1,1), (-1,0,1)$  and  $(0,-1,1)$  all belong to the same family.

In order to construct the low dimensional dynamical system (6.30)-(6.31), modes are selected first based on the following criteria;

$$S = \left\{ (m,n,k) \mid \sqrt{m^2 + n^2} \leq 3 \text{ and } 1 \leq k \leq 4 \right\} . \quad (6.42)$$

The idea is to include minimal number of modes in as complete symmetry representation as possible as well as to exploit the homogeneity in the horizontal direction. The energy criteria can not be directly used in selecting the modes to be included in  $S$ , since the optimality of the KL decomposition is only valid at the parameter values that the modes are generated.

The resulting dynamical system is integrated in time to test the effect of the vertical magnetic field in qualitative

manner. The results are shown in Figures 6.7 to 6.10. The numbering of the modes in the KL spectrum is based on the Table 6.4. These preliminary results show that the dynamical system constructed using KL basis simulates the behaviour observed in the full simulation to a qualitative extent. This is encouraging to pursue further tests and improvements on the construction of this system.

Table 6.4 The indexing of the KL modes as it appears in the KL spectrum plots in Figures 6.7 to 6.8.

Index	$q$	Index	$q$
1	(1,0,1)	11	(1,1,2)
2	(0,1,1)	12	(1,-1,2)
3	(1,0,2)	13	(1,1,3)
4	(0,1,2)	14	(1,-1,3)
5	(1,0,3)	15	(1,1,4)
6	(0,1,3)	16	(1,-1,4)
7	(0,1,4)	17	(0,0,1)
8	(1,0,4)	18	(0,0,2)
9	(1,1,1)	19	(0,0,3)
10	(1,-1,1)	20	(0,0,4)

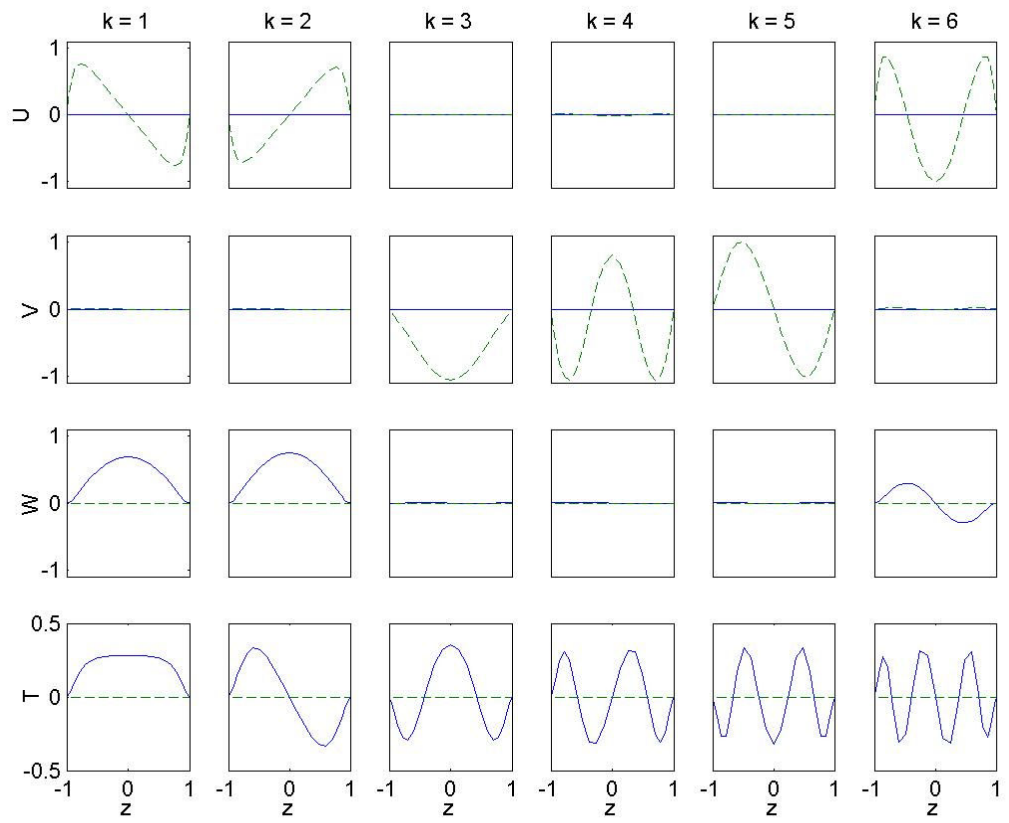


Figure 6.1 The vertical profiles of KL modes ( $m = 1, n = 0, k$ ) with real (solid) and imaginary (dash) parts.

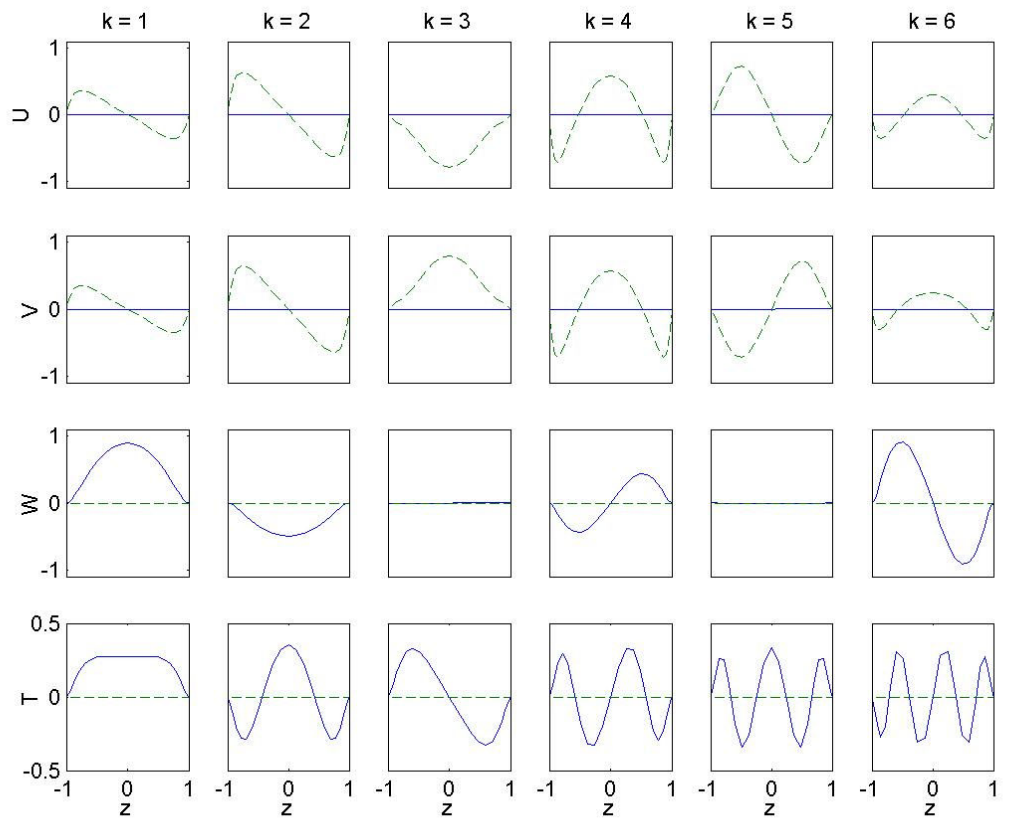


Figure 6.2 The vertical profiles of KL modes ( $m=1, n=1, k$ ) with real (solid) and imaginary (dash) parts.

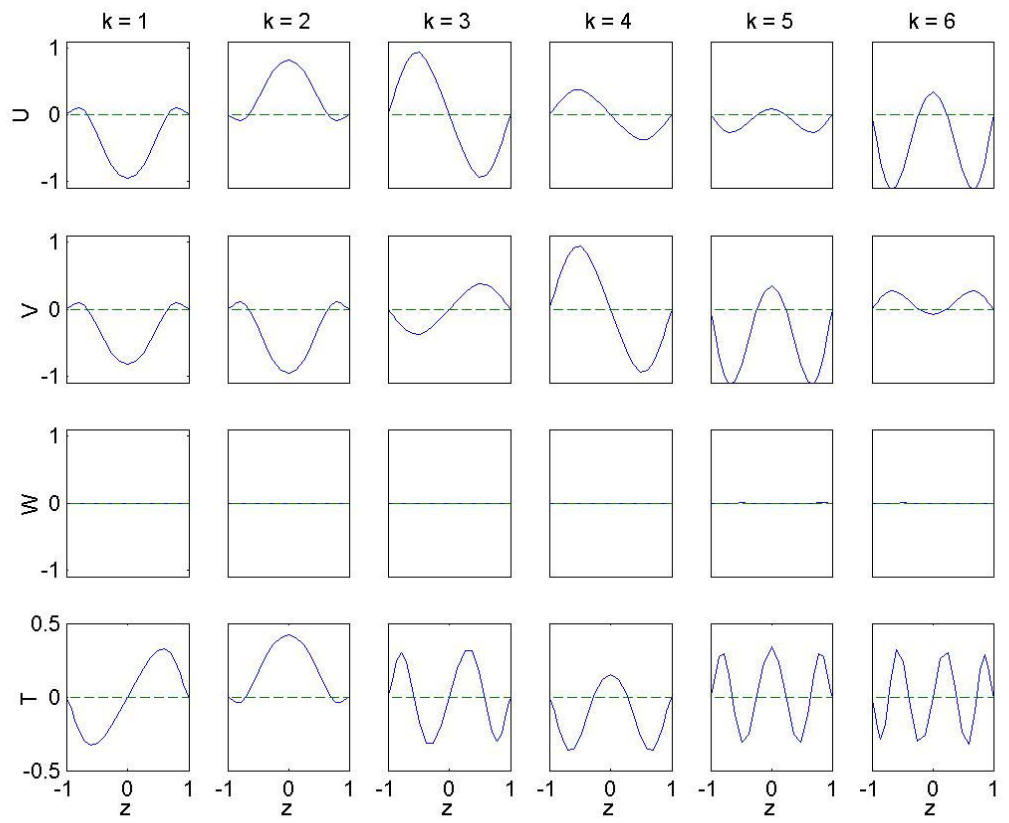


Figure 6.3 The vertical profiles of KL modes ( $m = 0$ ,  $n = 0$ ,  $k$ ) with real (solid) and imaginary (dash) parts.

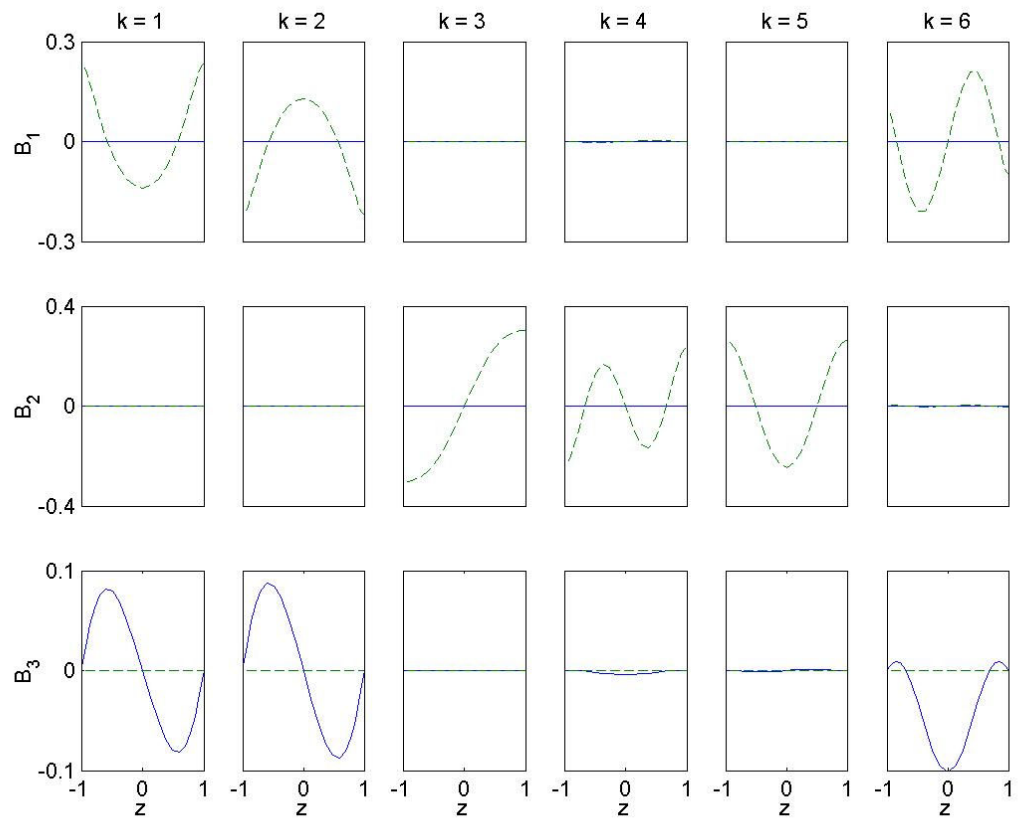


Figure 6.4 The vertical profiles of the induced magnetic field components corresponding to KL modes ( $m=1$ ,  $n=0$ ,  $k$ ) with real (solid) and imaginary (dash) parts.

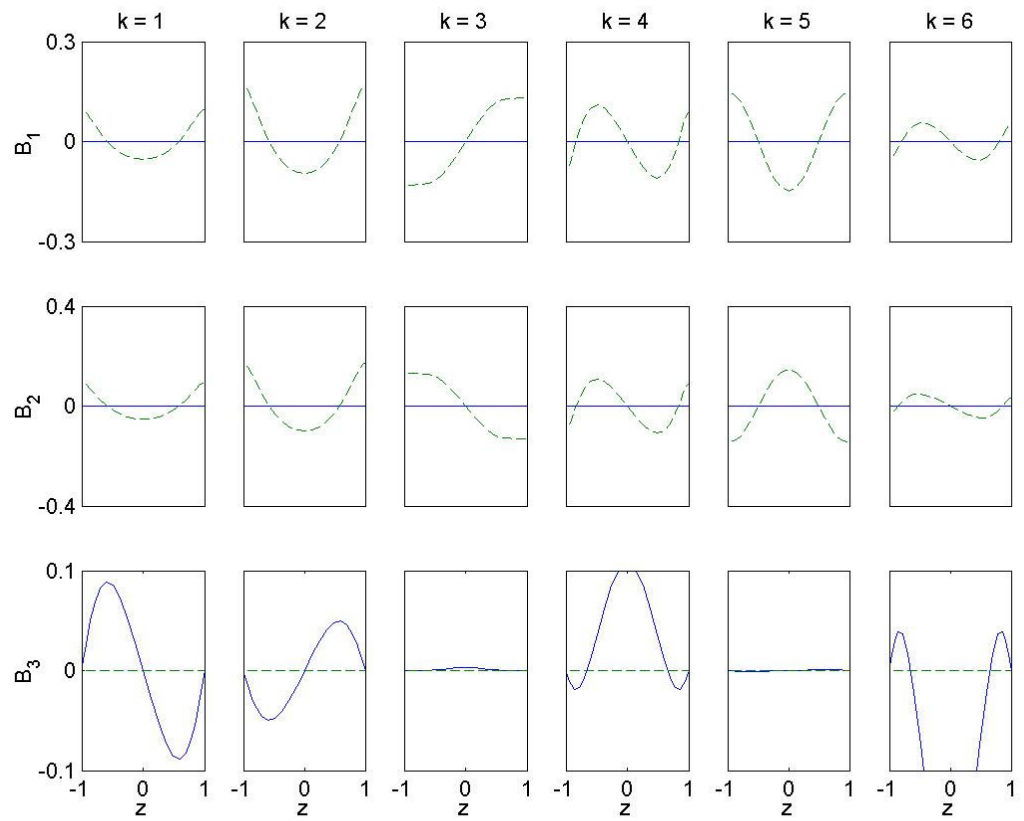


Figure 6.5 The vertical profiles of the induced magnetic field components corresponding to KL modes ( $m=1, n=1, k$ ) with real (solid) and imaginary (dash) parts.

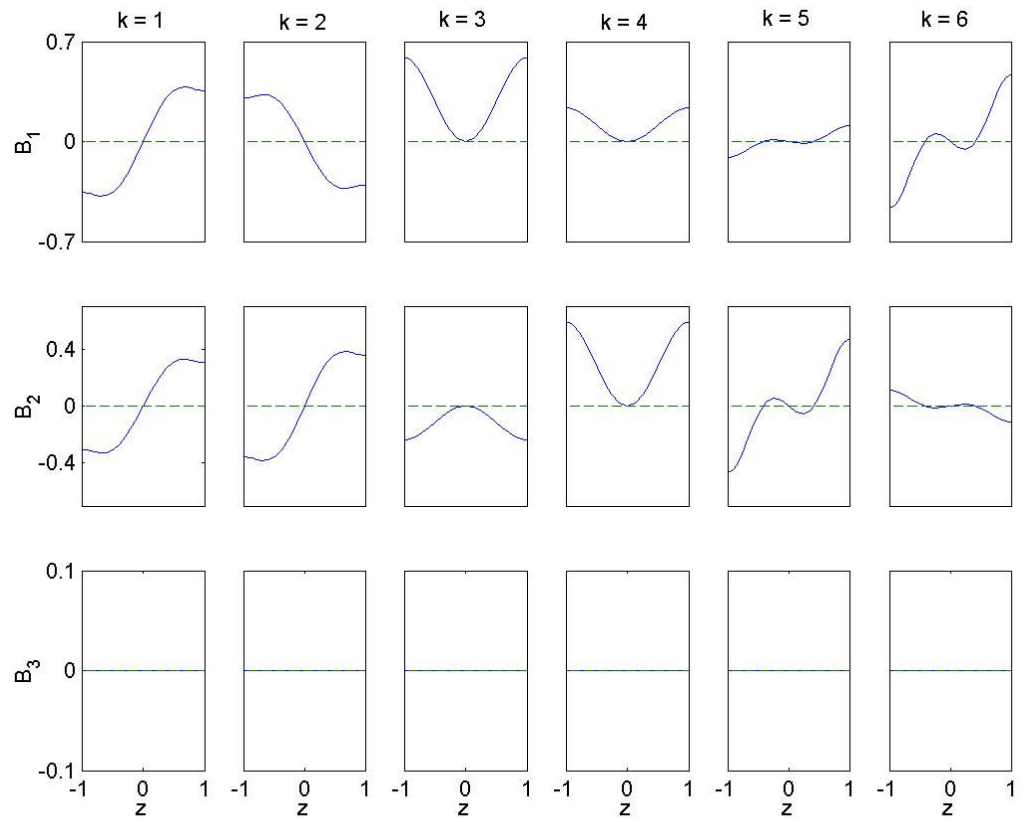


Figure 6.6 The vertical profiles of the induced magnetic field components corresponding to KL modes ( $m=0, n=0, k$ ) with real (solid) and imaginary (dash) parts.

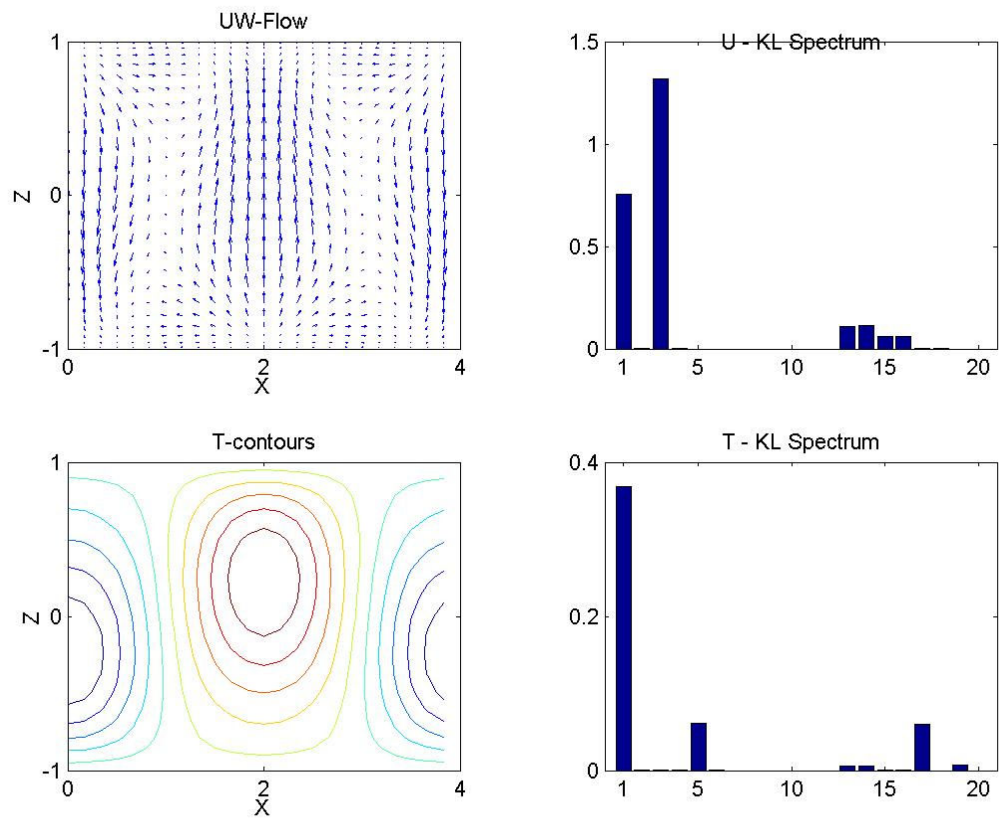


Figure 6.7 The rolling motion at  $Ra=10000$ ,  $Pr=0.1$  obtained by integrating the dynamical system in time. The KL spectrum shows those modes (Table 6.3) excited in this steady regime.

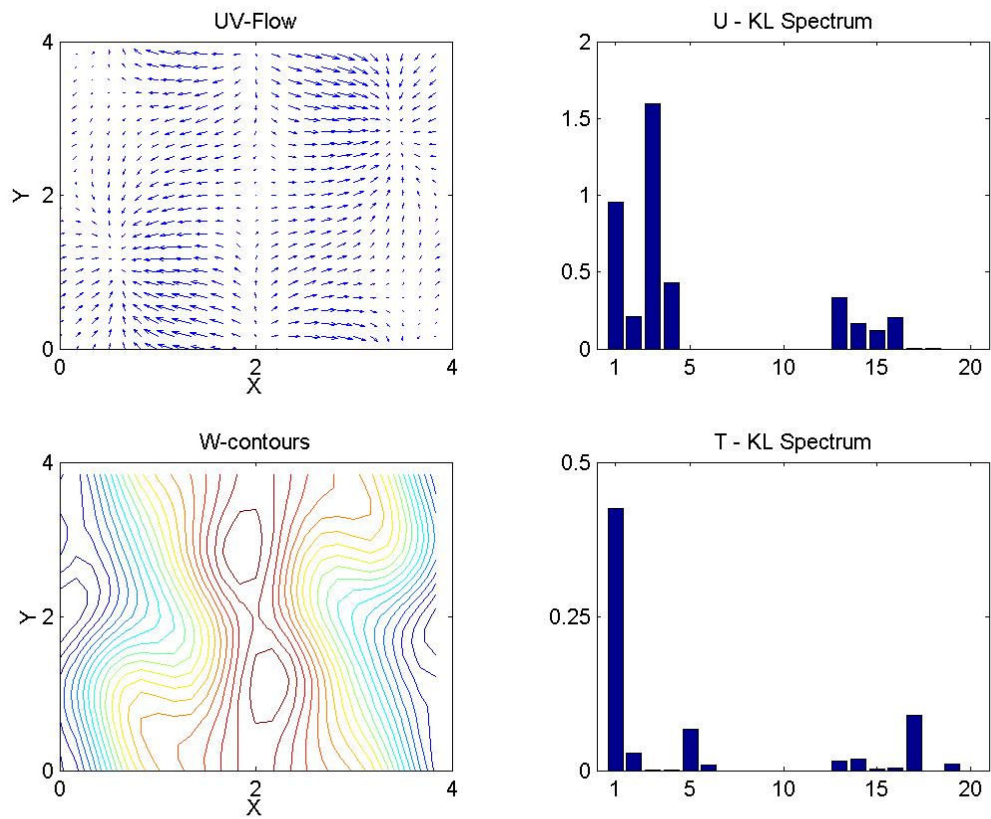


Figure 6.8 The periodic motion at  $Ra=14000$ ,  $Pr=0.1$  obtained by integrating the dynamical system in time. The KL spectrum shows that relatively more modes (Table 6.3) are excited in this periodic regime.

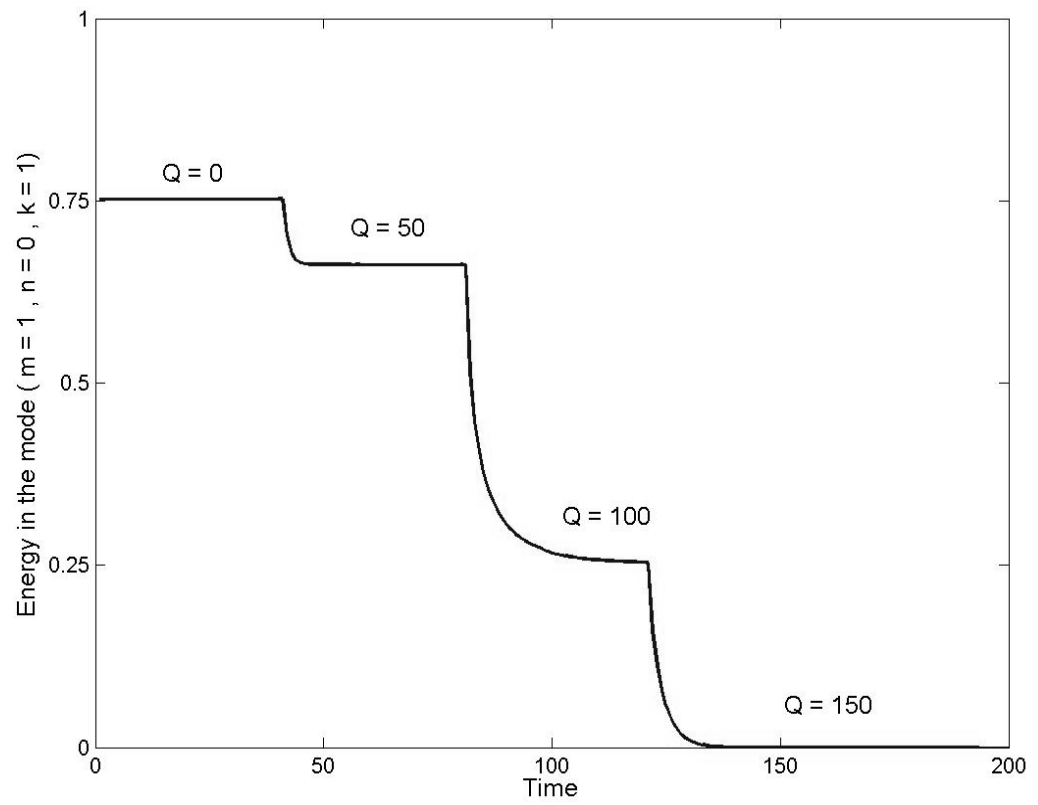


Figure 6.9 The steady roll motion in Figure 6.7 cascades to zero as the strength of the vertical magnetic field applied is increased.

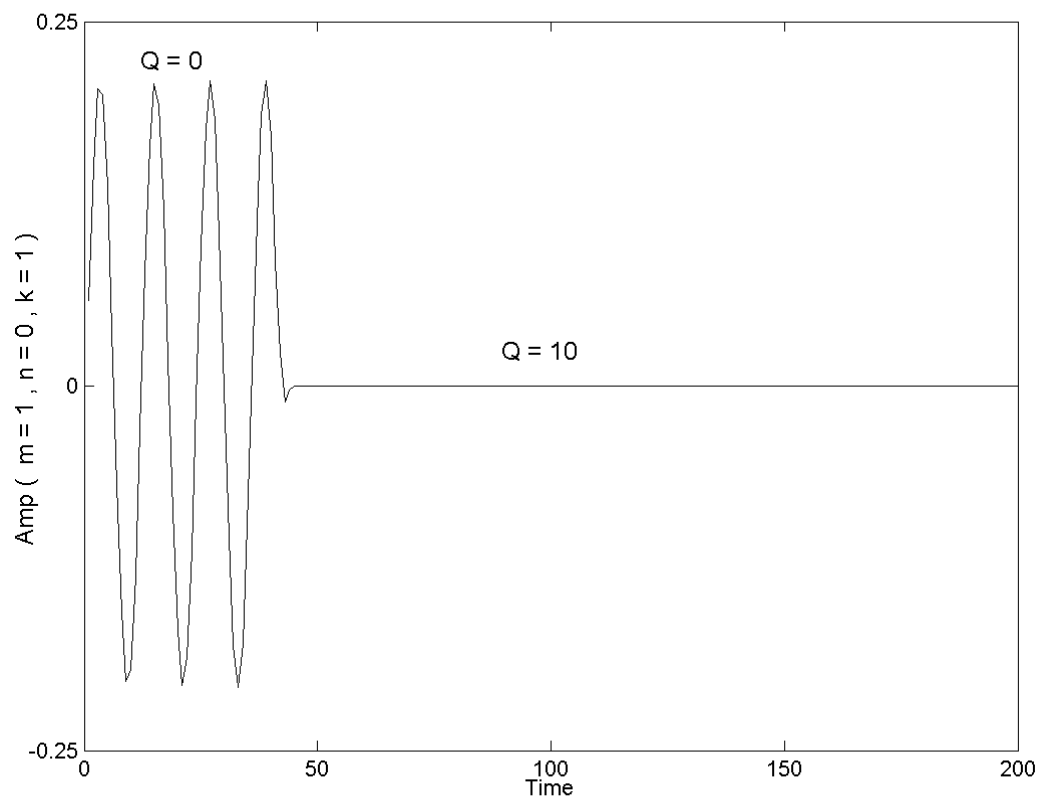


Figure 6.10 The periodic motion in Figure 6.8 is inhibited by the application of the vertical magnetic field as shown in the time evolution of a particular expansion coefficient.

## CHAPTER 7

### CONCLUSION

In this work, we have been able to extend a spectral-element based numerical scheme to simulate natural thermal convection in electrically conducting low Prandtl fluids (i.e. liquid metals) in an infinite layer under the influence of an externally applied inclined magnetic field and to test successfully in comparison to many results in literature with the main outcome that an external magnetic field in any direction within the plane of the roll axis leads to suppression of various instabilities of the convective fluid by means of the Lorentz force, especially, in the case of the large magnetic diffusion or small  $Pm$ , in other words, magnetic field stabilizes thermal convection.

As a second point, heat transfer efficiency is increased momentarily by the magnetic field. Simulations for a number of  $(Ra, Q)$  pairs converged to steady rolls in the  $xz$  plane. Induced magnetic field in the horizontal  $y$  direction and currents in the horizontal plane vanish for the case of the 2D stationary roll motion whose roll axis is parallel to the  $y$  direction. Usual roll motion interacts with the external magnetic field in the  $z$  direction via Lorentz forces. These forces acts against the motion, reorganize the classical Benard cells and get them denser which results in an increase in the number of cells. This increased horizontal

wave number or increased vertical motion causes rapid or efficient heat transport.

The horizontal component of the external magnetic field in the  $y$  direction, parallel to roll axis, results in the least inhibition of the flow kinetic energy but the most support on the flow stability. A delayed onset of convection is caused by the vertical component of the external magnetic field whereas horizontal component retards the onset of oscillations much more effectively. Restrictions such as Hartmann breaking or viscous damping due to sidewalls does not exist in this study.

On the other hand, dimensions of the horizontal layer should be chosen larger to allow more degrees of freedom for the convective motions to select appropriate spatial scales naturally. Even though the computed results are in satisfactory agreement with existing results in literature ([12],[13],[20] and [21]), we expect much more comparable results due to less spatial constraints when a larger aspect ratio is selected. Due to inadequate computational resources, the analysis of the model in a range of large  $Ra$  and  $Q$  values is limited to small aspect ratio. Critical values of  $Ra$  and  $Q$  at the onset of the supercritical regime are found to be within 4% of the values presented in [13] as shown in Table 3. It should be noted that the present computation is performed at a fixed value of the aspect ratio corresponding to the wave number  $\zeta = 3.2$ . Small aspect ratio as well as the quadratic extrapolation used on data in the steady regime may be contributing to this end. Correlation analysis in the experimental study of Aurnou and Olson [21] gives a

relationship between  $Nu$  and  $(Ra, Q)$  as  $Nu \approx \sqrt{Ra/Q}$ . This relationship is also observed to be valid for the results computed here in the interval given by the experimental study.

As to the spectral element method implemented, the accuracy of the spectral element method increases exponentially with increasing polynomial degree (resolution) used as long as the underlying solutions are smooth. In the spectral element method, one can locally increase the polynomial degree within the element, called p-refinement or the number of elements, called h-refinement in the under-resolved regions. For a given resolution, spectral element method is much more accurate than the conventional finite differences or finite element method, and that the accuracy increases faster with the increasing resolution. Besides this, the spectral element method offers flexibility in the choices of the geometry of the computational domain. Hence, this work may be carried over to the curvilinear geometries.

In chapter 6, a low dimensional description to magneto-convection model is attempted using KL modes of pure convection model. The results of this preliminary analysis show that amplitudes of some KL modes vanish due to the suppressive effects of the external magnetic field. A detailed analysis is to be performed towards associating the physical picture attached to each KL mode and the damping and reorganizing effects of the magnetic field. In the unsteady regime, the KL modes initiating the low amplitude oscillations are to be identified and examined under the varying inclination angles.

## REFERENCES

- [1] S. Chandrasekhar. Hydrodynamic and Hydromagnetic Instability. Oxford, Clarendon Press, 1961
- [2] G. Veronis. Cellular convection with finite amplitude in a rotating fluid, *J. Fluid Mech.*, 5:401–435, 1959
- [3] B. Lehnert. *Quart. Appl. Math.*, 12, 321, 1955
- [4] R.B. Deissler. Magneto-fluid dynamic turbulence with a uniform imposed magnetic field, *Phys. Fluids*, 6, 1250, 1963
- [5] J.A. Nestlerode, J.L. Lumley. Initial response of the spectrum of isotropic turbulence to the sudden application of a strong magnetic field, *Phys. Fluids*, 6, 1260, 1963
- [6] Y. Nakagawa, An experiment on the inhibition of thermal convection by a magnetic field, *Proc. R. Soc. Lond. A*, 175, 417-419, 1955
- [7] E.A. Spiegel, Convection in stars II. Special effects. *Ann. Rev. Astron. Astrophys.* , 10, 261-304, 1972
- [8] N.O. Weiss, Magnetic fields and convection, *Adv. Chem. Phys.*, 32, 101-107, 1975
- [9] M.R.E. Proctor, N.O. Weiss, Magneto-convection, *Rep. Prog. Phys.*, 45, 1317-1379, 1982
- [10] F. H. Busse, Nonlinear interaction of magnetic field and convection, *J. Fluid Mech.*, 71, part 1, 193-206, 1975
- [11] F. H. Busse, R. M. Clever. Stability of convection rolls in the presence of a vertical magnetic field. *Phys. Fluids*, 25(6):931–935, 1982

- [12] R.M. Clever, F.H. Busse. Nonlinear oscillatory convection in the presence of a vertical magnetic field. *J. Fluid Mech.*, 201:507–523, 1988
- [13] F. H. Busse, R. M. Clever. Finite amplitude convection in the presence of an inclined magnetic field. *Eur. J. Mech., B/Fluids*, 9, n° 3:225–238, 1990
- [14] F. H. Busse, R. M. Clever. Three-dimensional convection in the presence of strong vertical magnetic fields. *Eur. J. Mech., B/Fluids*, 15, n° 1:1–15, 1996
- [15] U. Burr, U. Müller. Rayleigh-Benard convection in liquid metal layers under the influence of a vertical magnetic field. *Phys. Fluids*, 13(11):3247–3257, 2001
- [16] U. Burr, U. Müller. Rayleigh-Benard convection in liquid metal layers under the influence of a horizontal magnetic field. *J. Fluid Mech.*, 453:345–369, 2002
- [17] A. T. Patera. A spectral element method for fluid dynamics: laminar flow in a channel expansion. *J. Comp. Phys.*, 54:468–488, 1984
- [18] M. R. Schumack, W. W. Schultz, J. P. Boyd. Spectral method solution of the Stokes equations on nonstaggered grids. *J. Comp. Phys.*, 94:30–58, 1991
- [19] L. Guessous. A Pseudo-spectral numerical scheme for the simulation of steady and oscillating wall-bounded flows. *Numerical Heat Transfer.*, 45(Part B):135–157, 2004
- [20] R. Mössner, M. Ulrich. A numerical investigation of three dimensional magneto-convection in rectangular cavities. *Int. J. Heat Mass Transfer.*, 42:1111–1121, 1999

- [21] J. M. Aurnou, P. L. Olson. Experiments on Rayleigh Benard convection, magneto-convection and rotating magneto-convection in liquid gallium. *J.Fluid Mech.*, 430:283–307, 2001
- [22] S.A. Orszag, L.C. Kells, Transition to turbulence in plane Poiseuille flow and plane Couette flow. *J. Fluid Mech.*, 96, 159, 1980
- [23] J. P. Boyd, Chebyshev and Fourier spectral methods. New York: Springer-Verlag, 1989
- [24] G. Freud, Oxford, New York, Pergamon Press [1971]
- [25] R. Peyret, Spectral methods for incompressible flow, NewYork: Springer , 2000
- [26] C. Canuto, M. Hussaini, A. Quarteroni, T. Zang, Spectral Methods in Fluid Dynamics. New York: Springer-Verlag, 1988
- [27] D.B. Haidvogel, T. Zang, The accurate solution of Poisson's equation by expansion, *J. Comp. Phys.*, 30, 167-180, 1979
- [28] G. Grötzbach, Spatial resolution requirements for direct numerical simulation of Rayleigh-Benard Convection, *J. Comp. Phys.*, 49, 241-264, 1983
- [29] R.M. Clever, F.H. Busse, Transition to time-dependent convection, *J. Fluid Mech.*, 65,625–645, 1974
- [30] L. Sirovich, Turbulence and the dynamics of coherent structures, Parts 1-3, *Q. Appl. Math.*, 45, 561, 1987
- [31] J.L. Lumley, `Stochastic Tools in Turbulence', Academic Press, New York, 1970

[32] G. Berkooz, P. Holmes, J.L. Lumley, The Proper Orthogonal Decomposition in the analysis of turbulent flows, *Annual Review Fluid Mechanics*, 25, 539, 1993.

[33] H.I. Tarman, A Karhunen-Loeve based approach to numerical simulation of transition in Rayleigh-Benard convection, *Numerical Heat Transfer Part B*, 43 (6): 567-586, 2003.

## APPENDIX A

### TEST FUNCTIONS

The functions chosen in section 3.4 produce the forcing terms which are to be added to the right hand side of the three components of momentum equation, hydro-magnetic equation and to the heat equation for them to be the solution fields:

$$\begin{aligned}
 \varphi_1(x, y, z, t) = & -2 \cos t \cos x \cos y z (1-z^2) \\
 & + \sin t \sin x \cos y (1-z^2)^2 (-2 \sin t \cos x \cos y (1-z^2) \\
 & + 4 \sin t \cos x \cos y z^2 - \sin t \cos x \cos y (1-z^2)^2) \\
 & - \text{Pr} (4 \sin t \cos x \cos y z (1-z^2) + 12 \sin t \cos x \cos y z) \\
 & + 6 Q^* \text{Pr} \sin t \cos x \cos y \left[ \frac{(e^{\sqrt{2}z} - e^{-\sqrt{2}z})}{(e^{\sqrt{2}} - e^{-\sqrt{2}})} - z \right] \\
 & + 2(Q^* / \sqrt{3}) \text{Pr} \sin t (\sin x \cos y + \cos x \sin y) \\
 & \cdot \left[ \frac{(-3/\sqrt{2})(e^{\sqrt{2}z} + e^{-\sqrt{2}z})}{(e^{\sqrt{2}} - e^{-\sqrt{2}})} + 1 + (3/2)z^2 \right]
 \end{aligned} \tag{A.1}$$

$$\begin{aligned}
 \varphi_2(x, y, z, t) = & 2 \cos t \sin x \sin y z (1-z^2) \\
 & + \sin t \sin x \cos y (1-z^2)^2 (-2 \sin t \sin x \sin y (1-z^2) \\
 & + 4 \sin t \sin x \sin y z^2 - \sin t \sin x \sin y (1-z^2)^2)
 \end{aligned}$$

$$\begin{aligned}
& -\Pr \left( -4 \sin t \sin x \sin y z (1-z^2) - 12 \sin t \sin x \sin y z \right) \\
& + 6 Q^* \Pr \sin t \sin x \sin y \left[ \left( e^{\sqrt{2}z} - e^{-\sqrt{2}z} \right) / \left( e^{\sqrt{2}} - e^{-\sqrt{2}} \right) - z \right] \\
& + 2 \left( Q^* / \sqrt{3} \right) \Pr \sin t \left( \sin x \cos y + \cos x \sin y \right) \\
& \cdot \left[ \left( -3 / \sqrt{2} \right) \left( e^{\sqrt{2}z} + e^{-\sqrt{2}z} \right) / \left( e^{\sqrt{2}} - e^{-\sqrt{2}} \right) + 1 + (3/2)z^2 \right]
\end{aligned} \tag{A.2}$$

$$\begin{aligned}
\varphi_3(x, y, z, t) = & \cos t \sin x \cos y (1-z^2)^2 \\
& + 2 \sin t \cos x \cos y z (1-z^2) \left( -2 \sin t \cos x \cos y (1-z^2) \right) \\
& + 4 \sin t \cos x \cos y z^2 - \sin t \cos x \cos y (1-z^2)^2 \\
& + 2 \sin t \sin x \sin y z (1-z^2) \left( -2 \sin t \sin x \sin y (1-z^2) \right) \\
& + 4 \sin t \sin x \sin y z^2 - \sin t \sin x \sin y (1-z^2)^2 \\
& - \Pr \left( -2 \sin t \sin x \cos y (1-z^2)^2 - 4 \sin t \sin x \cos y (1-z^2) \right. \\
& \left. + 8 \sin t \sin x \cos y z^2 \right) + \Pr Ra^* \sin t \sin x \cos y (1-z^2) \\
& + Q^* \Pr \sin t \sin x \cos y \left[ 6\sqrt{2} \left( e^{\sqrt{2}z} + e^{-\sqrt{2}z} \right) / \left( e^{\sqrt{2}} - e^{-\sqrt{2}} \right) - 6z^2 \right. \\
& \left. - 4 \right] + \left( Q^* / \sqrt{3} \right) \Pr \sin t \left( \cos x \cos y - \sin x \sin y \right) \\
& \cdot \left[ 6 \left( e^{\sqrt{2}z} - e^{-\sqrt{2}z} \right) / \left( e^{\sqrt{2}} - e^{-\sqrt{2}} \right) - 2z^3 - 4z \right]
\end{aligned} \tag{A.3}$$

$$\begin{aligned}
\varphi_4(x, y, z, t) = & \text{Cos } t \text{ Sin } x \text{ Cos } y (1-z^2) \\
& - 2 (\text{Sin } t)^2 [(\text{Cos } x \text{ Cos } y)^2 + (\text{Sin } x)^2] z (1-z^2)^2 \\
& - (1/2) \text{Sin } t \text{ Sin } x \text{ Cos } y (1-z^2)^2 + 2 \text{Sin } t \text{ Sin } x \text{ Cos } y (1-z^2) \\
& + 2 \text{Sin } t \text{ Sin } x \text{ Cos } y (1-z^2) + 2 \text{Sin } t \text{ Sin } x \text{ Cos } y
\end{aligned} \tag{A.4}$$

$$\varphi_5(x, y, z, t) = 2 \text{Sin } t (\text{Sin } x \text{ Cos } y + \text{Cos } x \text{ Sin } y) z (1-z^2) \tag{A.5}$$

$$\varphi_6(x, y, z, t) = 2 \text{Sin } t (\text{Sin } x \text{ Cos } y + \text{Cos } x \text{ Sin } y) z (1-z^2) \tag{A.6}$$

$$\varphi_7(x, y, z, t) = -\text{Sin } t (\text{Sin } x \text{ Sin } y - \text{Cos } x \text{ Cos } y) (1-z^2)^2 \tag{A.7}$$

## **CURRICULUM VITAE**

### **PERSONAL INFORMATION**

Surname, Name : Güray, Ersan

Nationality: Turkish (TC)

Date and Place of Birth: 14 July 1978, Kocaeli

Marital Status: Single

Phone: +90 535 279 26 92

Fax: +90 312 210 44 62

email: ersan\_guray@yahoo.com

### **EDUCATION**

<b>Degree</b>	<b>Institution</b>	<b>Year of Graduation</b>
MS	METU Engineering Sciences	2002
BS	METU Civil Engineering	2000
High School	Ankara College, Ankara	1995

### **WORK EXPERIENCE**

<b>Year</b>	<b>Place</b>	<b>Enrollment</b>
2005-2006	TUBITAK	Research Assistant
2002-2003	AKEN Yapı Denetim	Assistant Controller

### **FOREIGN LANGUAGES**

Advanced English, Basic French

### **HOBBIES**

Reading, movies, trekking, outdoor activities.